Ph.D. DISSERTATION

Design of Wireless Power and Data Transfer System with Perfluoroalkoxyalkane (PFA) Film Based Electrodes Fabrication for Retinal Prosthesis

인공 망막 장치를 위한 Perfluoroalkoxyalkane 기반의 전극 공정법 개발 및 무선 전력과 정보 송수신 시스템 설계

BY

JISUNG KIM

February 2023

Department of Electrical and Computer Engineering
College of Engineering
Seoul National University

Design of Wireless Power and Data Transfer System with Perfluoroalkoxyalkane (PFA) Film Based Electrodes Fabrication for Retinal Prosthesis

인공 망막 장치를 위한 Perfluoroalkoxyalkane 기반의 전극 공정법 개발 및 무선 전력과 정보 송수신 시스템 설계

지도교수 서종모

이 논문을 공학박사 학위논문으로 제출함

2023년 2월

서울대학교 대학원

전기정보공학부

김 지 성

김지성의 공학박사 학위 논문을 인준함

Chair	김재하	(Seal)
Vice Chair	서종모	(Seal)
Examiner	송윤규	(Seal)
Examiner	Andrea Neviani	(Seal)
Examiner	정준수	(Seal)

Abstract

Keyword : Neural prosthesis, Retinal prosthesis, Perfluoro alkoxyalkane(PFA), Micro electrode array, DC-DC step-up converter, Pulse delay modulation (PDM)
Student Number : 2017-22199

The neural prosthesis device is an implantable medical device that helps patients with neurological dysfunction recover their function through direct electrical stimulation. Recently, artificial retina technology has emerged as a method of restoring sight to blind people who have lost retinal functions by electrically stimulating intact bipolar cells or retinal ganglion cells in the visual system. A problem mainly occurring in implantable biomedical devices such as artificial retinas is limited space that can be inserted into the living body. Existing implantable batteries have limitations in that they are bulky and need to be replaced periodically. Therefore, implantable medical devices require a wireless power transmission system to provide a stable supply voltage in a relatively small size. In addition to power and information transmission and reception technologies used in existing implantable medical devices, there are also limitations to biocompatible materials. Materials used in implantable neural prosthetic devices are generally biocompatible metals, glass, or ceramics. Feedthrough technology is required for metal-based encapsulation, such as titanium, due to system isolation. In addition, the assembly process is complicated, and the completed module is bulky, so there is a limit to the implantation site in the body, or internal tissue may be damaged. Microelectromechanical systems (MEMS) compatible polymer-based devices are currently not durable enough for organ implantation.

Therefore, in this study, an inductive wireless power transmission system designed to meet the requirements of an artificial retina and a planar electrode based on biocompatible fluororesin PFA were presented. A reconfigurable DC-DC step-up converter capable of boosting at various magnifications was designed

considering the low coupling coefficient of wireless power transmission in an implantable device in vivo, and a target power of 30mW was achieved with an output voltage of 5V. For wireless information transmission, a pulse delay modulation technique was used to achieve an information transmission rate of 13.56 Mbps, the same as the power transmission frequency of 13.56 MHz. In addition, a thin and flexible integrated process technology with a total thickness of 62.7um was established by designing a 20-channel electrode with low water absorption and capable of thermal bonding. A charge storage capacity of 0.65mC/cm2 or more, the critical charge density limit of general artificial retinas, was achieved.

The performance, stability, and biocompatibility were verified through in vitro and ex vivo experiments for the long-term durability of the developed artificial vision device. Judging from the accelerated life test, the stimulation electrode's polymer-metal bonding has been enduring over 180 days at 75 ° C and is currently in progress. This period is expected to operate normally for about 8 years or more at in vivo temperature. Furthermore, the biocompatibility was verified through cytotoxicity, extract tests according to ISO standards, and Korean Pharmacopoeia and biocompatibility were determined. In addition, the effectiveness of electrode stimulation was verified through ex vivo experiments.

Table of Contents

List of Tables

List of Figures

Notes

Some parts of this dissertation are extracted and adapted from the journal or conference publications that were published or submitted during this study.

1) Kim, Jisung, et al. "A 13.56 MHz reconfigurable step-up switched capacitor converter for wireless power transfer system in implantable medical devices." Analog Integrated Circuits and Signal Processing 110.3 (2022): 517-525
2) Kim, Ji-Sung, et al. "Micro Electrode Arrays Fabrication Using Flexible Perfluoroalkoxy Alkane Films." 2019 41st Annual International Conference of the IEEE Engineering in Medicine and Biology Society (EMBC). IEEE, 2019

Chapter 1. Introduction

1.1. Background

1.1.1 Neural Prosthesis

The neural prosthetic device is an implantable medical device that helps patients with nerve dysfunction restore their function through direct electrical stimulation. Neuro-prosthetic devices using nerve stimulation function have been continuously studied for decades. They are now helping patients in various fields, such as deep brain stimulation (DBS) for Parkinson's disease [1], retinal prosthesis [2]-[4], cochlear implant [5]-[7], and cardiac pacemaker [8]. DBS is considered an alternative surgical treatment for patients with refractory tremors or those affected by long-term complications of levodopa therapy, such as movement fluctuations and severe dyskinesia [9]. The depth type probe stimulates the thalamus area with electrical stimulation. Similarly, cochlear implant is one of the most commercialized implantable neural prosthesis devices. Cochlear implants have provided a partial hearing to more than 120,000 people worldwide, half of whom are pediatric users who are able to develop near-normal speech. A cochlear implant is an operation to implant a cochlear implant in a patient with severe sensorineural hearing loss in both ears due to a disease of the cochlea, and the hearing does not help even when wearing a hearing aid. In this process, the outer part of the

cochlea detects high frequencies, and the inner part detects low frequencies. The 'vibration of air' called sound is converted into various 'electrical signals' that the auditory nerve can interpret and transmit to the brain. Hearing loss is a situation in which a particular part of the process suffers. A hearing aid is usually worn in the case of 'conductive hearing loss,' which is a problem in the outer and middle ear that amplifies the vibration. The problem is sensorineural hearing loss, which is a problem with the inner ear, especially the cochlea. If the cochlea is malformed or severe hearing loss due to more than hair cells, it is difficult to recognize it as a proper sound no matter how loud the sound is. A cochlear implant is a device that replaces the process of converting sound into electrical signals. It consists of a 'sound processor' that is hung or attached behind the ear, an 'implant' implanted in the skull, and an electrode inserted into the cochlea. A sound processor captures the external sound and converts it into a digital signal, which passes through the skin and is transmitted to the implant in the body. The implant converts the signal into electrical stimulation and transmits it directly into the cochlea through electrodes, and the auditory nerve sends it to the brain [10].

1.1.1.1 Power Supplies for Implantable Devices

Numerous power sources for IMDs have been extensively

investigated over the past few decades, as most IMDs must rely on a permanent and sufficient power supply to ensure proper operation. Different power approaches can allow the autonomous operation of IMDs by generating power to replace or supplement existing battery power. The main traditional challenges have been size limitations, inaccessibility, the need for continuous work, and biocompatibility [11].

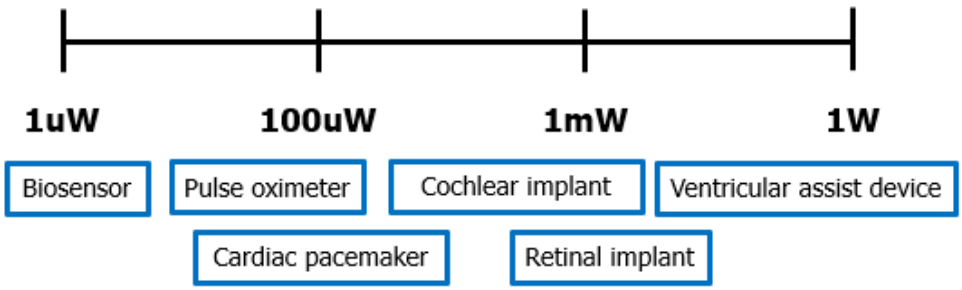

Figure 1 Power requirements for implantable medical devices

The power required to drive a biomedical device ranges from a few uW to hundreds of mW. Among them, in the case of the cochlear implant described above, since the number of electrodes driven is smaller than that of the artificial retina, it is driven with the power of several hundred uW. In contrast, in the case of the artificial retina, correspondingly high power is required to implement a resolution similar to that of vision [12].

1.1.1.1.1 Implantable Battery

Figure 2 Power supplies for implantable devices

Batteries typically store energy in the form of chemicals that can produce electricity. A battery contains an anode, a cathode, and an electrolyte, allowing ions to move and form an electric current. As a reliable source for long-term applications such as cochlear implants, pacemakers, defibrillators, or drug delivery, these Li batteries are widely used to provide the appropriate power levels from microamps to amps required by many types of IMDs. However, further implementations on implants have been limited by remaining hurdles of size and questions related to potential toxicity [13]- [15].

1.1.1.1.2 Wireless Power Transfer

A significant problem with implantable biomedical devices such as artificial retinas is that the space that can be inserted inside the body is limited. In addition, existing implantable batteries are bulky and have limitations because they need to be replaced periodically. Therefore, implantable medical devices require a wireless power transfer system to provide a stable supply voltage in a relatively small size.

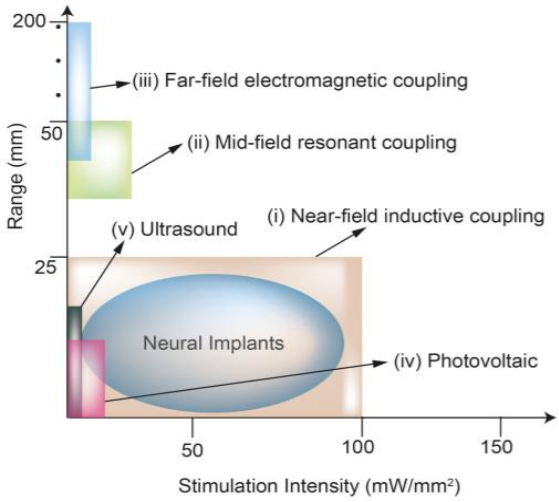

Figure 3 Wireless Power Transfer (WPT) in [16]

Most implantable nerve stimulators are powered by inductive link wireless power transfer. Near the magnetic field, coupling helps minimize tissue heat transfer due to low energy absorption and low loss by biological tissue.

Various wireless communication technologies have been applied in implantable artificial prosthesis devices. Among these technologies,

near-field magnetic communication systems are promising because they provide the advantages of near-field magnetic technologies.

Near-field magnetic systems have distinct advantages in lossy dielectric media such as water, or biological tissues. In such environments, the conventional far-field Electro-Magnetic (EM) technologies experience significant path loss as a result of high energy absorption in the medium. The near-field magnetic systems are more efficient than the conventional far-field counterparts for power and information transmission since they experience much less energy absorption in a lossy dielectric medium [17].

Because of their lower path loss, the near-field magnetic systems can transfer power and information using less transmission power compared to conventional far-field EM technologies, while satisfying specific absorption ratio (SAR) constraints. Since near-field magnetic systems ensure better safety, they are more suitable for implantable biomedical devices [18].

Furthermore, the near-field magnetic systems are highly reliable in lossy dielectric medium. Conventional far-field EM technologies exhibit variable channel conditions and propagation delays due to the inhomogeneous permittivity of the materials in transmission environments such as soil and the human body. In contrast, near-field magnetic systems experience negligible channel variations even in an inhomogeneous lossy medium, because these materials have similar permeability [19].

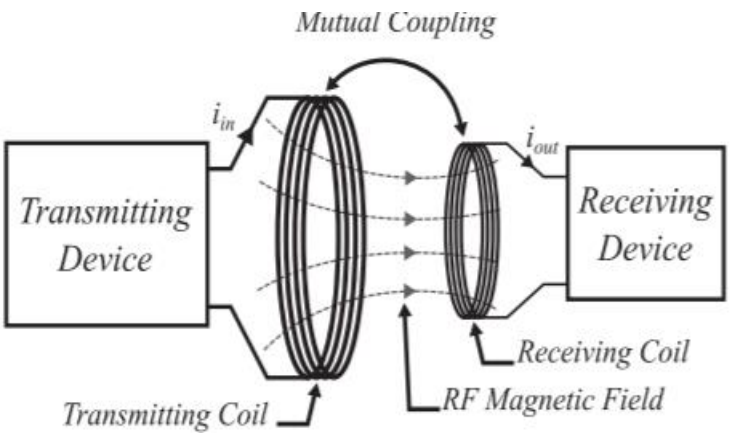

Figure 4 Near field magnetic system for wireless transfer system [20]

1.1.2 Artificial Retina System

Recently, with the rapid development of electronics, the development of an artificial visual transmission device for restoring eyesight using bionics technology combining biology and electronics are being attempted. The core of this device is to mimic the function of

the retina, which converts external light into bioelectric signals that can be interpreted by the human nervous system and transmitted them.

1.1.2.1 Retina Layers

The retina is a transparent nervous tissue that covers about 2/3 of the inside of the eyeball and is located at the back of the eyeball. The wall of the eyeball is composed of a fibrous membrane, a blood vessel membrane, and a nerve membrane, and the thin nerve membrane surrounding the innermost layer is called the retina. The retina is formed in two layers at the back of the eyeball, the outer retina in the front is called the pigment layer retina, and the inner retina is called the neural layer retina. The retina is composed of nerve cells and glial cells, and the color-sensing cells, the cones, are gathered and slightly recessed in this area called the fovea and the most resolving and sensitive area. The yellow area around the fovea is called the macula and is the center of the field of vision. Anatomically, the retina is classified as a terminal sensory group, but embryologically it can be viewed as a part of the central nervous system.

When light enters the eye through the cornea and lens, an image is formed on the retina, transforming the shape into electrical signals to transmit information from the optic nerve to the brain. In particular, the photoreceptor cell containing a protein molecule called opsin absorbs a photon and transmits a signal to the photoreceptor cell. The central part of the vision is called the macula, and in the retina, other

than the macula, it plays a role in seeing dark areas and peripheral areas. And the external image coming through the lens is reversed up, down, left, and right to form an image on the retina, and since the two eyes look at the object from different angles, the retinal image of each eye is inconsistent, allowing us to perceive the distance of the object. In addition, the rod cells in the retina react sensitively to a small amount of light, allowing objects to be identified even in dark places. Send the relevant information.

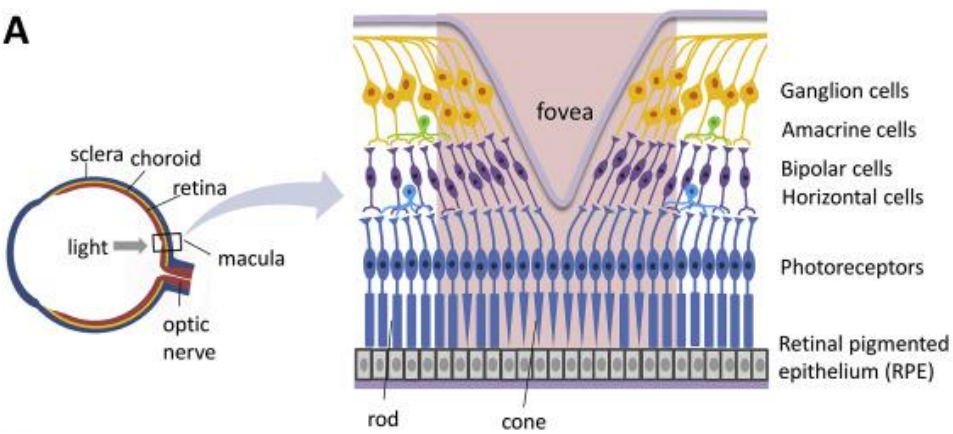

Figure 5 Retinal tissue layers [21]

1.1.2.2Artificial Diseases

Retinitis pigmentosa (RP) is a hereditary disease in which the retina's function is lost due to the accumulation of pigment in the retina, which converts light entering the eye into electrical signals. In patients with retinitis pigmentosa, the visual field gradually narrows as the eye cells are damaged, and eventually, they lose sight. The cause of

retinitis pigmentosa is a defect in the gene involved in converting light into electrical signals within the visual cells. In some people without a family history, the disease develops suddenly. An early symptom of retinitis pigmentosa is night blindness, which makes it difficult to see things in the dark or at night. If the patients suddenly enter a dark place, they may not adjust well, have problems when going out at sunset, or live in a dark room becomes difficult. As the disease progresses, they may see only the middle like a tunnel (tunnel field of view), their vision may be blurred, and their may be unable to read or recognize faces. Although the symptoms and timing of the onset of retinitis pigmentosa vary from patient to patient, many patients lose sight. However, the course varies from person to person to the extent that some people maintain their sight until their 50s and 60s [22].

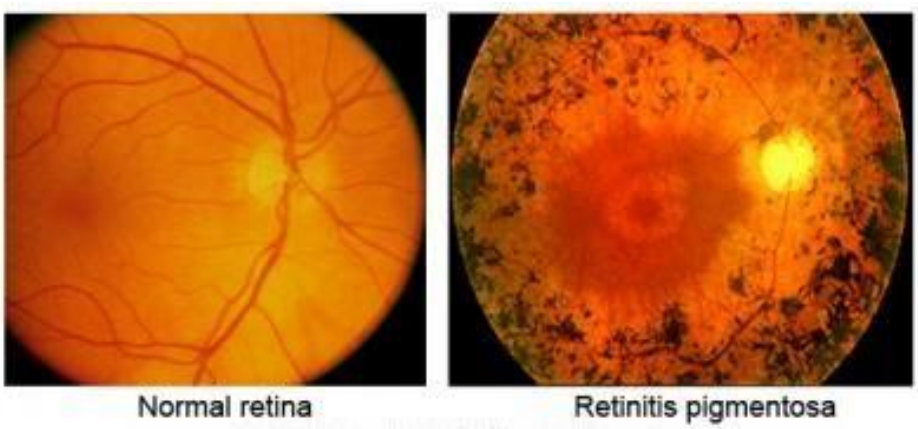

Figure 6 One of the most popular artificial disease: retinitis pigmentosa

Age-related macular degeneration (AMD) is a degenerative disease that occurs in the macula of the eye tissue and causes vision loss. The macula refers to the center of the retina. This macula is what allows to see objects accurately. As we age, many changes occur in the macula, and macular degeneration is one of the representative changes. Just because you have macular degeneration doesn't mean you're living in darkness with patients' entire vision darkened. However, the part you want to see looks dark or distorted.

In the early stages of macular degeneration, letters or straight lines appear shaky or curved. Eventually, the vision deteriorates a lot, and an invisible area is formed in the center of the field of vision [23].

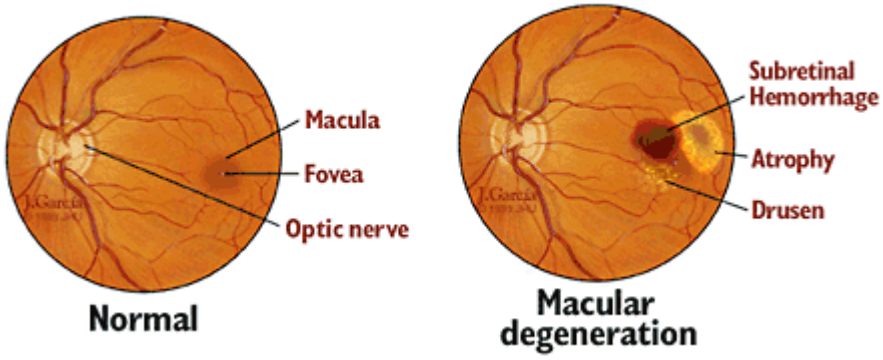

Figure 7 Age-related macular degeneration

1.1.2.3Electrical Treatment

There is no cure for AMD or RP, and most current treatments aim to slow cell death and the resulting loss of vision. In addition, nutritional supplements have been used to prevent the progression of AMD and RP [24].

During the advanced stages of photoreceptor degeneration, the neural retina is also significantly altered. Lack of regular input from unresponsive or absent photoreceptors leads to significant neuronal remodeling [25].

Despite reorganization and cell loss, the inner retinal neurons retain their signal transduction ability. Morphometric analysis showed that more than 50% of ganglion cells, based on nuclei count, survive in wet AMD, and the ganglion cell density in dry AMD is not significantly different from that of a normal eye, even in areas of the retina where photoreceptors are virtually absent [26].

Morphological studies of patients with severe human RP indicate moderate conservation of inner retinal neurons (70–80% of bipolar cells and 25–40% of ganglion cells). Inner retinal preservation supports the potential for vision restoration by establishing a stimulation mechanism that bypasses the damaged photoreceptor layer and interfaces directly with the remaining inner retinal neurons. Work in this field is primarily based on several stimulation modalities, including bioelectronics, optogenetics, photochemistry, and, more recently, ultrasound stimulation. These distinct approaches are detailed in this article in terms of underlying mechanisms and prosthetic

systems [27].

Neurons in our body are interconnected with other nerve cells in a structure called 'neural synapse (or neural synapse).' In most cases, the electrical signal generated by a specific nerve cell is not transmitted to other nerve cells as it is. Instead, in a nerve synapse, an electrical signal is transformed into the secretion of a chemical substance, a neurotransmitter, and information is transmitted by binding to the 'neurotransmitter receptor' of the other neuron.

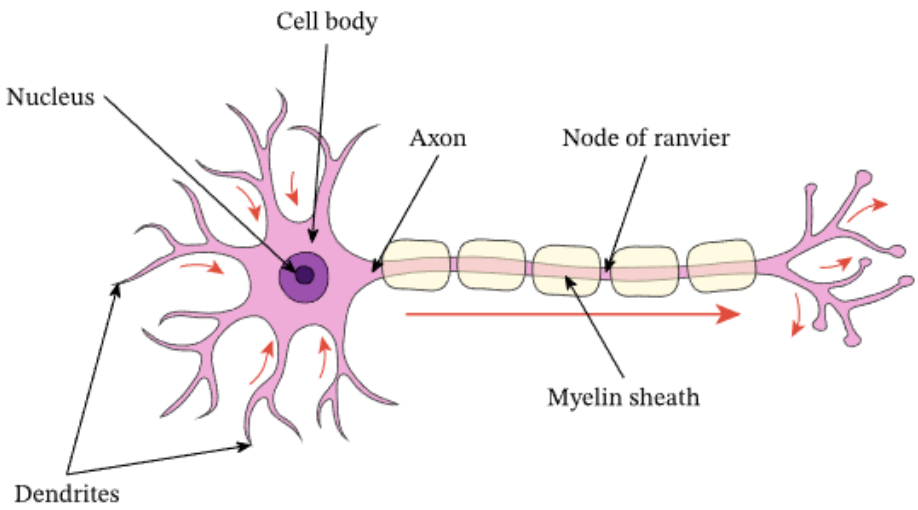

Figure 8 Structure of a neuron

As a major cell in the nervous system, sensory neurons transmit nerve impulses to the spinal cord and brain, and motor neurons transmit commands from the brain or spinal cord to muscles or glandular tissues. A neuron consists of one axon and one or two dendrites, and it functions to receive and store various information by sending and receiving

signals through a structure called a synapse that connects neurons to neurons. Neurons can be classified into neuronal cell bodies, dendrites, and axons. The neuron cell body is the central part of the nerve cell and contains the nucleus and cytoplasm of the cell. A dendrite is a part where nerve cells receive signals and is characterized by branching. An axon is a part that extends from the neuronal cell body and transmits the signal transmitted to the dendrites and the nerve cell body to other nerve cells or cells. In a neuron, a synapse is created when two nerve cells are connected, and two cells send and receive signals through a synapse [28].

The nervous system of our body receives and transmits external stimuli and processes the information to induce a response. Nerve bundles spread throughout the body and quickly and accurately transfer information using electrical signals called 'action potentials,' Numerous nerve cells in the brain integrate and process information using these electrical signals. The action voltage generated by nerve cells is about 0.1 V, which occurs for about 1/1000 of a second.

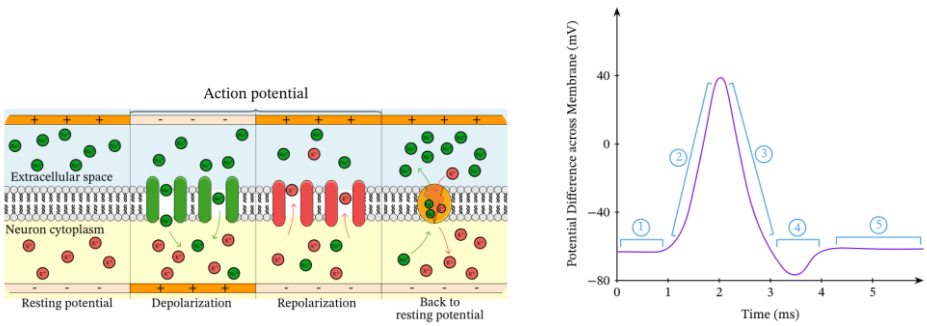

Figure 9 The maintenance of resting potential of neuron and

action potential [29]

On all neurons' surfaces (cell membrane), there are more negative ions than positive ions on the inside and more positive ions than negative ions on the outside, so a potential difference (voltage) occurs between the membranes. The pure charge is expressed to the outside by the complex interaction of the cation and anion. For this reason, the inside of the cell is usually more negative than the outside, and this voltage difference is called the stable membrane voltage of the neuron. The stabilizing membrane voltage at the stimulation site changes dramatically when a neuron is stimulated. This voltage change, called an action potential, is propagated along the axon, and the propagation of this action potential is the main method of transmitting a signal in the human body. [30].

Electrode-based extracellular stimulation works by injecting an electric current into the tissue of interest through a single or array of electrodes placed nearby. For example, in bioelectronic retinal implants, electrodes are placed close to the retina to form an electrochemical interface with physiological saline. The current injected by the stimulation electrode is passed through the retinal tissue to a return electrode placed either locally on the array or at a distant location. An electric current delivered to the extracellular region causes a redistribution of charge across the cell membrane of retinal neurons. An action potential is firing when the membrane depolarization exceeds

a threshold [31].

1.1.2.4 Photodiode System

Photodiode artificial system is a method that acquires an image with a camera, converts it into the light of a near-infrared wavelength (880-905 nm) with minimal influence on the retina, and irradiates it to a photovoltaic chip containing a photodiode implanted under the retina. This device stimulates the retinal bipolar cells by irradiating near-infrared rays of strong intensity into the eye to induce a current sufficient to stimulate the retina only with light intensity without dependence on an external power source. Furthermore, since this chip does not require a cable for an external power supply, it has the advantage that a stimulation chip can be placed in the eyeball [32].

1.1.2.5 Optogenetics

Optogenetics is a method of controlling gene expression and firing neurons using light rays. It is widely used to detect neural circuits in the laboratory and is being studied as a potential treatment for pain, blindness, and brain disorders.

Optogenetic therapy uses viruses to deliver algae photoreceptor protein genes to RGCs, bypassing damaged photoreceptor cells and allowing direct image detection [33].

1.1.2.6 Gene Therapy

Gene therapy is a treatment that replaces a gene with a specific mutation into a normal gene using an adeno-associated virus vector (AAV) for retinal degenerative diseases caused by a single recessive gene abnormality. Since it is difficult to restore already damaged cells to their original state, it is considered as a treatment method at an early stage when the damage is relatively mild. There is a limitation in that the success or failure of retinal gene therapy depends on the accurate diagnosis of patients with suspected hereditary retinal disease [34].

1.1.3 Conventional Retinal Devices

Conventional artificial retinal devices using electrical stimulation include the epiretinal stimulation method located on the side of the retinal ganglion cells in the eye according to the intraocular position of the electrode that stimulates the retina and the electrode located at the position of the photoreceptor cells between the neural retina and the retinal pigment epithelial cell layer: subretinal stimulation. And finally, placing the electrode on the episcleral, suprachoroidal stimulation has been commercialized and inserted into patients. In addition to directly stimulating the retinal layer, there is a method of directly stimulating the optic nerve by winding a cuff electrode around the optic nerve behind the eyeball and a method of stimulating the visual cortex. However, these methods are complicated because they require neurosurgical surgery and transmit visual information processing that is still not well known.

The target of epiretinal stimulation is retinal ganglion cells, and it is relatively easy to insert electrodes into the eye, but since the retina is very thin and fragile, it is difficult to fix the electrodes. In addition, when electrical stimulation is applied from the upper surface of the retina, the retinal nerve fiber layer is stimulated to spread the signal, or cells in several layers of the retina are stimulated at once, making it difficult to increase spatial resolution. Since the intraretinal signal processing process cannot be utilized, the shape of the stimulating electrode grid may differ from the shape felt by the patient, so customized image processing is required for each patient. Therefore, rather than a subretinal type stimulator, various parts, and a signal transmission unit connecting them are required [35], [36].

The subretinal method aims to replace the function of photoreceptors because patients with damaged photoreceptors located at the bottom of the retina need artificial retinas. This method can also utilize the neural processing in the retina that occurs between bipolar cells, horizontal cells, and retinal ganglion cells so that the image processing unit can be omitted [37] – [39].

With suprachoroidal approach, though the furthest distance to the target neuron can lead to the highest threshold and lowest resolution of the three approaches, the surgical procedure is the most invasive and simplest [40], [41].

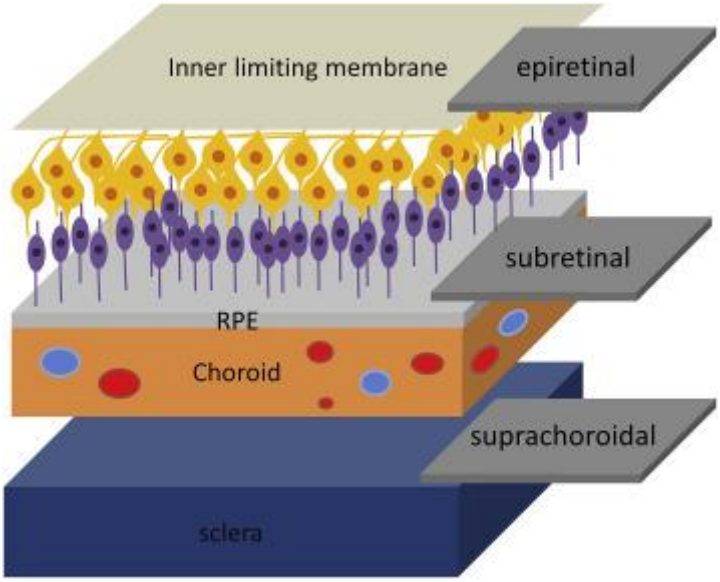

Figure 10 Conventional retinal prosthesis method according to implant placement [42]

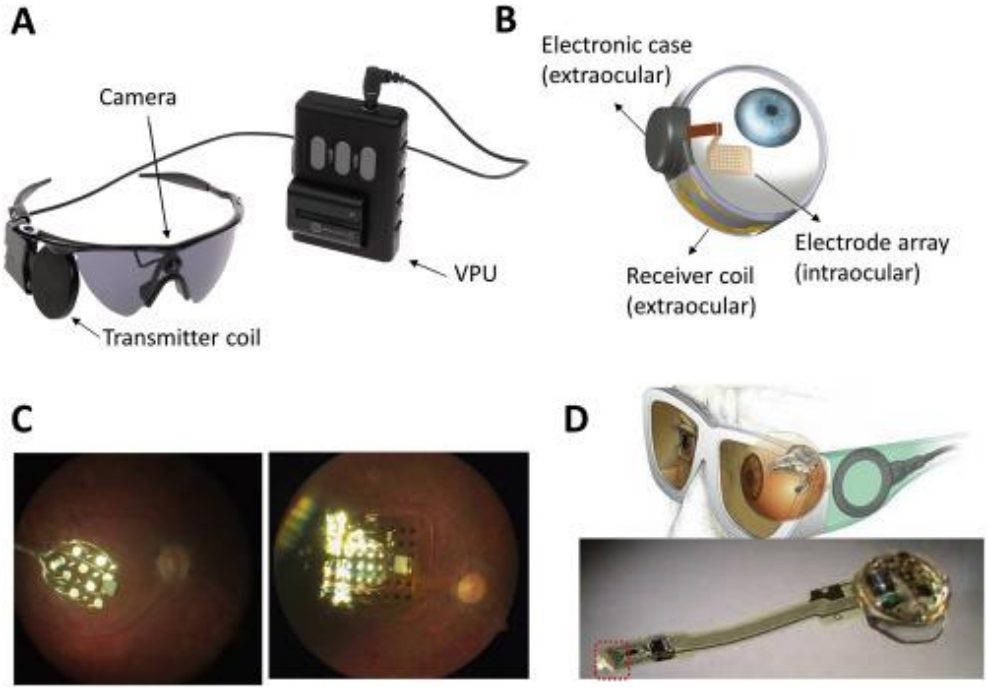

Figure 11 Commercialized implantable retinal prosthesis devices:

Epiretinal artificial retina from Argus II Second sight [43]

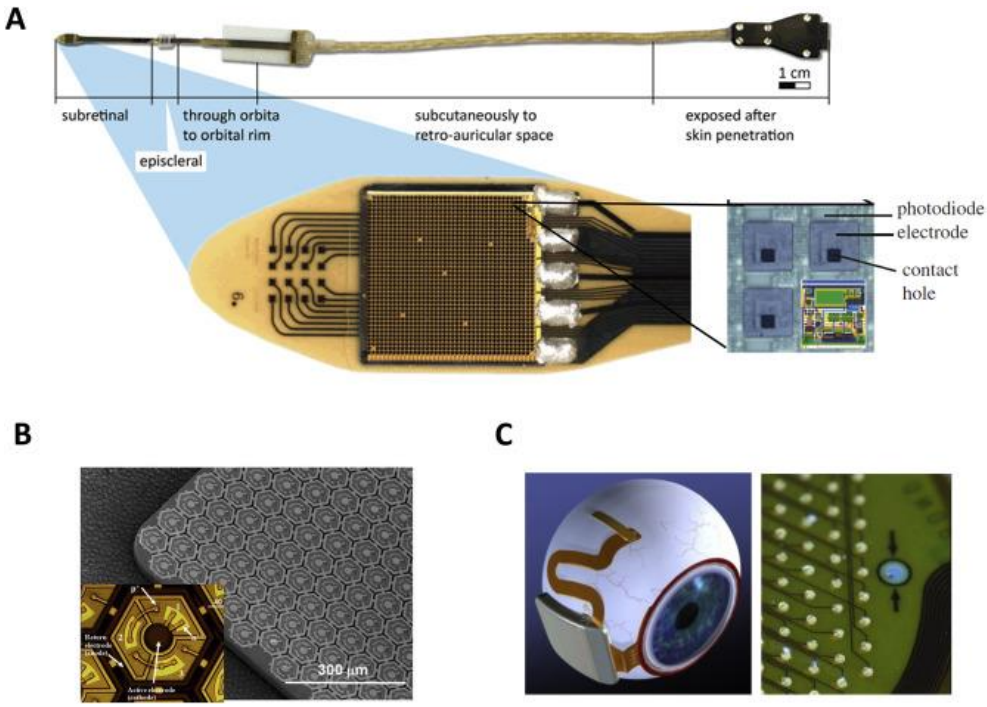

Figure 12 Commercialized implantable retinal prosthesis devices [47]: Subretinal artificial retina from Alpha IMS [44], from Stanford university [45], from Harvard university [46]

1.1.4 Perfluoroalkoxyalkane (PFA)

The neural prosthetic devices are composed of several parts with different roles. Among them, the electrode interfaces which connect the electrical system with the living body require the strongest biocompatibility. In addition, since this part exposed to the chronic damage caused by the continuous electrical stimulations, various

chemical and physical properties, including hygroscopicity and durability, are also important. In general, biomaterials used in neural prosthetic devices are made of metals, glasses, ceramics, or polymers. Recently, polymers are widely used because of their high flexibility, high chemical resistance, and low production compared to other materials. Polymer-based electrodes are suitable for mass production because they are easily moldable, flexible, and inexpensive. In addition, the application of Micro Electro Mechanical System(MEMS) fabrication process on the polymer is easy due to its excellent chemical resistance [48].

There are several considerations when selecting a biocompatible polymer for the substrate material of a bio-implantable electrode. First, the biocompatible polymer should have a low water absorption rate and maintain its function in the living body after implantation. Also, it is desirable to have a modulus of elasticity similar to that of the tissue to prevent tissue damage in the portion directly in contact with the body after transplantation. In addition, when the system operates based on a wireless signal, it is advantageous to have a low dielectric constant so that the wireless signal can be transmitted

or received. Finally, it must be resistant to high temperatures to enable the application of MEMS fabrication process [49].

The material properties of biocompatible polymers were compared in Table 1. Biocompatible polymers frequently used in implantable medical devices are mainly polydimethysiloxane (PDMS), Parylene-C, and polyimide. Since PDMS has a relatively low Young's modulus compared to other biocompatible polymers, it is being used for various applications. However, the high hygroscopicity causes the PDMS substrate to degrade in a similar environment to the human body. To compensate for this, PDMS is often used with parylene-c, which has a higher Young's modulus than PDMS but has significantly lower moisture absorption. However, since parylene-C has a high Young's modulus, it can damage living tissue except when used very thinly. Polyimide is a biocompatible polymer frequently used in various fields thanks to its unique spin-coating properties. However, the electrode manufactured with polyimide multi-layers using spin coating has a limitation in that it can be easily delaminated in body fluid [50] - [53].

Table 1 Characteristics of biocompatible polymers

	LCP	PDMS	Polyimide	Parylene-C	COC	PFA	FEP	PTFE	ETFE
Water absorption (%)	0.04	0.4	0.3	0.06	0.01	0.02	0.01	0.01	0.03
Melting temperature ($^{\circ}C$)	315	-40	520	290	163	305	260	327	150
Young's modulus (Pa)	20G	2M	2.5G	2.7G	2.1G	0.5G	0.43G	0.5G	1.5G
Dielectric const. @1MHz	2.8	2.5	2.4	2.95	2.3	2.05	2.0	2.0	2.6

LCP: Liquid crystal polymer; PDMS: Polydimethylsiloxane; COC: Cyclic olefin copolymer; PFA: Perfluoroalkoxy alkane;
FEP: Fluorinated ethylene propylene; PTFE: Poly tetra fluoro ethylene; ETFE: Ethylene tetra fluoro ethylene;

Considering these conditions, it is beneficial to use a thermoformable polymer to manufacture an integrated electrode that maintains its shape for a long time, even inside a living body. Thermoplastic polymers with strong heat resistance have been applied to many medical devices over the past 20 years because they can withstand temperatures over 200℃ and bond very strongly when molded [54]. Among the thermoplastics, fluoropolymers have outstanding characteristics owing to its chemical structures. The fluoropolymers have aliphatic or aromatic characteristics because of the included fluorine, which has amorphous or semi-crystalline structures. The carbon-fluorine bond inside the fluoropolymer is a polar bond with very high bond strength, and the intermolecular attraction is weak. For this reason, the fluoropolymer has a low surface energy and a low coefficient of friction. Due to their low surface energy, fluoropolymer can be mixed or coated with other polymers to impart lubricity and water resistance to the surface. In addition, a fluoropolymer has a high heat resistance and excellent dielectric properties. With these superior properties, fluoropolymers are used in various applications, from flexible tubes to catheters and vascular

implants.

Among them, especially, Perfluoroalkoxy Alkane (PFA) has outstanding permeability, elongates over 300% with tensile strength of 27MPa, 0.5GPa of modulus of elasticity and physical properties with water absorption rate of 0.01%. It is also suitable for general MEMS process due to the high thermal melting point up to 305° C and has strong resistance to chemicals [55].

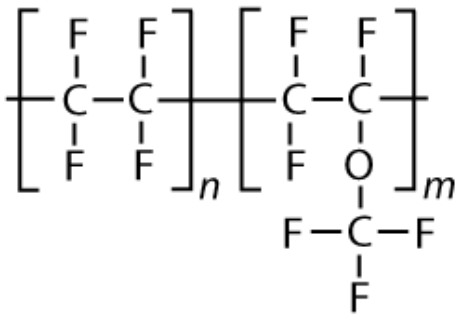

Perfluoroalkoxy Alkane : PFA

Figure 13 The molecular structure of perfluoroalkoxy alkane (PFA)

Table 2 Possible fluoropolymers as electrode substrate

	PFA	FEP	PTFE	ETFE
	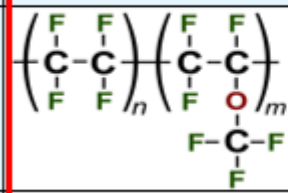	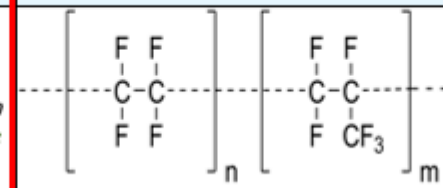	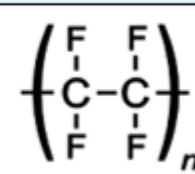	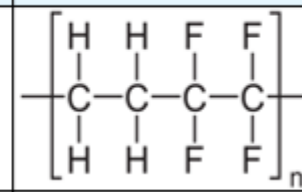
Water Absorption(%)	0.02	0.01	0.01	0.03
Melting temp.(℃)	305	260	327	150
Young's modulus(Pa)	0.5G	0.43G	0.5G	1.5G
Dielectric const.	2.05 @1MHz	2.0 @1MHz	2.0 @1MHz	2.6 @1MHz

Chapter 2. Methods

2.1 Wireless Power and Data System

2.1.1 General Specifications

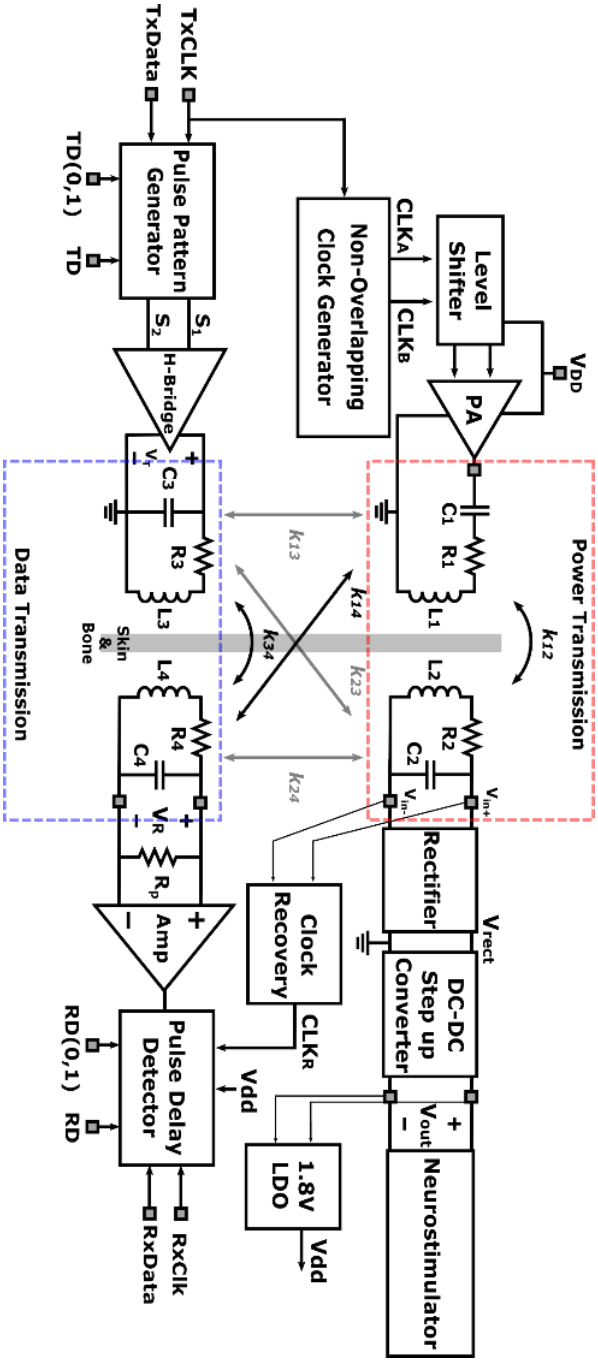

Figure 14 Full power and data transmission circuit system diagram

2.1.2 Near Field Transmission

Various wireless communication technologies have been applied in implantable artificial prosthesis devices. Among these technologies, near-field magnetic communication systems are promising because they provide the advantages of near-field magnetic technologies.

Near-field magnetic systems have distinct advantages in lossy dielectric media such as water, or biological tissues. In such environments, the conventional far-field Electromagnetic (EM) technologies experience significant path loss as a result of high energy absorption in the medium. The near-field magnetic systems are more efficient than the conventional far-field counterparts for power and information transmission since they experience much less energy absorption in a lossy dielectric medium.

Because of their lower path loss, the near-field magnetic systems can transfer power and information using less transmission power compared to conventional far-field EM technologies, while satisfying specific absorption ratio (SAR) constraints. Since near-field magnetic systems ensure better safety, they are more suitable for implantable biomedical devices.

Furthermore, the near-field magnetic systems are highly reliable in lossy dielectric medium. Conventional far-field EM technologies exhibit variable channel conditions and propagation delays due to the inhomogeneous permittivity of the materials in transmission environments such as soil and the human body. In contrast, near-field magnetic systems experience negligible channel variations even in an inhomogeneous lossy medium, because these materials have similar permeability [56].

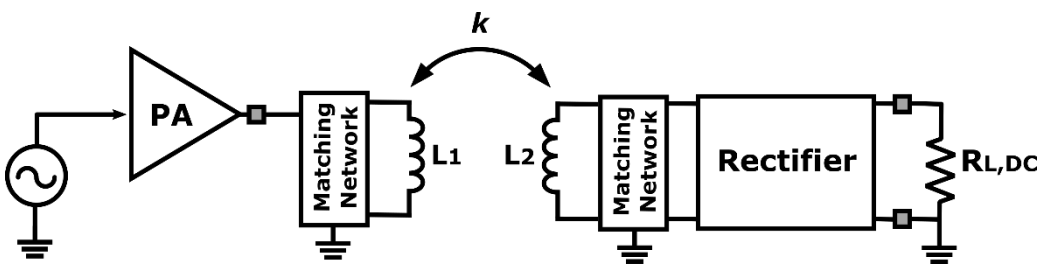

Figure 15 Near field wireless power transfer scheme [57]

A schematic diagram of a typical wireless power supply is shown in Figure 15. A power amplifier(PA) with an radio frequency (RF) voltage source input transmits power through the primary coil. Some form of matching is used to adjust the intrinsic loop inductance to reduce the loading effect on the power amplifier. As long as the

operating wavelength is much smaller than the coil's physical dimensions and separation, the energy is mainly contained in the near magnetic field. Thus, a secondary coil receives energy from the time-varying magnetic field generated by the transmitter. The RF output of the secondary-side matching network then passes through a rectifier to convert AC energy to DC energy used to power the load.

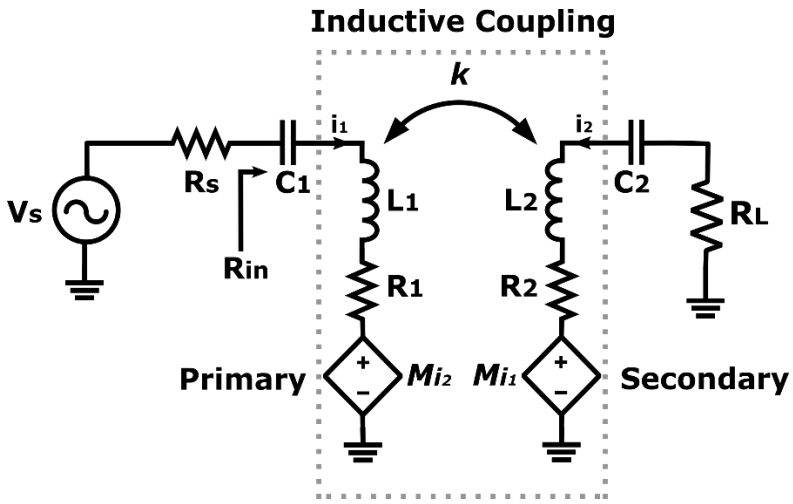

Figure 16 Near field wireless power transfer circuit load [58]

A more detailed schematic of a typical inductively coupled system is shown in Figure 16: Inductors L1 and L2 model the primary and secondary loop reactances, respectively. However, inductors are not perfect because they all have a finite quality factor. In particular, the

quality factor of each coil is specified as

$$Q = \frac{\omega L}{R} \ (Quality\ factor)$$

Here w is the operating frequency, and R is the parasitic series loss resistance. Voltage sources Mi2 and Mi1 model the effect of mutual coupling between the coils, where M is the mutual coupling coefficient, and capacitors C1 and C2 provide resonant matching with the inductor. The equation defines the coil coupling coefficient k:

$$k = \frac{M}{\sqrt{L_1 L_2}} \ (Coupling\ coefficient) \quad \eta = \sqrt{\frac{L_2}{L_1}}$$

, where M is mutual coupling factor. The near field system generally has a range of 0.03 <K <0.3.

Power transfer efficiency must be high for the external power source to become smaller in a normal wireless power transmission system. Therefore, the inductor must resonate with the capacitor to increase the efficiency of wireless power transmission.

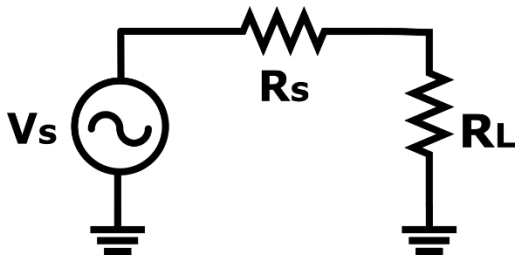

Figure 17 Simplified load for near field wireless transfer circuit

Near Field Wireless Transfer Circuit can be shown as shown in Figure 17. Here, for maximum power transfer to load resistance, you must meet the condition of RS = RL. Therefore, the impedance matching must be made the same as the source's impedance and the load of the road.

$$\eta = \frac{R_L}{R_S+R_L} \quad , \; P_L = \frac{V_S^2 R_L}{(R_S+R_L)^2}$$

For inductive coupled circuit, with reflected load analysis, the inductively coupled coil can be assumed as loosely-coupled transformer.

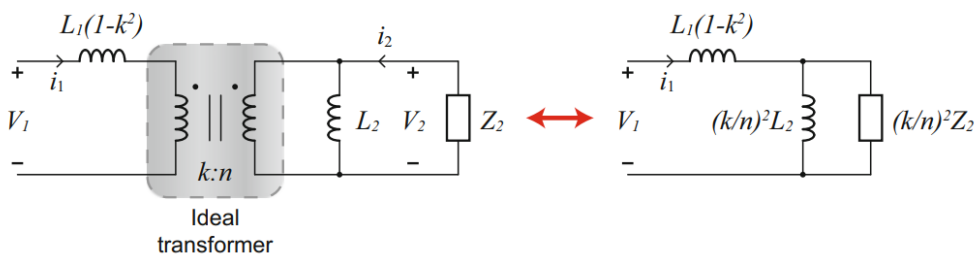

Figure 18 Reflected load diagram of coupled coil

Figure 18 shows the reflected load diagram of coupled coil. After reflected load analysis, it is better to do resonance tuning for

primary coil by connecting the capacitor in series or either parallel. Generally adding series capacitor reduces loading effect of voltage-based source, it is more efficient to add series capacitor to primary coil.

For secondary coil tuning, there are two different methods. First, parallel tuning, which is represented as a voltage multiplication factor. By adding parallel capacitor, the operation of rectifier could get faster. The series-parallel tuning method often used in low power application with large RL. The other method is to put series capacitor. This scheme is more likely to be used in high power application.

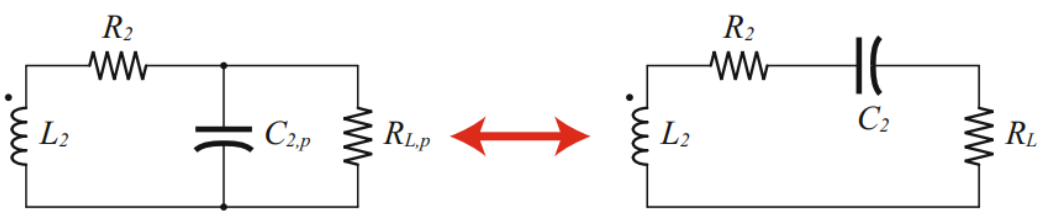

Figure 19 Secondary coil tuning

$$Q_L = \omega C_{2p} \cdot R_L$$

$$R_L = R_{Lp}(1 + {Q_L}^2)$$

$$C_2 = C_{2p}(\frac{1 + {Q_L}^2}{{Q_L}^2})$$

As can be shown in Figure. 6, after the secondary coil tuning, the resonance frequency of parallel tuned secondary is affected by RLP

as below,

$$\omega_o = \sqrt{\frac{1}{L_2 C_2} - \frac{1}{{R_{Lp}}^2 {C_2}^2}}$$

After transforming RLP to series and if the value is small enough, the following equation will be set,

$$\frac{1}{{R_{Lp}}^2 {C_2}^2} > \frac{1}{L_2 C_2}$$

With this condition, series tuned method can be used in various power applications.

By using equivalent circuit analysis, the coupled coil circuit can be represented as simple circuit with equivalent impedance loaded.

$$Z_{2T} = R_2 + R_L + \frac{1}{j\omega C_2}$$

$$Z_{eq} = -j\omega k^2 L_1 + \frac{1}{\frac{1}{j\omega \left(\frac{k}{n}\right)^2 L_2} + \frac{1}{\left(\frac{k}{n}\right)^2 Z_{2T}}}$$

$$= -j\omega k^2 L_1 + \frac{1}{\frac{1}{j\omega k^2 L_1} + \frac{1}{\left(\frac{k}{n}\right)^2 Z_{2T}}}$$

$$= \frac{\omega^3 k^2 L_1 L_2 C_2 [\omega C_2 (R_L + R_2) + j(1 - \omega^2 L_2 C_2)]}{\frac{1}{j\omega k^2 L_1} + \frac{1}{\left(\frac{k}{n}\right)^2 Z_{2T}}}$$

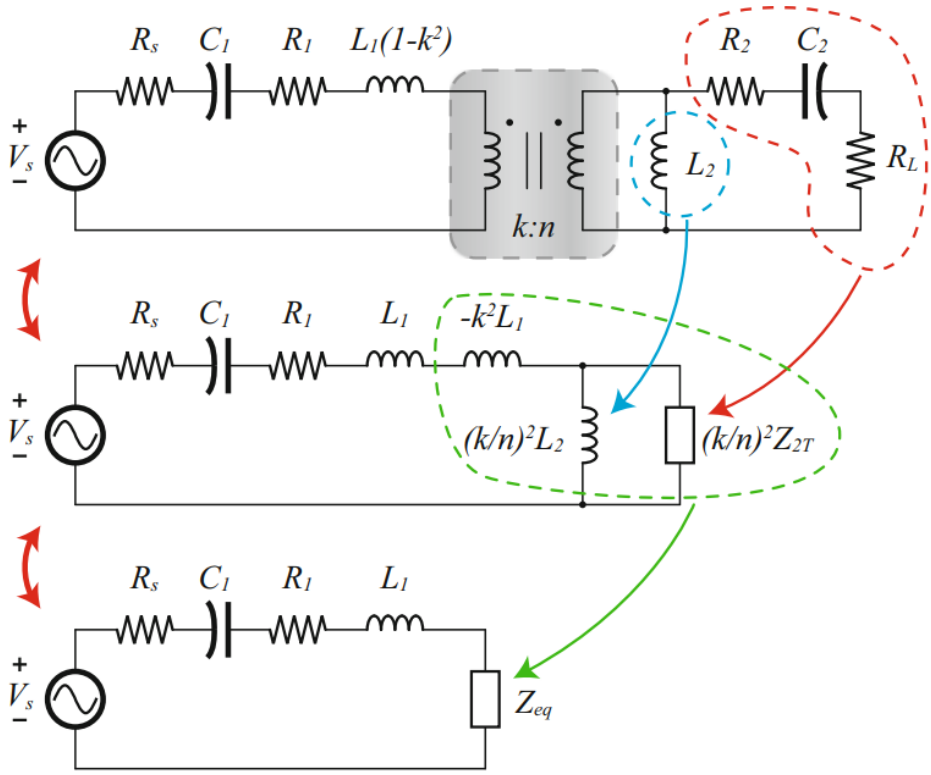

Figure 20 Equivalent circuit of coupled coil circuit

At resonance frequency, following equivalent circuit could be depicted as following equations,

$$@\ \omega = \omega_0 = \frac{1}{\sqrt{L_2 C_2}}$$

$$Z_{eq}|_{\omega_0} = \frac{k^2 L_1}{C_2(R_L + R_2)} = R_{eq}$$

$$R_{eq} = \frac{k^2 L_1}{C_2(R_L + R_2)} = \frac{k^2 L_1}{C_2}\frac{R_L R_2}{R_L + R_2}\frac{1}{R_L R_2} = \left(\frac{k^2 L_1}{C_2 R_2}\right) // \left(\frac{k^2 L_1}{C_2 R_L}\right)$$

$$P_{out} = {V_{eq}}^2 \left(\frac{C_2 R_L}{k^2 L_1}\right)$$

$$V_{eq} = V_s \left(\frac{R_{eq}}{R_s + R_1 + R_{eq}}\right) = V_s \left(\frac{k^2 L_1}{C_2(R_s + R_1)(R_L + R_2) + k^2 L_1}\right)$$

$$\therefore P_{out} = {V_s}^2 \left(\frac{k^2 L_1 C_2 R_L}{[C_2(R_s + R_1)(R_L + R_2) + k^2 L_1]^2}\right)$$

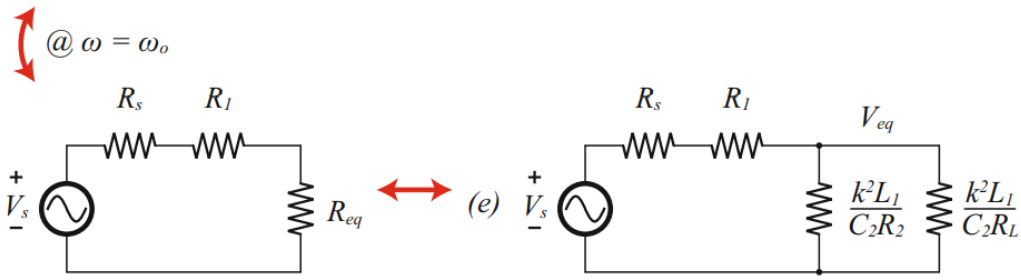

Figure 21 Equivalent circuit at resonance frequency

For maximum power transfer, following equation should be validated,

$\frac{\partial P_{out}}{\partial R_L} = 0$

With this condition, the optimal value of load resistance can be set as follow,

$$\therefore R_{L,opt} = R_2 + \frac{k^2 L_1}{C_2(R_s + R_1)}$$

$$@\ R_s = 0,$$

$$\Rightarrow \quad R_{L,opt} = \frac{\omega L_2}{Q_2} + \frac{k^2 Q_1}{\omega C_2} = \frac{1}{Q_2}\sqrt{\frac{L_2}{C_2}} + k^2 Q_1 \sqrt{\frac{L_2}{C_2}} = \sqrt{\frac{L_2}{C_2}}\left(\frac{1 + k^2 Q_1 Q_2}{Q_2}\right)$$

$$= \omega_0 L_2 \left(\frac{1 + k^2 Q_1 Q_2}{Q_2} \right)$$

So that for the efficient power transfer, the optimal load resistance can be expressed with quality factors of inductors, coupling factor and values of capacitors and inductors. By selecting optimal value of resistance of each part of the system, it was possible to design the system that could deliver power efficiently [59].

2.1.3 Wireless Power Transmission Circuit

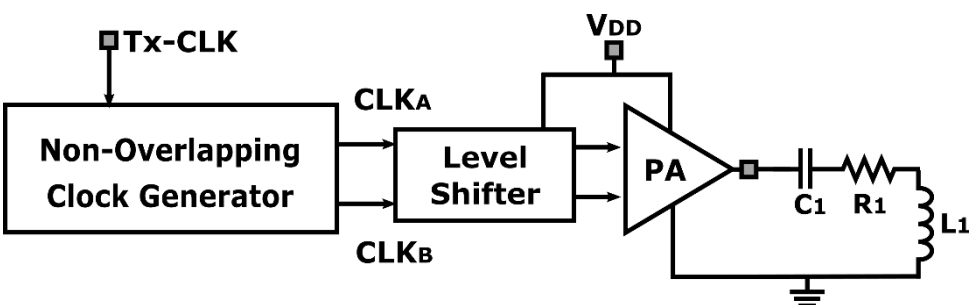

Figure 22 Power transmitter system

The wireless power transmitter circuit is composed of non-overlapping clock generator with tapered buffer power amplifier. From non-overlapping clock generator, two clock signals that doesn't overlapped. This clock signal is generated from external master Tx

clock according to the selected carrier frequency fp. By passing tapered buffer and level shifter, the generated clock signals stepped up to external VDD. Then the Class-D PA generates power carrier signal depending on the output power level.

Amplifiers are classified mainly into class-A, AB, B, C, and D depending on the bias. The Class-D amplifier uses pulse delay modulation and has high efficiency, but peripheral circuits may be complicated, and switching noise is easy. Unlike other amplifiers, the Class-D amplifier is not a linear method but a method of controlling and amplifying a signal by varying the switching time according to the signal. That is, the pulse width is adjusted by changing the switching time. Linear amplifiers have a simple structure, low noise, and good frequency characteristics but have disadvantages in that they generate heat easily and increase in volume due to low energy efficiency. On the other hand, the Class-D amplifier has a complex structure but can achieve up to 90% energy efficiency and can be designed in a small size. After the power amplifier, the first transmitting power tank with coil is placed [60].

a) Non-overlapping phase generator

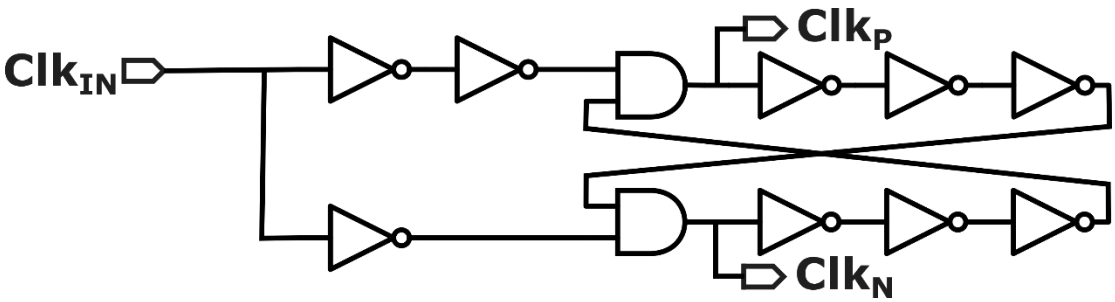

Figure 23 Non-overlapping phase generator

Non-overlapping phase generators are required to use switched capacitor circuit system to provide two non-overlapping clock phases to charge and discharge flying capacitors. The non-overlapping phase generator for those clock signals are consisted of NAND based inverter chains, which is the conventional method. This type of non-overlapping clock generator is advantageous for switching high frequency signals [61].

b) Tapered buffer

c)

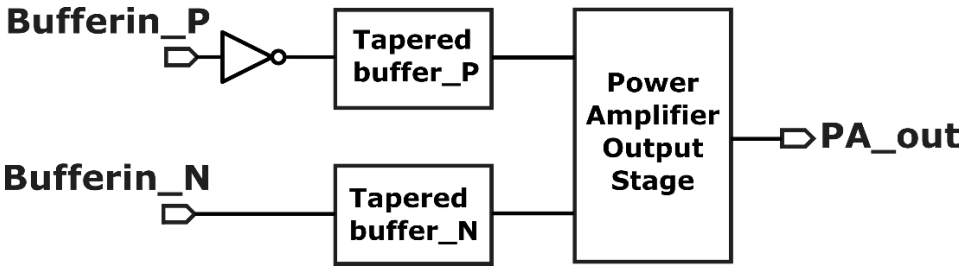

Figure 24 Tapered buffer diagram

The tapered buffer is enlarged to about six times in size to drive the output stage of the Class-D PA.

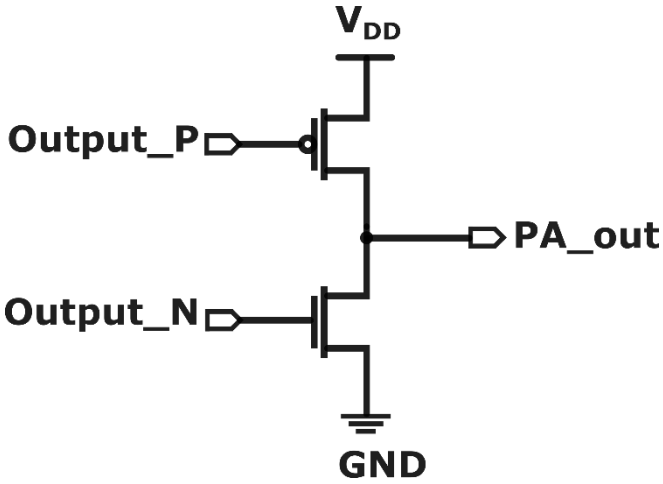

Figure 25 Power amplifier output stage

For the Class-D PA optimization, losses due to switching power amplifiers should be considered. First, conduction losses are generated

due to power dissipation from the resistance value of semiconductor devices, inductors, or capacitors. However, this power dissipation doesn't affect by the high-frequency band, and depending on the skin depth due to the size of the device, these losses could be varied. For example, a wide, flat, and short connection can reduce conduction loss and parasitic lead inductance.

Secondly, turn-switching losses should be considered. At the turn-on point, the voltage decreases from the initial value, and the current increases from 0. So that section, called 'cross over,' appears since the voltage doesn't drop instantaneously. Therefore, the power dissipation according to this phenomenon is proportional to the length of the cross-section and the switching frequency of each turn-on loss of the switching cycle. This can also be expressed as the loss generating because of the charge dissipation at the output capacitor, the intrinsic capacitance of the device. Since the intrinsic capacitance cannot be reduced to 0 in real, the zero-voltage switching method is the most efficient way to reduce this.

Another loss is the so-called turn-off switching losses. Unlike the turn-on point, during the turn-off period, there is no other capacitor

voltage generated from charge dissipation. However, the loss comes from parasitic inductance due to currents flowing through the leads or wire bonds. This loss can be reduced by designing circuit layout efficiently or using a low lead inductance package.

Finally, there will be gate drive losses. As the frequency band increases, the power dissipation increases due to charging and discharging the gate capacitance. The gate drive losses may vary depending on the shape of the power signal used for gate driving. Using the square-wave drive as an example, the same amount of energy will be lost through the resistor while the gate is charged through the resistor. So the power loss from the gate drive can be reduced by lowering the drive resistance.

For better efficiency, zero-voltage switching Class-D PA needs to be designed. From the power amplifier's output stage, when the top device turns off, the bottom device remains turned off; this situation creates so-called ‘dead time.’ When the resonance load circuit phase lags, the current flows through the capacitive circuit—making one side capacitor discharged while the other capacitor charged. When the bottom device is turned on and off, this procedure charges a lower

capacitor and discharges the upper capacitor. To manage zero-voltage switching in Class-D PA, controlling the dead time, peak current in the device, and load phase angle to the fundamental component of the voltage is crucial. If the dead time is too short or long, there will be a loss since the output voltage doesn't go down to 0. When the voltage discharge is fully done due to low current amplitude, there will be a loss because of the insufficient discharged voltage. In the opposite case, when the current amplitude is too large, the output voltage crosses the 0 value twice, transferring reverse polarity to the device. This holds negative voltage to the MOSFET body, turning on the body diode, which might break the device [62].

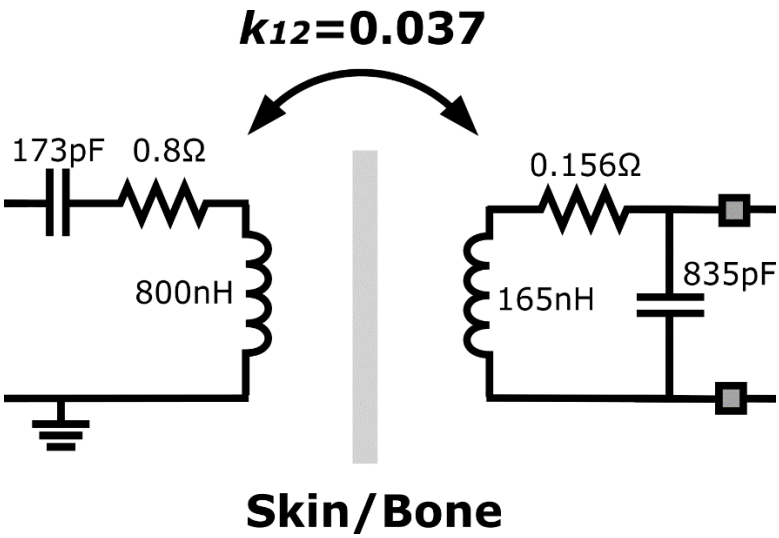

Figure 26 Power tank parameters

The parameters of the power tank were set considering the limited implantable space for the artificial retina. Due to the structure of the artificial retina, the maximum size of both external and internal coils is limited. Since the subretinal way was chosen in this work to insert electrodes between retina tissues. The maximum thickness and diameter of the inner coil are restricted up to 1.5mm and 15mm, respectively. Also, the distance between two coils must be placed within up to 10mm, filled with biological tissues such as skin, bone, or fat. Within these restricted environments, we have to achieve the proposed minimum goal or even more for further development.

Table 3 Power tank parameters under implantation conditions

	1st Coil part	2nd Coil part
Maximum outer D (mm)	30	15
Quality factor	85	80
Line width (mm)	1.5	1
Spacing (mm)	0.2	0.2
Number of turns	8	4
Inner D (mm)	3	5

L (nH)	800	165
C (pF)	173	835
R (Ohm)	0.8	0.1562

Within the limitation of maximum outer diameter for both coils in the power transmitter part, the maximum inductance and quality factor can be derived. Since the first coil doesn't have to be implanted for the transmitter, the consisted material can be set as a standard PCB board with copper winding. While the second coil, which needs to be implanted inside, needs a biocompatible system. In this case, we assumed cyclic olefin copolymer as a substrate with gold winding trace for a planar spiral coil pattern. According to series-parallel tuning method to get optimal value, the inductance, capacitance and resistance of power tank decided. With respect to the optimal equivalent value of resistance after the power amplifier, the power transferred to the optimal load was over 80mW.

Table 4 Designed power coils specifications

Unit: mm	L1	L3
Substrate height (H)	0.1	0.1
Winding trace width (W)	0.45	0.45
Winding trace thickness (T)	0.01	0.01
Inter-winding gap (S)	0.2	0.2
Outer inductor diameter (Do)	30	13
Number of turn (N)	7.5	8.5
Test frequency (f)	13.56MHz	13.56MHz
Inner inductor diameter (Di)	20.65	2.35
Inductance	818.18nH	165.12nH

The inductive link specifications for both power and data transmission can be found in Table 1. The planar spiral coil has several variables that need to be set for higher quality factors and inductance within limited space. From the circuit level simulation, the power tank coupling was set at 0.037, considering the harshest implant environment.

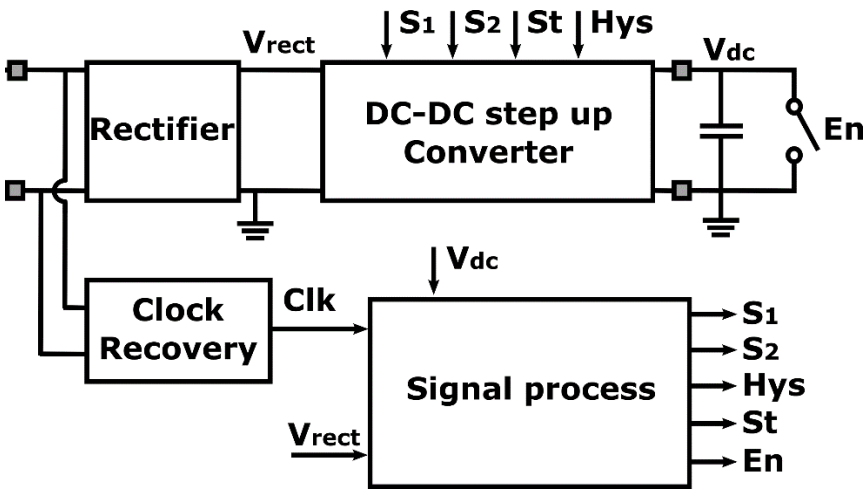

Figure 27 Power receiver diagram

The wireless power receiver consists of the rectifier, clock recovery system, signal process part, and finally main reconfigurable DC-DC step-up converter.

a) Rectifier

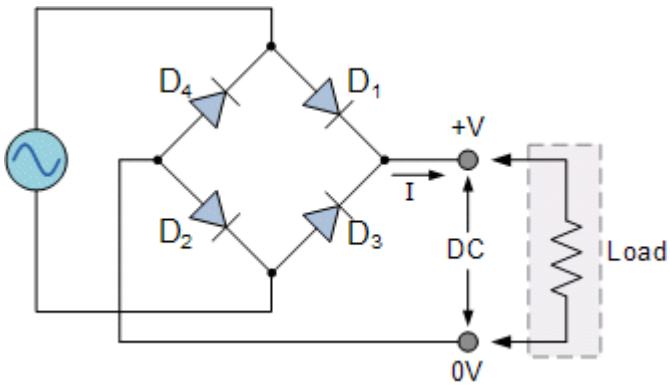

Figure 28 Conventional full-wave rectifier using diodes [63]

There are full-wave and half-wave rectification methods for converting AC (alternating current voltage) to DC (direct current voltage). Both are rectified using the characteristic that current flows only in the diode's forward direction.

Full-wave rectification converts the negative voltage of the input voltage into a positive voltage and rectifies it to direct current (pulsating current) by composing a diode as a bridge circuit. On the other hand, half-wave rectification removes the negative input voltage with one diode and converts it into direct current (pulse current). After that, using the axial discharge of the capacitor, the waveform is smoothed to convert it to a clean direct current.

Therefore, compared to half-wave rectification, which does not use a negative input voltage, full-wave rectification can be said to be a more efficient rectification method. Also, the ripple voltage that appears after smoothing changes depending on the capacitor capacity and the load. If the capacitor capacity and load are the same, the full-wave rectification will have a smaller ripple voltage in full-wave rectification and half-wave rectification. Of course, the smaller these ripple voltages are, the more stable they are [64].

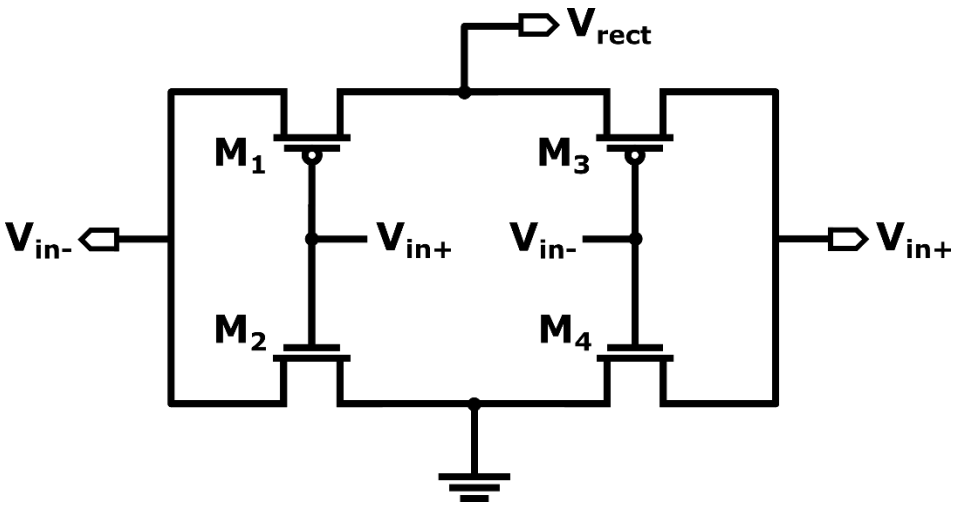

Figure 29 Full wave rectifier diagram

The conventional rectifier using a diode is unsuitable for integration, and it is difficult to expect high efficiency because of the voltage drop due to the diode's large voltage. Therefore, interest in full-wave rectifiers using MOSFET switches instead of diodes, as shown in Figure 19, has been drawn to improve efficiency. This rectifier has almost no voltage drop between the input and output voltage because all MOSFETs operate only as switches. However, when operating as a switch, leakage current occurs because the current cannot be interrupted [65].

b) Low drop out voltage regulator (LDO)

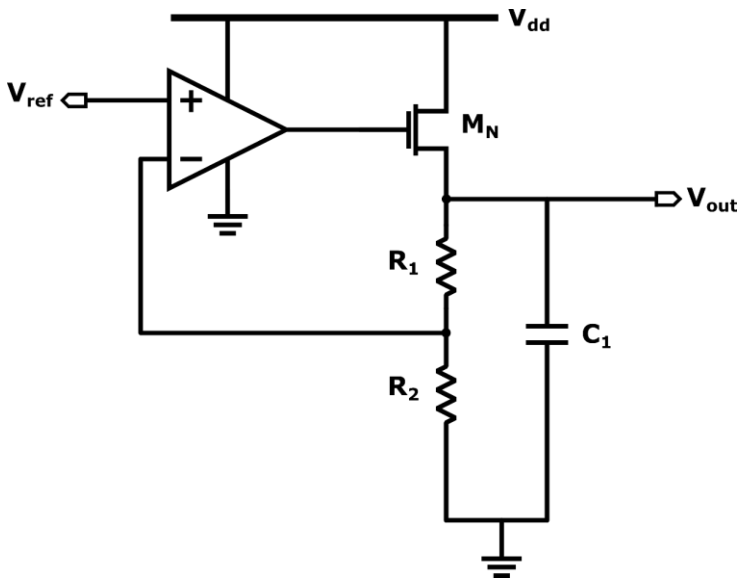

Figure 30 Low drop out voltage regulator diagram

Low drop out voltage regulator can provide 1.8V supply voltage for those MOSFETs used in data transmission circuit. The output of LDO is independent from variation of the temperature. It is a linear regulator that operates even with a low input/output potential difference. Also called low loss type linear regulator and low saturation type linear regulator. Although there is no numerical definition of the input/output potential difference of an LDO, it generally means that the minimum potential difference at which the regulator operates stably is

suppressed to 1V or less. For example, in the case of an IC that requires a 3.3V power supply, an LDO with a low input/output potential difference is required because the standard type cannot generate a 5V to 3.3V power supply. This way, the input voltage can be set low even when the LDO outputs the same voltage as a standard-type regulator. By operating at a low potential difference, it is possible to design a design that suppresses heat generation due to low energy loss [66].

Figure 30 shows a classic diagram of the low dropout voltage regulator. It comprises a pass MOSFET with an error amplifier and a resistor feedback network. The voltage divider, the resistive feedback network, provides a scaled output voltage according to the input reference voltage. The error amplifier compares the reference voltage to the feedback voltage coming from the voltage divider. The error amplifier also amplifies the difference between two voltage signals, and the pass MOSFET is driven to keep the output voltage at a specific level.

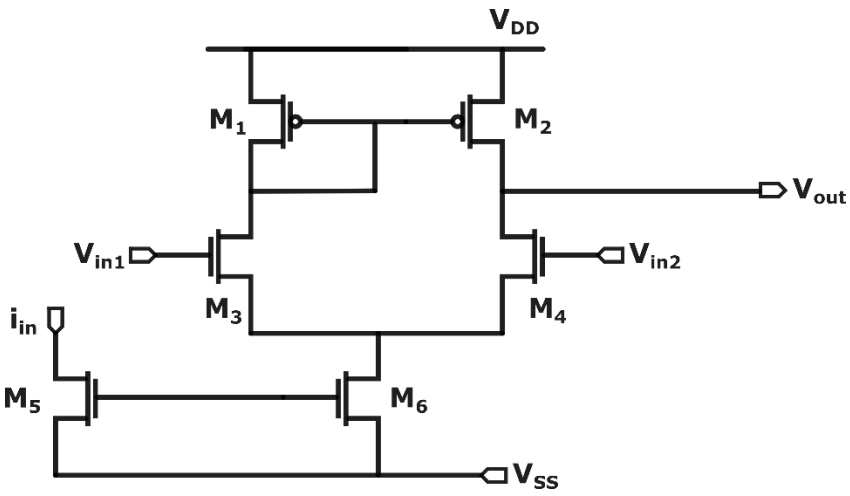

Figure 31 Error amplifier diagram

One of the most important parts of LDO is the error amplifier, which should draw a small current as much as possible. Since the gate capacitance of the pass MOSFET is large, the resistance of the amplifier should be low. The error amplifier has two inputs: reference voltage and output voltage scaled by the voltage divider. The error amplifier constantly compares these two signals and adjusts the resistance of the pass MOSFET [67].

The pass MOSFET in LDO transfers current from input to load and is driven by the error amplifier through a feedback loop. The advantage of using NMOS for the pass element is that it is in source follower configuration. Also, the regulator's output is at the transistor's source.

With this layout, the LDO can take low input and dropout voltage. The difference between the input and output voltages of the error amplifier is defined as dropout voltage. The regulator stops regulation when the input voltage gets close to the output voltage.

Finally, the output capacitor ensures the current is delivered directly to the load during load transients until the error amplifier returns to the ready state.

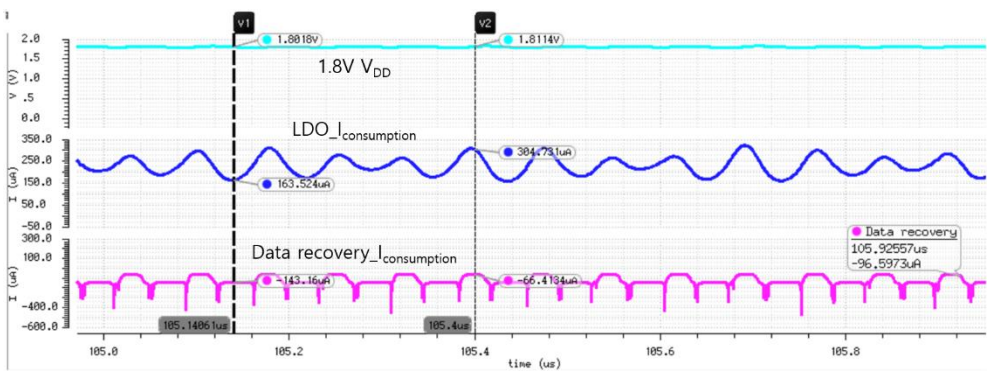

Figure 32 Output voltage and driving current of LDO

As shown in Figure 32, the designed LDO's output voltage (1.8V V_{DD}) maintaining maximum 20mV of ripple voltage. The ratio between R1 and R2 is set as 1:2 with C1 as 80fF. The output voltage of LDO is set as 1.8V with a 10mV ripple. And the error amplifier draws 84uA current with 78dB of gain, and the current drawing through the pass

transistor is up to 220uA. Summing up those two currents, the total current drawing from the designed LDO is 160~300uA. The LDO is loaded with our data receiver system and supplied with a 5V voltage signal with AC ripple. The average current drawing from the data recovery system (which will be discussed in 2.1.4 Figure 78).

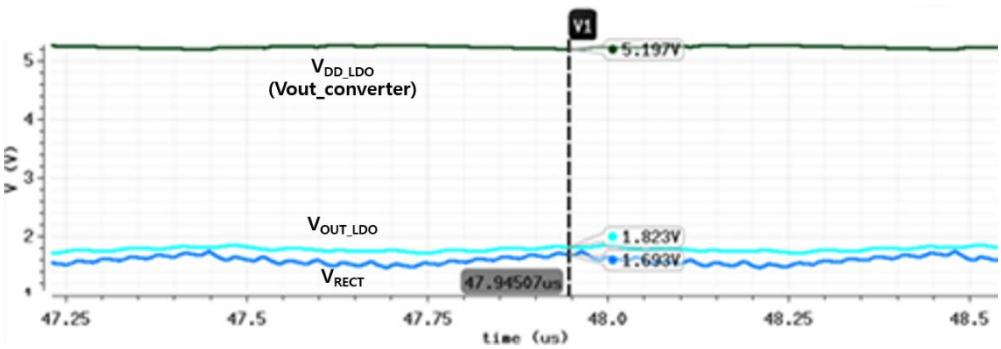

Figure 33 Input/Output voltage waveform of LDO

Figure 33 shows the input and output voltage waveform of the LDO. During the measurement, with the variation of V_{RECT} as an input voltage ranges from 1.6V ~ 3.3V, the output of the LDO(V_{OUT_LDO}) constantly maintains 1.8V with a 5V supply voltage(Vout_converter).

c) Clock recovery

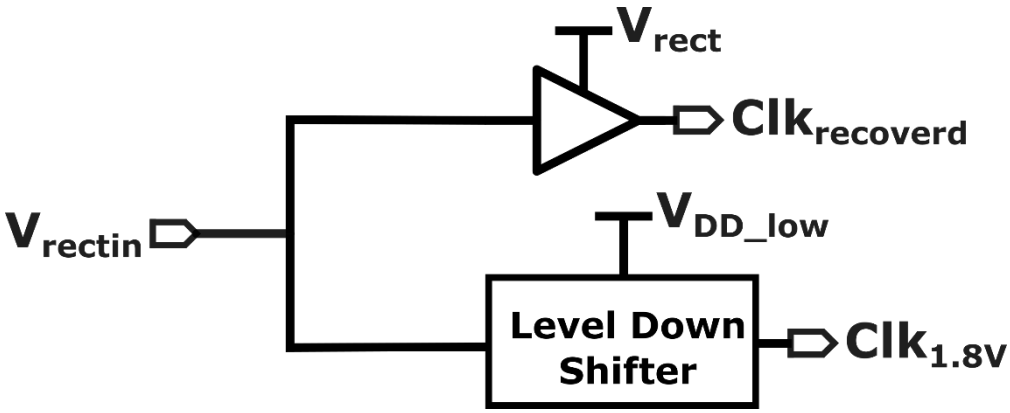

Figure 34 Clock recovery system

The Clk_recovered signal is the square of the input signal of the rectifier with an inverter, and it is used as the internal clock signal of the DC-DC step-up converter. The CLK_1.8V that passed the level-down shifter in the rectifier input signal is used as the standard 1.8V recovered clock of the data recovery stage. Level down shifter consists of a 5V buffer chain.

2.1.3.1 Reconfigurable Step-Up Converter

The DC-DC step-up converter stage can be divided into two parts. It is divided into the main converter stage and the signal process part that controls the main converter stage.

2.1.3.1.1 Start-Up, Auxiliary Circuit

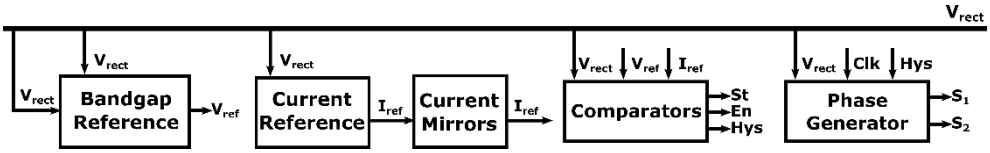

Figure 35 Signal process system

In the signal process part, there is a part that controls the output voltage through the start-up and driving process of the main converter stage, a part that adjusts the magnification of the converter stage, and a part that makes a standard current.

i) Band gap reference

Many analog circuits require a voltage or current that is not affected by temperature. However, since most process parameters are affected by temperature, the reference must be temperature-independent. The band gap reference consists of an error amplifier with a high gain—conventional current bandgap reference. The conventional current band gap reference was used. The basic principle of the bandgap reference circuit is to make a constant voltage output even when the temperature changes by adding or subtracting an element that

has a characteristic in which the voltage decreases when the temperature rises (Complementary To Absolute Temperature, CTAT) and an element (Proportional To Absolute Temperature, PTAT) that has a characteristic in which the voltage increases when the temperature rises [68].

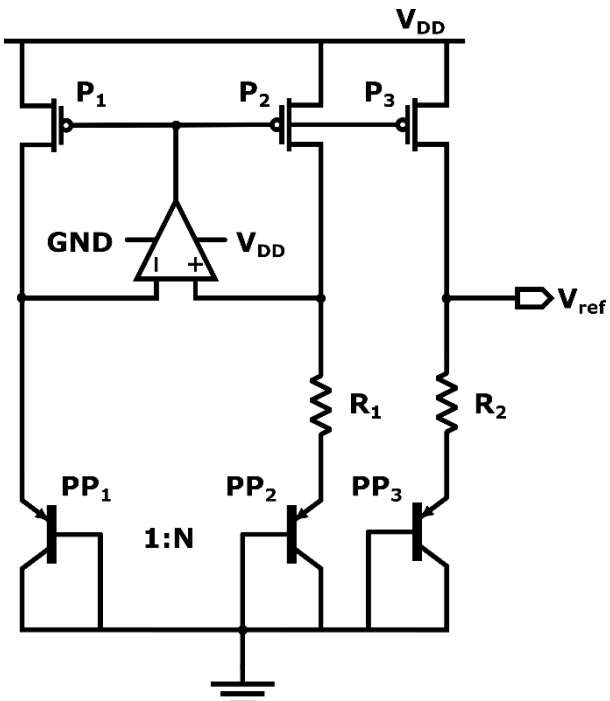

Figure 36 Current band gap reference circuit diagram

As shown in Figure 36, you can check the bandgap reference circuit diagram that is insensitive to fluctuations in process voltage temperature (PVT) and is advantageous for low voltage operation. This

is because it creates a constant reference current with respect to temperature change, and this current flows through the resistor R2 connected to Vref, making a constant voltage insensitive to PVT fluctuations.

Table 5 Specifications of error amplifier for bandgap reference

Vdd	1.5V	3V
Gain (A_v)	80dB	72dB
Cut-off frequency (f_c)	1.5kHz	5kHz
Phase margin (PM)	62°	63°
Bias current (I_{BIAS})	18uA	21uA

Table 5 shows the specifications of error amplifier that used for bandgap reference. Due to the V_{DD} variation coming from the rectifier, the bandgap reference should work in the supply voltage range of 1.5V ~ 3V. The reference voltage from the bandgap reference system was set as 1.2V.

Figure 37 Monte-Carlo simulation of band gap reference

This reference voltage through Monte-Carlo simulation has a standard deviation of 38.1875mV. As a result of simulating 1000 sample points, 89% passed.

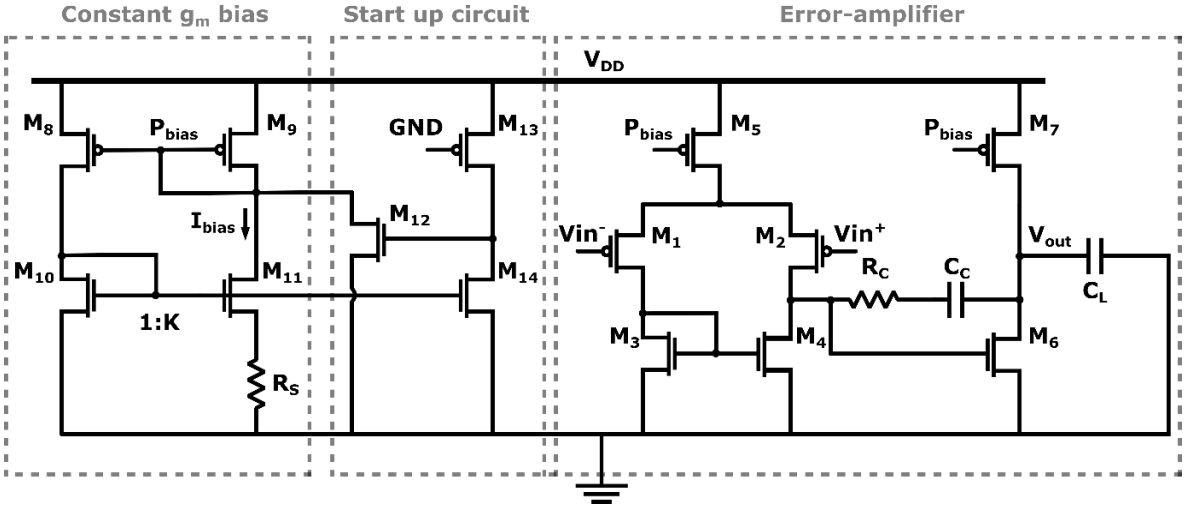

Figure 38 Error amplifier with constant gm bias cell diagram

The constant gm bias cell is a system that can keep the gm constant in the process variation or temperature change [69]. Therefore, it helps to keep the reference current of the amplifier stage constant without being fluctuated. Inside the constant gm bias cell, there is a start-up part that allows the system to be turned on all the time and prevents current from leaking in a high resistive state. From the constant gm bias start up circuit, the transconductance of M10 is determined by Rs and geometric ratios only, independent of power-supply voltages, process parameters, temperature, or any other parameters with large variability. Not only gm13 stabilized, but all other transconductances are also stabilized since all transistor currents are derived from the same biasing network, therefore, the ratios of the currents are mainly dependent on geometry.

ii) Current reference

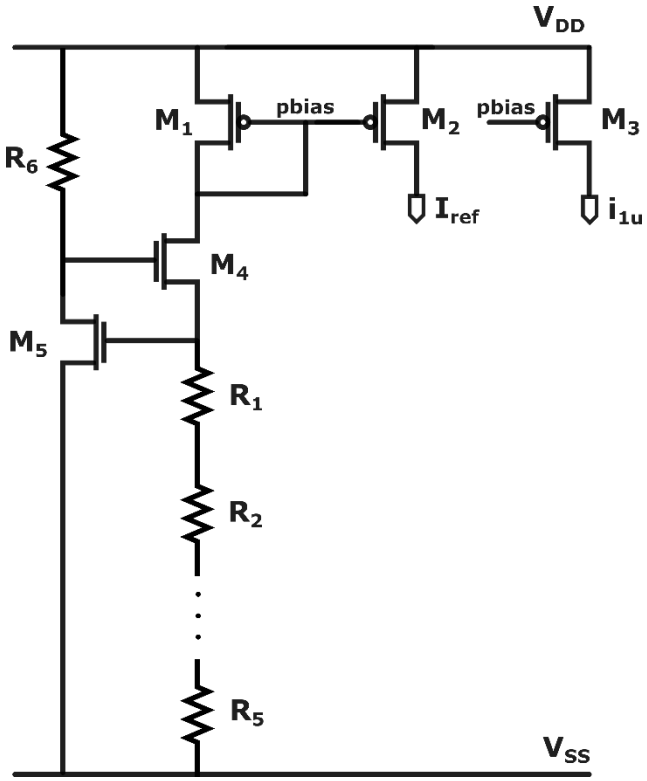

Figure 39 Current reference

The current reference parts for working well are the operation control and magnification selection parts of the converter stage [70]. Current reference is a conventional current reference using a resistor. PMOSFETs M1 and M2 act as a current mirror and are in strong inversion. M4 and M5 are in weak inversion region.

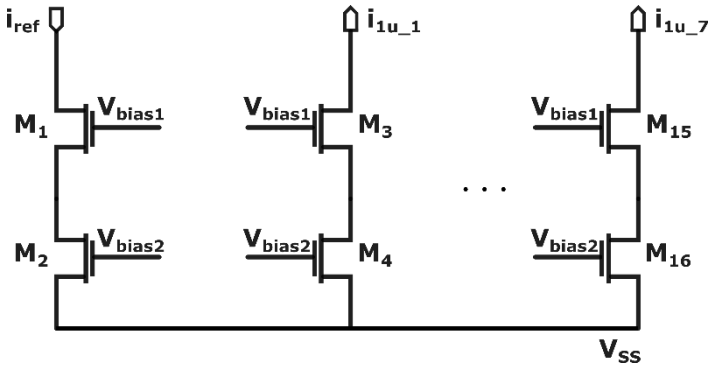

Figure 40 Current mirrors

The current reference is mirrored to each active part through the current mirrors. The reference current can be mirrored more accurately with the cascode-type current mirror.

iii) Hysteresis controller & Enable signals

The part with the hysteresis controller and enable signals consists of comparators and resistors to control each operating range.

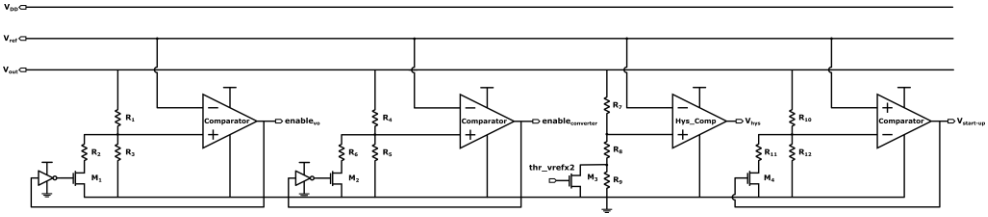

Figure 41 Hysteresis controller & Enable signals

First, the step-up converter enabler is composed of a two stages comparator and divided resistor so that when the converter stage output voltage Vo is stabilized to a value close to Vrect (about 2.4V), the step-up converter enabler is activated so that the main converter switch can be turned on properly. Then the step-up converter enabler charges the output capacitor to a sufficiently high voltage.

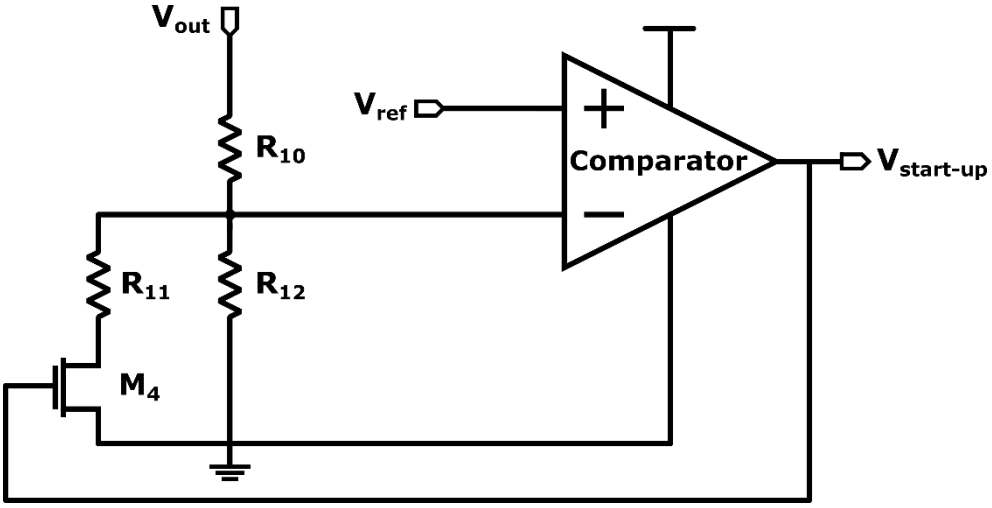

Figure 42 Step-up converter enabler

The hysteresis controller stage maintains the desired average output voltage value of around 5V with ±2.5% ripple to maintain the output voltage value of the converter stage after reaching 5V. It has a feedback loop to control output voltage within set range of ripple. DC-

DC converters must provide a regulated DC output voltage under various load and input voltage conditions. In addition, the transducer component values change with time, temperature, pressure, etc. Therefore, the output voltage control must be done in a closed-loop manner using the negative feedback principle. The converter output voltage is sensed and subtracted from the external reference voltage of the error amplifier. The error amplifier generates a control voltage compared to a sawtooth waveform of constant amplitude.

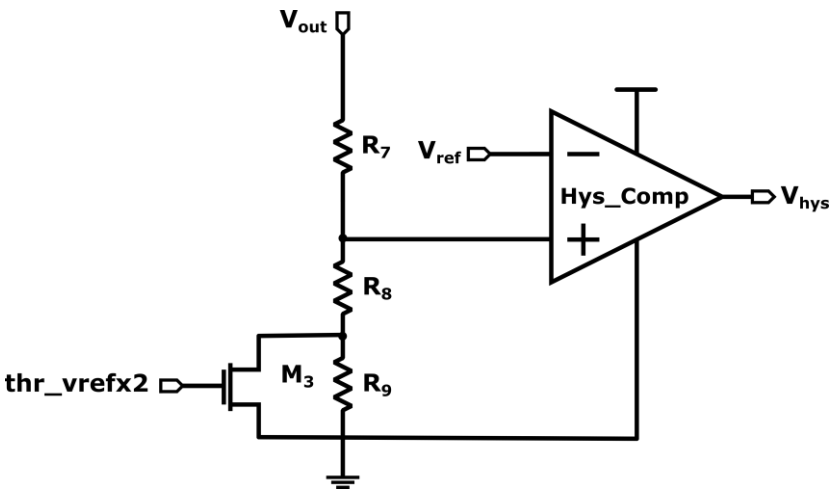

Figure 43 Output voltage hysteresis controller

Initially, with the output switch open, a start-up circuit enabler

connects the converter input to the output, allowing the rectifier to charge the output storage capacitor directly.

A non-overlapping clock generator also allows a switch in the main converter stage to generate a signal to increase the voltage by turning it on and off in different phases. The input voltage of thr_vrefx2 to control the series resistance of voltage divider comes from gear top unit (Figure 51).

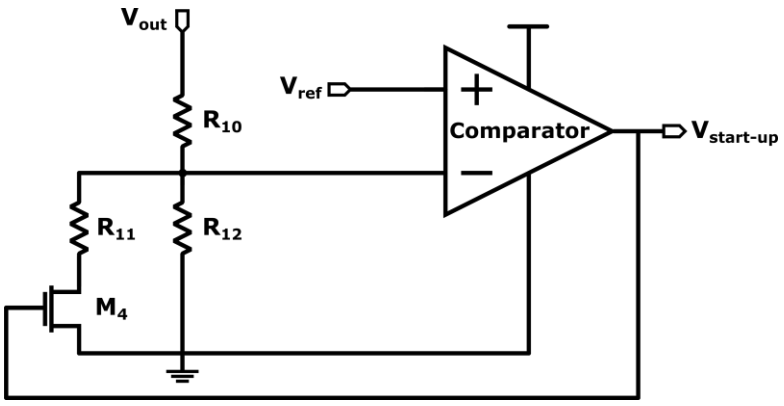

Figure 44 Start-up circuit enabler

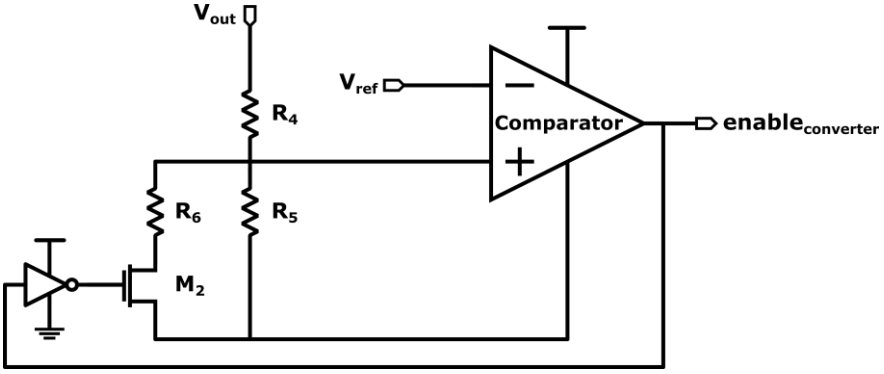

Figure 45 Step-up converter switches enabler

Each switch driver inside the step-up converter is controlled with a non-overlapping clock generator and converter switch enabler signal. Make sure the converter switches are properly turned on during the turn-on transient.

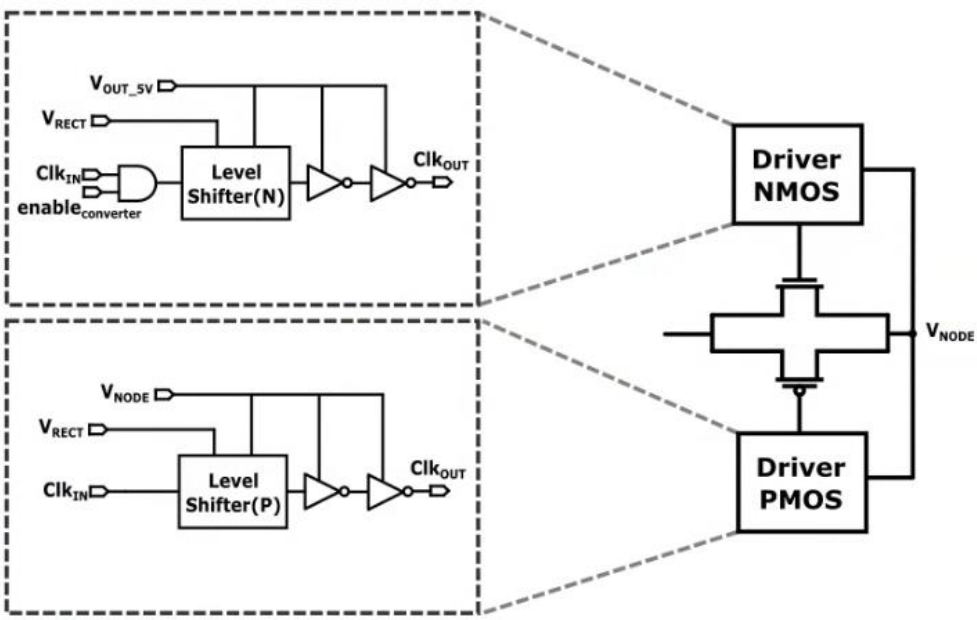

Figure 46 Switch driver

VDD supply voltage of the gate drivers is taken either from the output voltage of the step-up converter (upper driver in Figure 46) or from the node to the right of the switch V_{NODE} (lower driver in Figure

46) to guarantee that the switches work correctly also during the turn-on transient. The VSS for all switch drivers is set as 0V. Since the output voltage of the step-up converter will be maintained as 5V in every voltage ratio (n = 2, 3, 4,5) thanks to hysteresis controller unit (from Figure 42) within ±2.5% ripple, making operating switches turn on and off during each phase. Each width of the pump switch for the step-up converter gets larger as the voltage pumps up. To properly drive each switch with the switch driver, the buffer unit of the driver should get large enough.

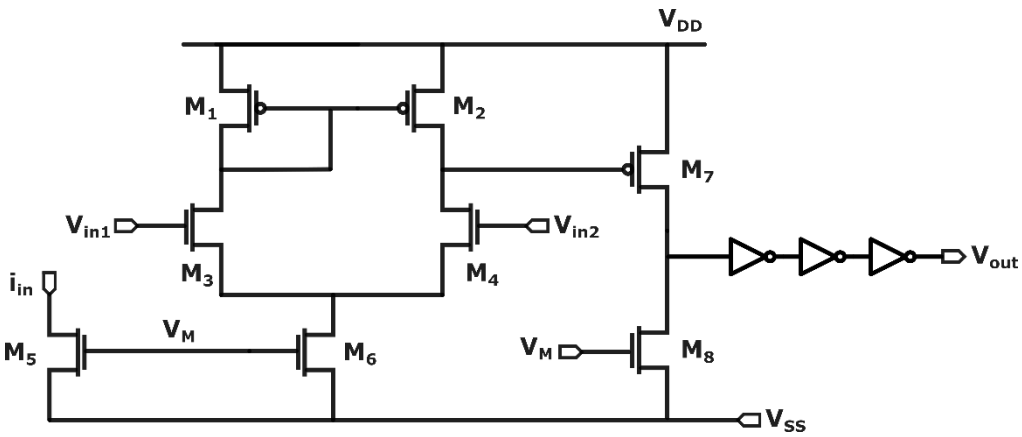

Figure 47 2-stages comparator

A 2-stage comparator consists of a differential amplifier and a common source amplifier. Therefore, increasing the gain and slew rate is possible according to the frequency band.

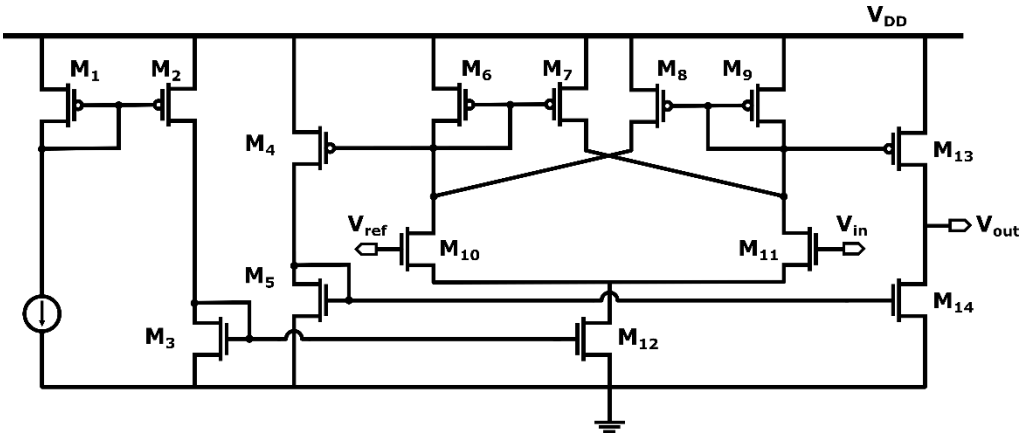

Figure 48 Hysteresis comparator

The hysteresis comparator adjusts the value to be maintained between about 5.1V and 4.9V when the output voltage exceeds 5V based on the reference voltage. A comparator having a hysteresis circuit is disclosed. The comparator has a differential amplifier circuit and a hysteresis circuit. The differential amplifier circuit generates a first signal by amplifying a difference signal corresponding to a difference between the input signals. The hysteresis circuit sets a first transition threshold voltage and a second transition threshold voltage lower than the first transition threshold voltage in response to the first signal, and when the difference signal rises, it transitions from the first transition threshold voltage, and the difference signal falls. In this case, a second signal that transitions at the second transition threshold

voltage is generated. Accordingly, by providing the hysteresis circuit at the output terminal of the differential amplifier circuit, the comparator can increase the noise immunity without reducing the operable frequency of the input signal [71].

iv) Phase generator

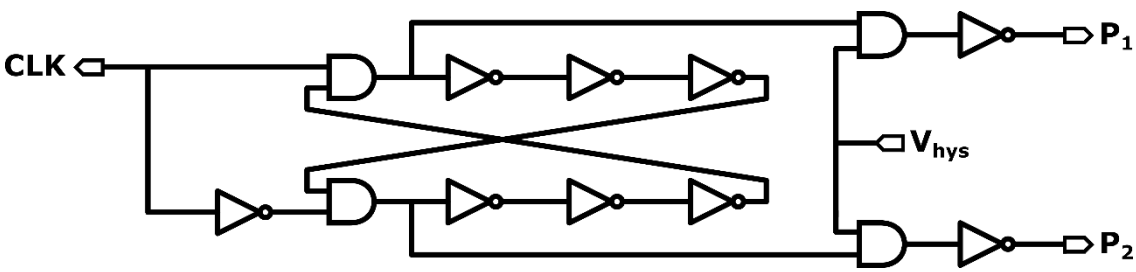

Figure 49 Phase generator

The phase generator includes a phase shift clock signal generator, a duty cycle adjuster, and an injection fixed oscillator. First, the phase shift clock signal generator generates a phase shift clock signal based on the input clock signal. Next, the duty cycle adjuster generates the injected clock signal by adjusting the duty cycle of the phase shift clock signal based on the duty cycle adjustment signal. Finally, the injection-locked oscillator receives an injection clock signal and oscillates to

generate an output clock signal [72].

v) Topology selector (Schedular)

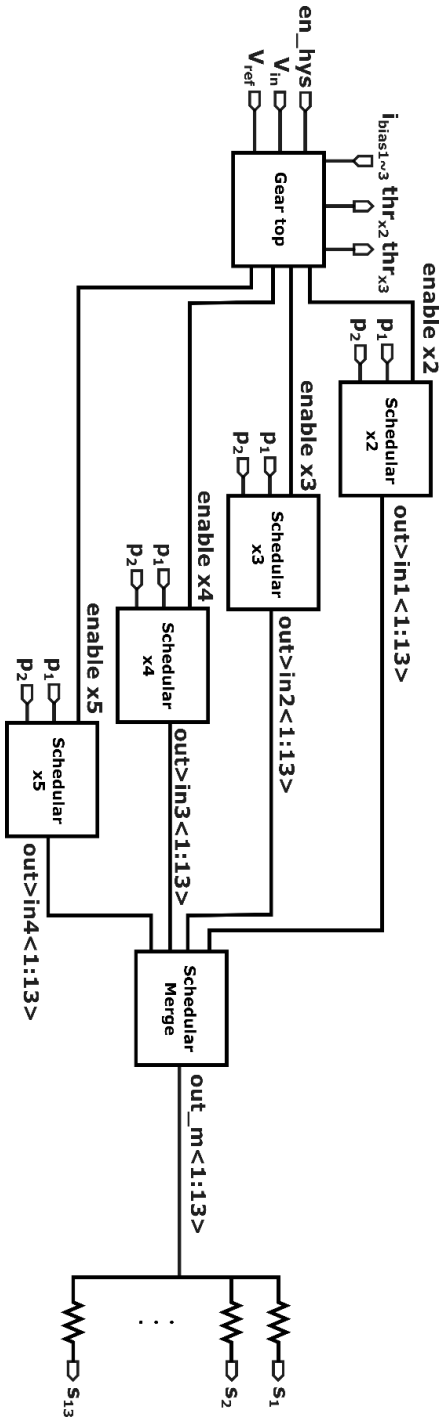

Figure 50 Schedular system

The schedular system to select topology for the main step-up converter can be seen in Figure 50. Depending on the conversion ratios (n = 2, 3, 4, 5) of the converter, the schedular is selected using hysteresis to enable the rectifier's signal, reference voltage, and output voltage.

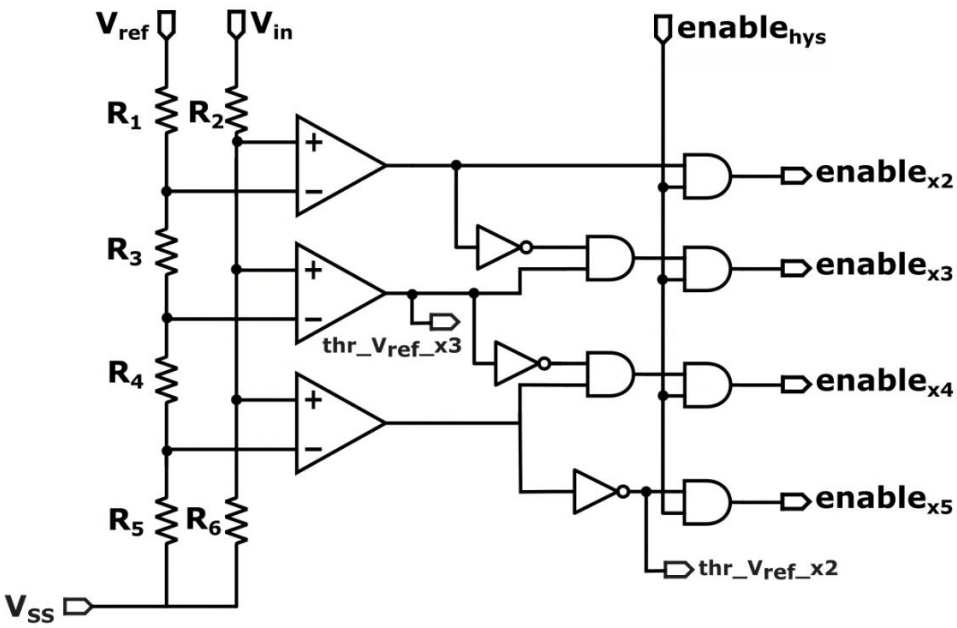

Figure 51 Gear top diagram

The gear top section generates enable signals for each schedular for a conversion ratio. By comparing the input voltage, which is the output voltage of the rectifier, and a reference voltage, the gear top system sorts which conversion ratio needs to be selected for the main

converter to get 5V.

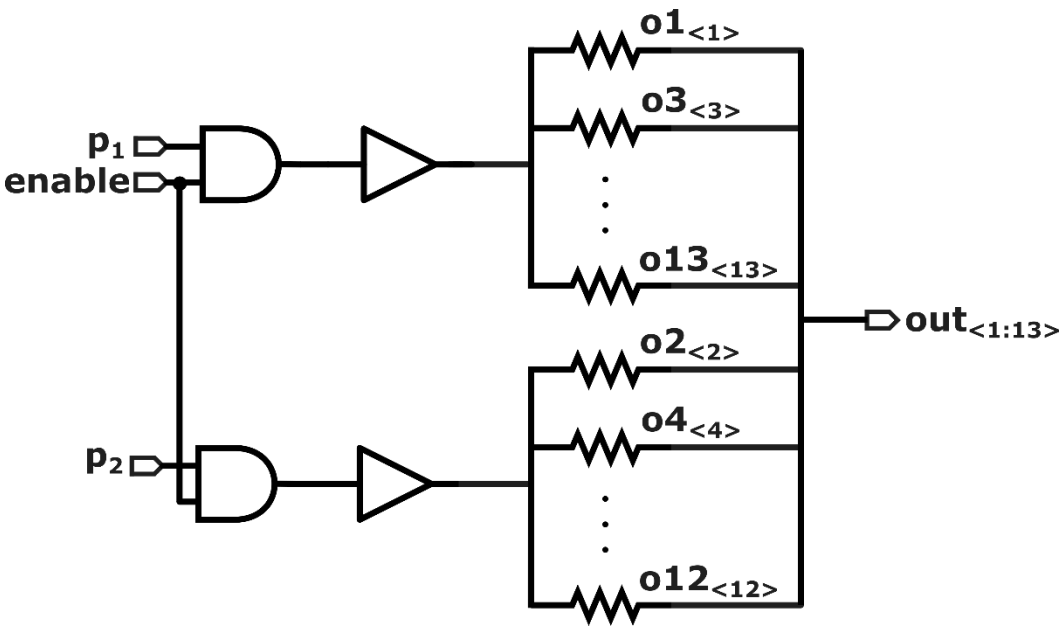

Figure 52 Schedular x5

The schedular for conversion ratio x5 works with two different phases with an enabled signal. Each enable signal is coming from the gear top cell. The driving signal for 13 switches in the step-up converter was generated to step up the input signal by five times bigger. For phase 1, to achieve x5 conversion ratio, S1/S3/S5/S7/S9/S11/S13 have to be turned on, while, for phase 2, S2/S4/S6/S8/S10/S12 have to be turned on.

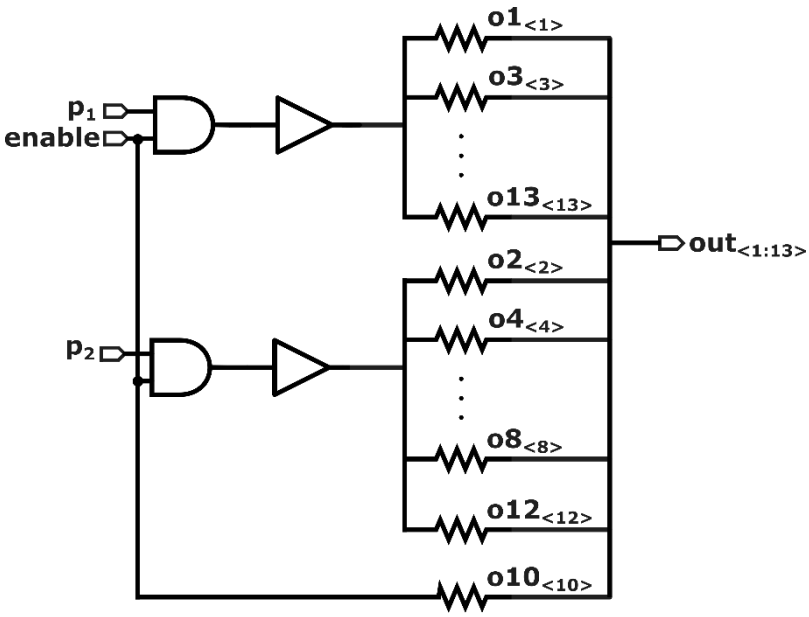

Figure 53 Schedular x4

Similarly, the schedular for conversion ratio x4 also works with two different phases with an enabled signal. For phase 1, to achieve x4 conversion ratio, S1/S3/S5/S7/S9/S10/S12 have to be turned on, while, for phase 2, S2/S4/S6/S8/S10/S11/S13 have to be turned on.

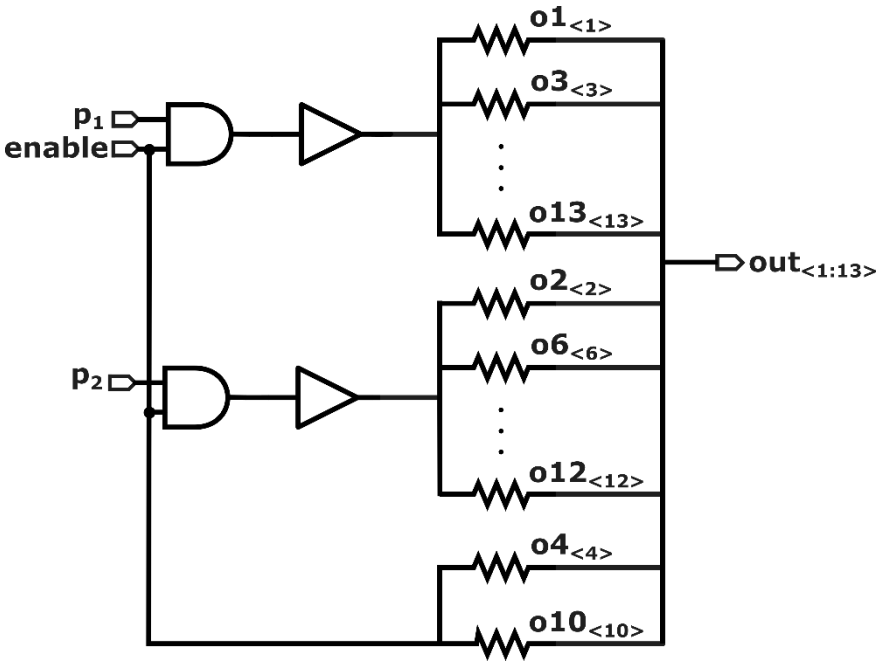

Figure 54 Schedular x3

The schedular for conversion ratio x3 can be seen in Figure 50. For phase 1, to achieve x3 conversion ratio, S1/S3/S4/S6/S8/S10/S11/S13 have to be turned on, while, for phase 2, S2/S4/S5/S7/S9/S10/S12 have to be turned on.

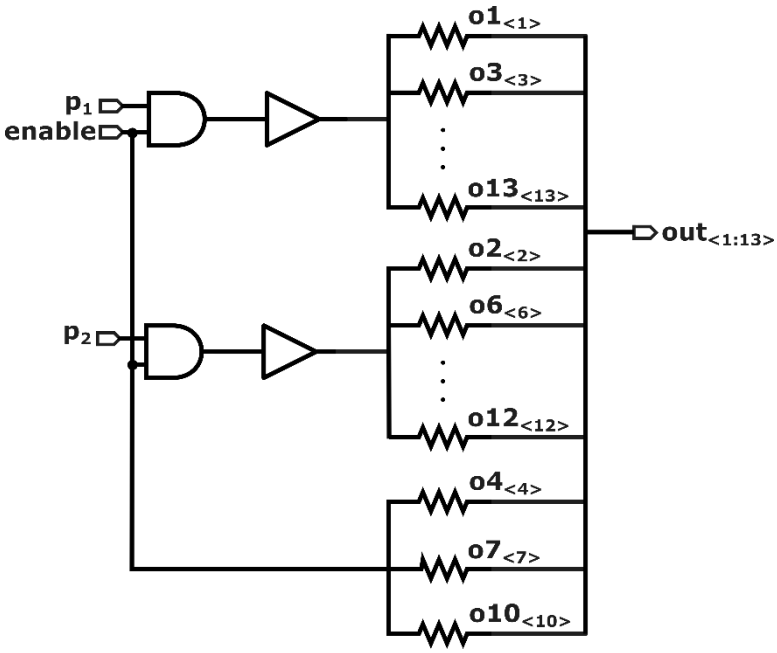

Figure 55 Schedular x2

The schedular for conversion ratio x2 can be seen in Figure 51. For phase 1, to achieve x2 conversion ratio, S1/S3/S4/S6/S7/S9/S10/S12 have to be turned on, while, for phase 2, S2/S4/S5/S7/S8/S10/S11/S13 have to be turned on.

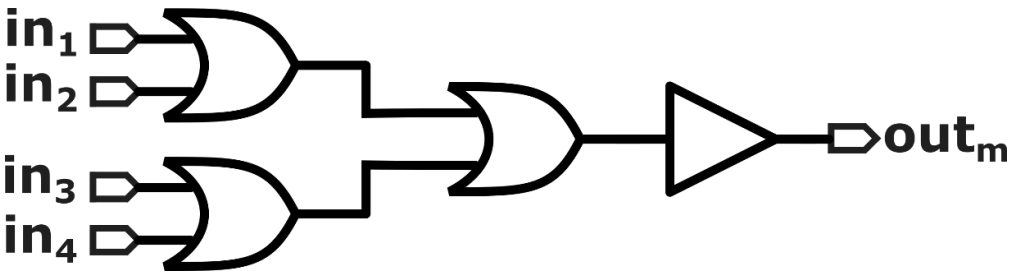

Figure 56 Schedular merge unit

The schedular merge unit merges signals coming out from each schedular units and spread the signal through each switch driver.

2.1.3.1.2 DC-DC Step-Up Converter

IMDs belonging to the class of neural prostheses try to alleviate degenerative or traumatic neurological diseases by delivering current pulses to neural terminations to stimulate their activity. The output stage of the neural stimulator circuit must source and sink current pulses of several hundreds of uA to biological tissue featuring a series resistance in the order of tens of kΩ. The resulting output voltage swing then requires a supply voltage of the order 5 V or more [73]. Most implantable neural stimulators are supplied by an inductive link WPT, because near-field magnetic coupling experience much less energy absorption by biological tissues than radiative transmission [74], [75]. A lower loss helps also to minimize heat transfer to the tissues. In some applications, like retinal prosthesis, the alignment between the external and the internal coil is not strictly fixed, because the former is typically built into the frame of eyeglasses, while the latter is implanted together with the neural stimulation microchip and attached to the eyeball. This

causes the magnetic coupling coefficient k12 to vary significantly not only on a patient-to-patient basis, but also in any given implant during normal operation. To avoid complicated adaptive WPT schemes, the DC-DC converter must be able to handle a relatively high range of input voltages coming from the rectifier [76].

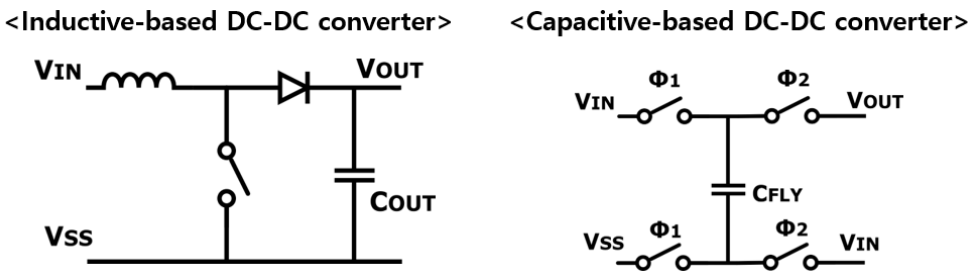

Figure 57 Inductive/Capacitive based DC-DC converter diagram (Boost converter, Voltage doubler)

Typically, in biomedical devices, a diode-based rectifier delivers an appropriate supply voltage to the stimulation current generator. Inductive or capacitive step-up converters are used to step up the voltage. To overcome the size limitations of implantable modules, an all-in-one system is suitable, and a switched capacitor converter (SCC), a type of capacitive-based step-up converter, has the advantage of high integration in the CMOS process. SCCs also have less

EM interference compared to inductance-based converters. However, SCC has the disadvantage of low efficiency because it has low regulation. To compensate for this problem, higher efficiency can be achieved by setting different conversion ratios in the reconfigurable converter system.

A reconfigurable SCC is a converter that outputs multiple voltages using clocks of different phases to the switch. The figure above shows that the desired output voltage ratio can be set by charging and discharging the capacitor with different switch combinations in the unit cell.

The typical power levels required by implantable neural stimulators ranges from a few mW to a few hundred mW [77], making converter transistor losses important, with a clear efficiency vs power-density trade off that calls for an optimization methodology for transistor sizes. These levels of power also require a large storage capacitance to reduce the supply voltage ripple, making the turn-on transient of the DC-DC converter problematic.

In order to derive realistic specifications for the converter, we considered a WPT operating at 13.56MHz for a retinal neural stimulator

capable of sinking/sourcing up to 200uA/channel from/to electrodes with up to 10kΩ series resistance, requiring a 4V voltage compliance. Considering some over design margin, the supply voltage is then set to 5V.

The overall simultaneous current should not exceed a safe limit of 3mA [78], which sets the power demand by the stimulator output stages to 15mW. Adding another 15mW for the data telemetry, auxiliary circuits and digital control unit, the DC−DC converter should be able to deliver an output power PO = 30mW at VO = 5V supply, irrespective of the input voltage variations caused by the changes of the magnetic coupling coefficient k12.

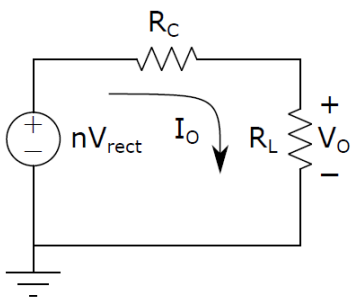

Figure 58 Equivalent model of the switched capacitor dc−dc converter considering conduction losses only.

The range of variation of the converter input voltage Vrect was

estimated prior to the design, using the first−order equivalent model of a SCC converter shown in Figure 56. The SCC converter is represented by an ideal voltage source VEQ = n·VIN, where n and VIN are the conversion ratio and input voltage, respectively, with a series resistance Rc, modeling the conduction losses of the converter switches, as shown in Figure 56. It follows from the model that the output voltage VO for a given output (load) current IO is given by:

$$V_O = n \cdot V_{IN}, - R_c \cdot I_O \qquad (1)$$

Equation (1) implies that, for a given specification of output power PO = VO·IO, output voltage regulation is achieved by modulating the output resistance Rc, whose value linearly increases with VIN. Consequently, for a fixed conversion ratio n, increasing values of VIN cause a drop of the converter efficiency η, defined as the ratio of the output power PO to the total power absorbed by the converter. The relatively wide range of VIN expected due to the uncertainty of the magnetic coupling coefficient value k12, suggests adopting a reconfigurable SCC with automatic conversion ratio selection, in order to limit the loss off efficiency.

$$V_O = n \cdot V_{IN}, - R_c \cdot I_O \qquad (2)$$

Corresponding set of threshold voltages representing the minimum value of VIN required by the SCC to deliver (VO, IO) when its conversion ratio is set to ni.

The value of the equivalent resistance Rc, as we shall see in the next section, is determined by the on resistance of the switches, so it is not known a priori. The conduction losses modeled by Rc, along with the driving losses, that is the power dissipated to drive the switches, limit the converter efficiency. Thus, setting a realistic target efficiency η between 0.6 and 0.8 (a lower efficiency is to be expected with higher conversion ratios), a reasonable estimate of Rc value can be derived and plugged into eq. (2) to compute the conversion ratio thresholds Vth,i.

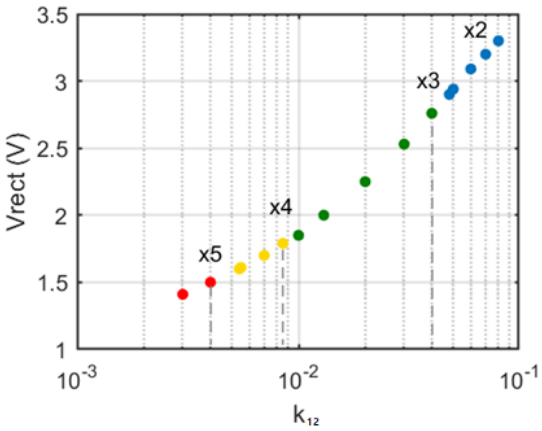

Figure 59 Input voltage range for the step-up converter

The equivalent model of the converter input port, loading the WPT rectifier, is then given by $I_{IN} = n_i \cdot I_O$, with $V_{th,i} \leq V_{IN} < V_{th,i+1}$. This model was used in the circuit-level simulations to derive an initial estimate of V_{rect} vs k_{12}, that ranges from 1.3 V to 3.3 V when k_{12} is changed between 0.02 and 0.08, and determine the corresponding conversion ratios n_i = (2, 3, 4, 5) that the reconfigurable SCC should handle to deliver the desired output voltage and current.

i) Converter architecture

Several possible topologies can be combined to realize a reconfigurable SCC. The Fibonacci (FB), series-parallel (SP), and Dickson (DK) converters [79] are examples of topologies operating on a two-phase clock. The extended binary representation (EXB) [80], signed Fibonacci representation (SFN) [81] and signed generalized representation (SGF) [82] topologies require instead a multi-phase clock.

Table 6 Figures of merit in conversion ratios n4 = 5 for different converter topologies.

	SP	FB	DK	SFN
Switches	13	10	13	10
Flying cap.	4	3	4	3
Phases	2	2	2	4
$V_{\mathrm{sw,stress}}$	$4V_{\mathrm{IN}}$	$5V_{\mathrm{IN}}$	$2V_{\mathrm{IN}}$	$3V_{\mathrm{IN}}$
$V_{\mathrm{CF,max}}$	V_{IN}	$5V_{\mathrm{IN}}$	$4V_{\mathrm{IN}}$	$3V_{\mathrm{IN}}$
$R_{\mathrm{C,FSL}}$	$26R_{\mathrm{on}}$	$54R_{\mathrm{on}}$	$26R_{\mathrm{on}}$	$67R_{\mathrm{on}}$

In order to select the topology best suited for the envisioned application scenario, we started from the most critical conversion ratio, i.e. n4 =5. It should first be noted that, while (SFN, SP, FB, DK) cover the full set required conversion ratios ni = (2, 3, 4, 5), n4 = 5 cannot be achieved with the SGF topology.

The figures of merit of the remaining four topologies for n4 = 5, are summarized in Table 6. They are the number of switches, flying capacitors CF, and clock phases; the maximum voltage stress on the switches and on the flying capacitors; the minimum value of the equivalent resistance Rc. These figures show that DK and SP topologies achieve the lowest equivalent output resistance for a given

value of the switch on-resistance, Ron. This implies that FB and SFN require larger switches to achieve the same Rc value, with a significant penalty in terms of efficiency due to the increased driving losses.

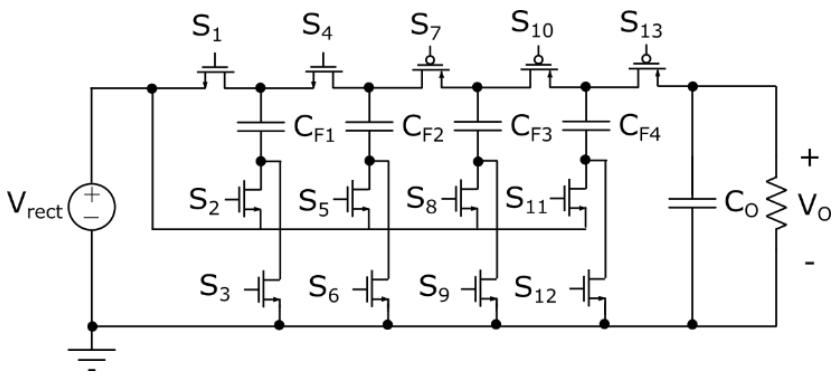

Figure 60 Simplified schematic of the reconfigurable step-up Dickson converter with programmable conversion ratios ni = (2, 3, 4, 5).

Each switch for step up converter was designed as a pass transistor as can be seen from Figure 61. Since the input voltage in the step up converter ranges from 1.2 V to 3 V the switch should pass or block the signal from the components while charging the flying capacitor. Each switch driver is composed of level shifter with buffer chains. These drivers shift the gate input voltage from Vin (which is the output of the rectifier) to Vo (output of the step-up converter).

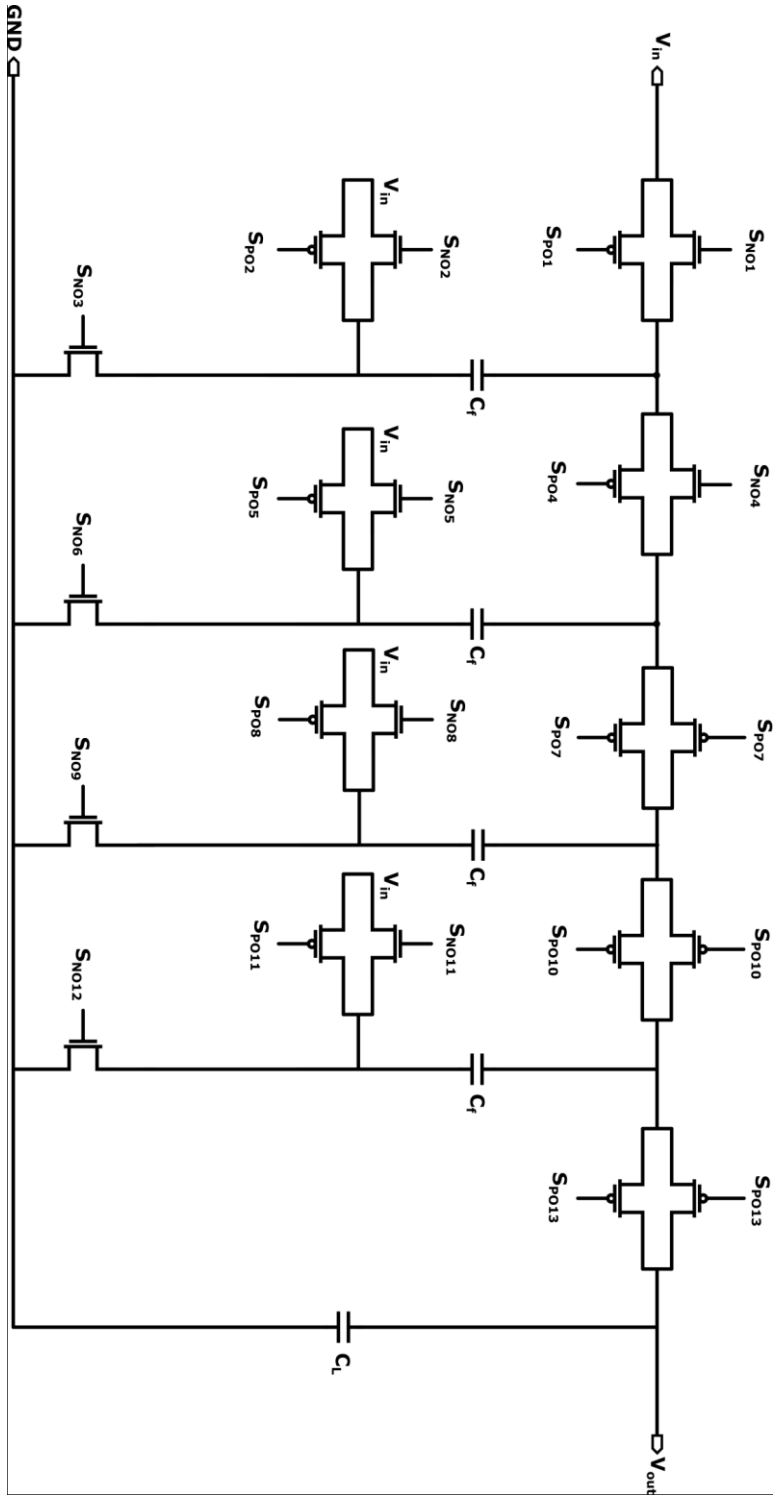

Figure 61 Full architecture of reconfigurable dickson step-up converter

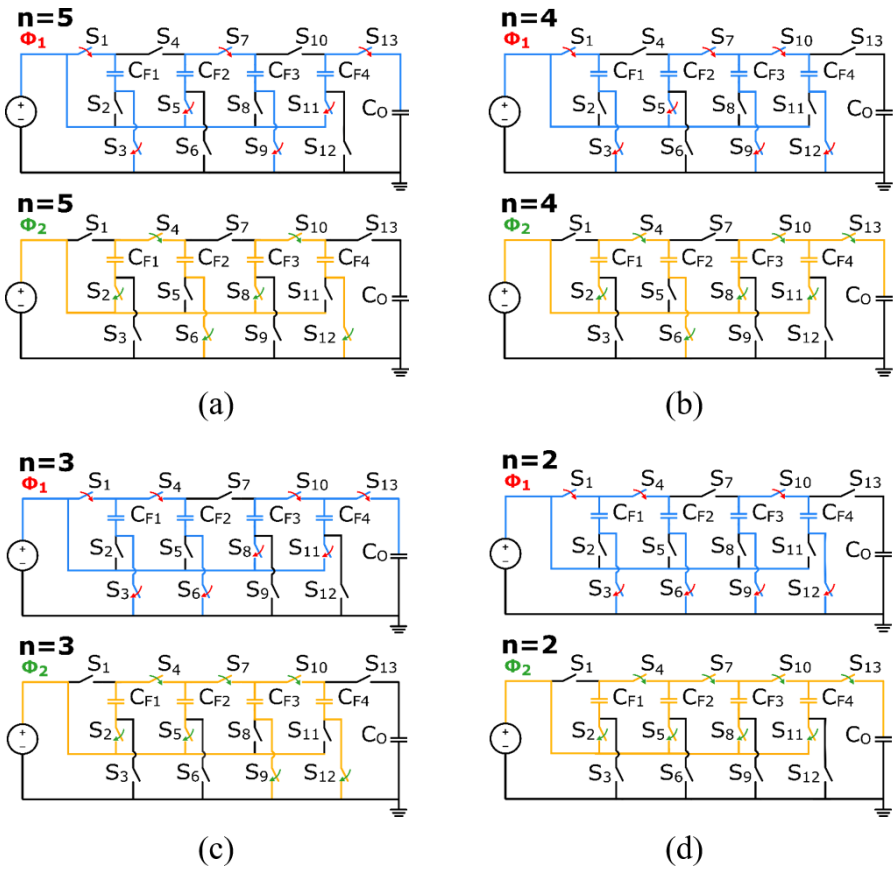

Figure 62 Modulation of the DK converter switches in the four configurations, with conversion ratio (a) n4 = 5, (b) n3 = 4, (c) n2 = 3, (d) n1 = 2.

We may then conclude that the best choice for n4 = 5 conversion ratio is the DK topology, thanks to the lower voltage stress imposed on switches with respect to SP topology. Voltage stress on flying capacitors is not an issue in this case since, given the required output power level, capacitors must be realized with external SMD. Although

the remaining three conversion ratios n1, n2 and n3 could be implemented using different topologies, we decided to stick to the DK topology because the lower conversion ratios can be realized with no extra switches, but just through a proper choice of the distribution of the two clock phases. This fact can be understood by looking at the schematic of the reconfigurable step−up Dickson converter reported in Figure 59 and at the switch modulation law reported in Table 7 and depicted in Figure 62 for each of the four possible configurations the SCC can be reconfigured into.

We then may notice that n1 = 2 is achieved by driving the gates of switches S3, S6, S9, S12 with p1, switches S2, S5, S8, S11 with p2, and switches S4, S7, S10 with both phases, so as to shunt the four flying capacitors together. Likewise, when the conversion ratio is n2 = 3, the phase distribution to the switches is chosen so that capacitors CF1 and CF2 are shunted together, and so are capacitors CF3 and CF4. When conversion ratio n3 = 4 is set, only CF3 and CF4 are shunted. Finally, n4 = 5 is achieved with the four flying capacitors, switched independently.

Table 7 Switch on−phases of the DK reconfigurable SCC.

n_i	S_1	S_2	S_3	S_4	S_5	S_6	S_7
5	Φ_1	Φ_2	Φ_1	Φ_2	Φ_1	Φ_2	Φ_1
4	Φ_1	Φ_2	Φ_1	Φ_2	Φ_1	Φ_2	Φ_1
3	Φ_1	Φ_2	Φ_1	Φ_1, Φ_2	Φ_2	Φ_1	Φ_2
2	Φ_1	Φ_2	Φ_1	Φ_1, Φ_2	Φ_2	Φ_1	Φ_1, Φ_2
n_i	S_8	S_9	S_{10}	S_{11}	S_{12}	S_{13}	
5	Φ_2	Φ_1	Φ_2	Φ_1	Φ_2	Φ_1	
4	Φ_2	Φ_1	Φ_1, Φ_2	Φ_2	Φ_1	Φ_2	
3	Φ_1	Φ_2	Φ_1, Φ_2	Φ_1	Φ_2	Φ_1	
2	Φ_2	Φ_1	Φ_1, Φ_2	Φ_2	Φ_1	Φ_2	

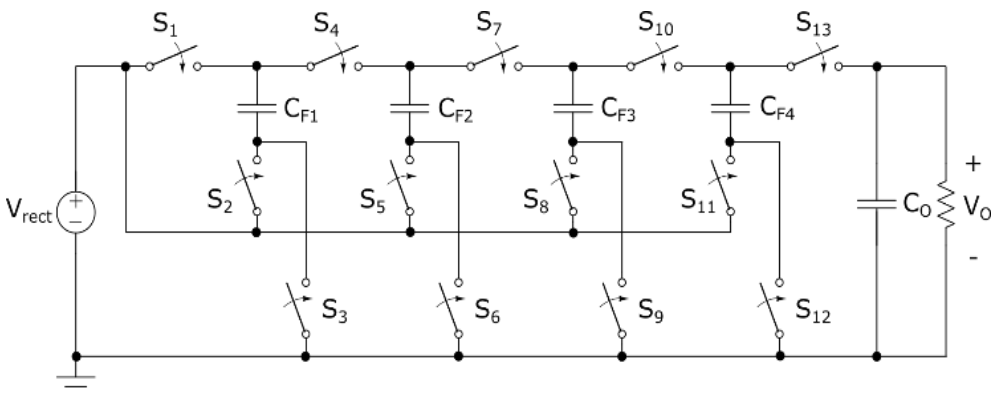

Figure 63 MOSFETs working as switches in the DK reconfigurable SCC

2.1.3.1.2 Switch Size Optimization

Having established the converter topology and the number of switches, we now present an optimization procedure to maximize the converter efficiency by taking into account the effect of the switch

width on both conduction and driving losses. We will assume that the SCC operates in the so-called fast switching limit (FSL) [83], implying that, once steady state is reached, capacitor voltage variation is very small, and thus the current flowing through each switch during the on phase is approximately constant. Operation in the FSL limit is guaranteed by a proper choice of the flying capacitor values.

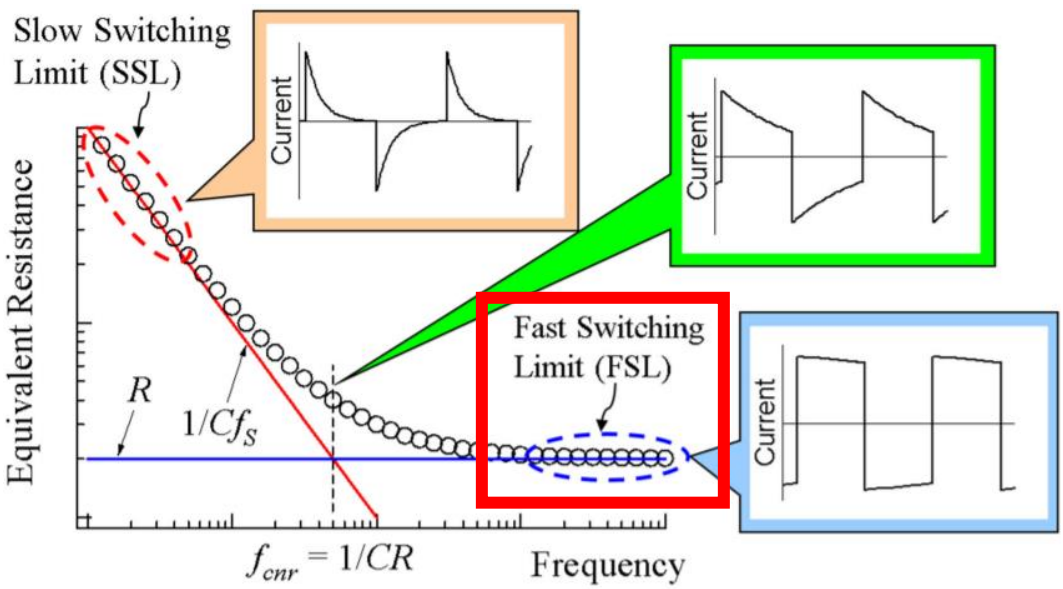

Figure 64 Fast switching limit operation for SCC

The optimal sizing is derived by minimizing a cost function that includes the power dissipated by both conduction and driving and driving losses over all the four possible configurations the SCC can

synthesize. In this way, the procedure aims at a circuit design that is globally optimized over all the operating conditions.

Conduction losses are accounted for by modeling the minimum equivalent output resistance Rc,i of SCC in the i−th conversion ratio. While, based on the analysis in [80], [81], in general Rc,i is a function of the switching frequency, the switch on−resistances and the flying capacitor value, if the converter is operated in FSL then Rc,i is determined by the switch on−resistances alone. Then, by equating the total conduction power loss, Rc,I • IO2 to the sum of the conduction power dissipated by each switch during its on phase, we get:

$$R_{c,i} = \frac{\sum_{m=1}^{M} h_{m,i}^2 R_{on,m}}{N_i} = \frac{1}{N_i G_0} \frac{\sum_{m=1}^{M} h_{m,i}}{W_m} \qquad (3)$$

Table 8 hi,m values corresponding to the four conversion ratios

n_i	S_1	S_2	S_3	S_4	S_5	S_6	S_7
5	2	2	2	2	2	2	2
4	2	2	2	2	2	2	2
3	2	1	1	1	1	1	2
2	2	0.5	0.5	1.5	0.5	0.5	0.5
n_i	S_8	S_9	S_{10}	S_{11}	S_{12}	S_{13}	
5	2	2	2	2	2	2	
4	1	1	1	1	1	2	
3	1	1	1	1	1	2	
2	0.5	0.5	1.5	0.5	0.5	2	

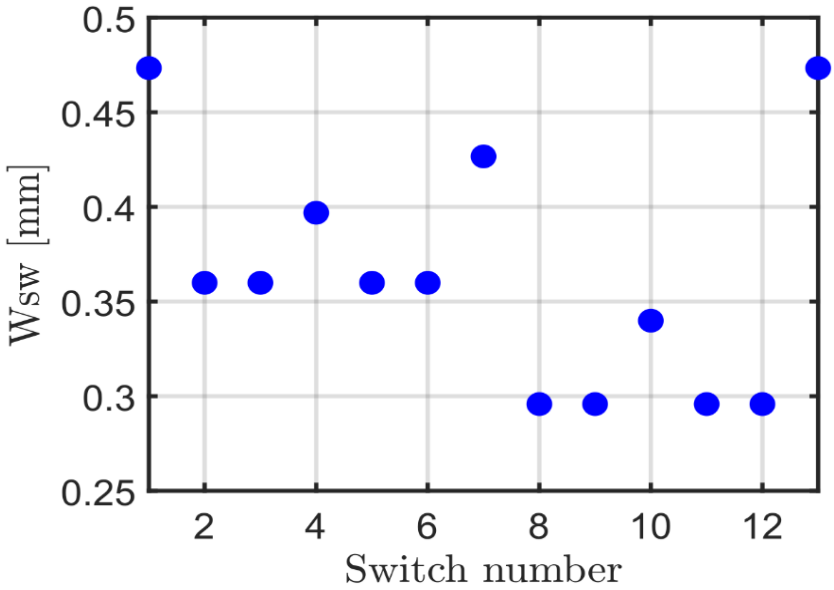

Figure 65 Switch width optimization according to switch number

where M is the number of the converter switches, Ron,m the on−resistance of the m−th switch, Ni is the number of phases used by the i−th converter configuration, and hm,i = Im,i / IO. Im,i is the constant current flowing, during the on−phase, through the m−th switch. Assuming that the gate length of the MOS transistors used to implement the switches is set to the minimum value, then Ron,m = 1/ Gm, with Gm = G0Wm, G0 being a technology parameter and Wm the width of the m−th switch. The hm,i parameters represent the fraction of the total output current IO flowing in the m−th switch and, ultimately,

determine the optimal relative sizing of the switches.

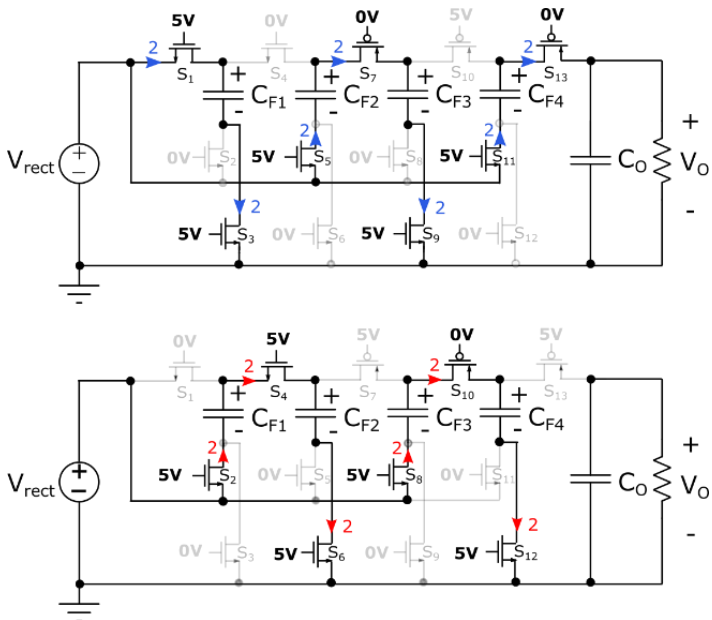

Figure 66 Circuit operation for the n1=5 conversion ratio with the related gate switch voltage to turn them on and off and the h5 parameters.

As an example, Figure 66 highlights the currents flowing through the switches in the two clock phases when the converter is in the n4 = 5 configuration, with re red and blue annotation representing the hm,i values. The hm,i parameter values corresponding to all the four conversion ratios of the SCC are reported in Table 9.

A general expression for the power dissipation in configuration i

due to the driving losses is given by:

$$P_{d,i} = \sum_{m=1}^{M} C_0 W_m f_{sw} V_{DD,m,i} \Delta V_{m,i} \tag{4}$$

where C0Wm = Cg,m is the gate capacitance of the transistor implementing the m−th switch, VDD,m,i the supply voltage from which the charge is taken, and ΔVm,i the voltage variation across Cg,m. The gate capacitance is assumed to be, at first order, proportional to the transistor width, Wm, while C0 is a technology related constant. It should be noted that, with VDD,m,i and ΔVm,i independent of m and i, a condition which is almost satisfied by the proposed DK converter , the cost function Pd of the driving losses, that sums up the driving power losses given by (4) in the I = 4 possible converter configurations, depends on the total switch width Wtot rather than of the individual switch sizing.

Based on this consideration, the optimal relative switch sizing can be derived from the partial cost function of the conduction power losses:

$$P_c = \sum_{i=1}^{I} R_{c,i} I_{o,i}^2 = \sum_{m=1}^{M} R_{on,m} \left(\sum_{i=1}^{I} \frac{h_{m,i}^2 I_{o,i}^2}{N_i} \right) = \frac{1}{G_0} \sum_{m=1}^{M} \frac{H_m^2}{W_m} \tag{5}$$

where Io,i is the maximum current in the i−th topology and

$$H_m = \sqrt{\sum_{i=1}^{I} \frac{h_{m,i}^2 I_{o,i}^2}{N_i}} \tag{6}$$

The partial cost function (5) shall then be minimized under the constraint of a fixed total switch width Wtot. Applying Lagrangian optimization of (5), under fixed Wtot constraint expressed as

$$G_{tot} = G_0 \sum_{m=1}^{M} W_m = G_0 W_{tot} \tag{7}$$

we obtain the optimal relative m−th switch size with respect to Wtot:

$$W_m = \frac{H_m}{H_{tot}} W_{tot} \tag{8}$$

where Htot is the sum of all Hm. The resulting relative size of the converter switches are reported in Table IV, taking into account that switches S1 – S10 are realized using nMOSFETs, while S11 – S13 are realized using pMOSFETs.

Table 9 Relative size of the converter switches.

	S_1	S_2	S_3	S_4	S_5	S_6	S_7
W_N/W_{tot}	8.2%	6.2%	6.2%	6.8%	6.2%	6.2%	7.4%
W_P/W_{tot}	0%	0%	0%	0%	0%	0%	0%
	S_8	S_9	S_{10}	S_{11}	S_{12}	S_{13}	
W_N/W_{tot}	5.1%	5.1%	5.9%	0%	0%	0%	
W_P/W_{tot}	0%	0%	0%	10.2%	10.2%	16.3%	

The optimal value of Wtot, and thus, the absolute switch sizes Wm,

can be obtained minimizing the total cost function, Ptot = Pc + Pd. Substituting (8) in (4) and (5), Ptot can be written as:

$$P_{tot} = \frac{\alpha}{W_{tot}} + \beta W_{tot} \tag{9}$$

where

$$\alpha = \frac{H_{tot}^2}{G_0}, \quad \beta = \sum_{i=1}^{I} \left(\frac{C_0 f_{sw}}{H_{tot}} \sum_{m=1}^{M} H_m V_{DD,m,i} \Delta V_{m,i}\right) \tag{10}$$

The value of Wtot minimizing the power losses is then:

$$W_{tot} = \sqrt{\alpha/\beta} \tag{11}$$

that corresponds to a condition where conduction losses equal the driving losses. Plugging the technology specific parameters G0 = 0.57mS/μm, C0 = 1.8fF/μm, the design specifications fsw= 13.56MHz, N = 2 together and the hm,i values listed in Table III into (10) yields Wtot = 5.8 mm.

The flying capacitors values CFk must be chosen in order to guarantee that the SCC operates in FSL. Starting from the value of Rc,i that can be computed from (3) it can be shown that CFk = 2.2 nF, k = 1, …, 4, is large enough to guarantee a negligible variation of the capacitor charge.

2.1.4 Wireless Data Transmission Circuit

2.1.4.1 General Data Transmission Schemes

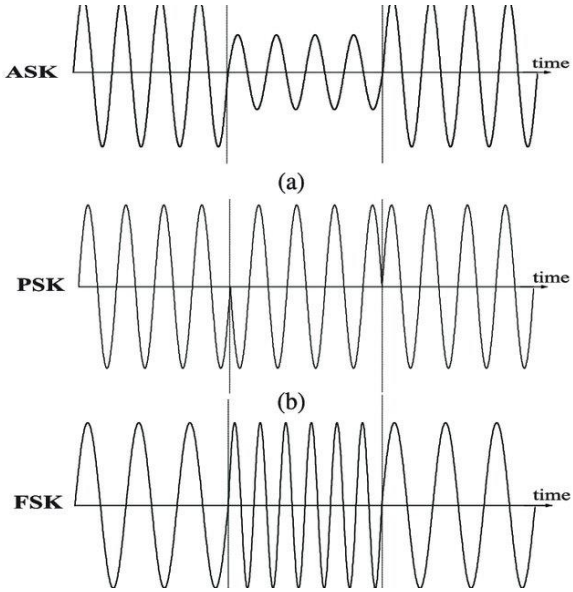

Figure 67 Amplitude shift keying, phase shift keying, frequency shift keying

Amplitude shift keying(ASK) and Frequency shift keying(FSK) are more attractive in terms of the minimal size of the implantable biomedical device among inductive coupling near-field magnetic communication, due to simple circuitry, although they experience SNR degradation and low data rates. Several artificial retinas that developed until lately also used these schemes.

Retinal prosthesis that used ASK scheme which has 15 stimulation channels achieved up to 700kbps with power consumption of 15mW for

stimulation. Though ASK scheme has simple modulator and demodulator system architecture it has low power efficiency so that it requires quite a lot of power compare to its number of electrodes [85].

Also another artificial retina that used FSK scheme achieved around 2Mbps data rate with 100mW of power loss with 98 stimulation channels. From these examples, we discovered that we need higher data rate communication to expand number of channels and electrodes of artificial retina, to achieve performance similar to human vision [85]. For example, to obtain resolution similar to the human eye, a visual prosthesis requires about 40Mbps to support 600~1000 electrodes. However, a conventional visual prosthesis can only support 60~100 electrodes. To achieve higher data rate from the data transmission system, pulse delay modulation (PDM) scheme was selected [86].

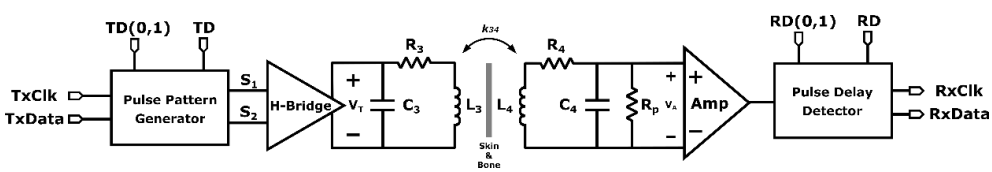

Figure 68 Data transmission system diagram

There are a pulse pattern generator and an H-bridge at the data

transmission end. The PDM data transmission design is depicted in Figure 68.

i) Pulse pattern generator

In the pulse pattern generator, at each Tp period (73.74ns), when the data bit is 1, two pulses with adjustable width and delay time are created. Two pulses are spaced apart by Tp/2 and are not generated when the data bit is 0. Therefore, when the pulse delay modulation scheme is used, the data rate (DR) always becomes 13.56Mbps, the same as the power frequency fp. The two pulses generated from data transmitter can be adjusted to a width of about 3.5 to 10 ns through a fine delay PD.

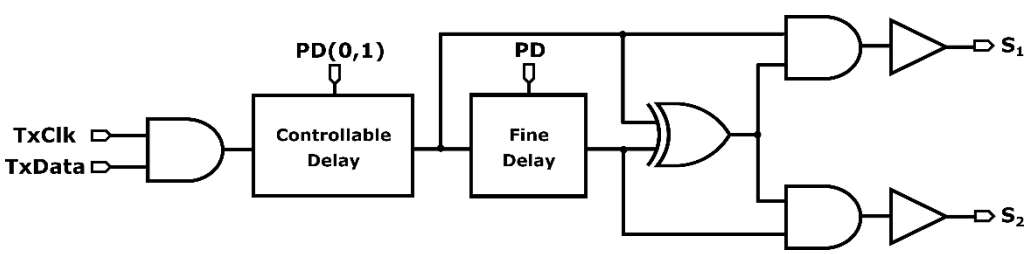

Figure 69 Pulse pattern generator diagram

By looking at the controllable delay inside the pulse pattern

generator, the system consists of a combination of coarse and fine delays that can adjust the delay time. This coarse delay can be adjusted to about 4 to 40 ns through an external bias current signal, and the fine delay can be adjusted to about 3.5 to 10 ns through an external bias current signal. The building delay line can be done using logic gates that have a propagation delay. One way to compensate for the delay times from variations in process temperature is to use feedback. While in this study, we used a combination of coarse and fine delay cells to achieve a wide range of delay.

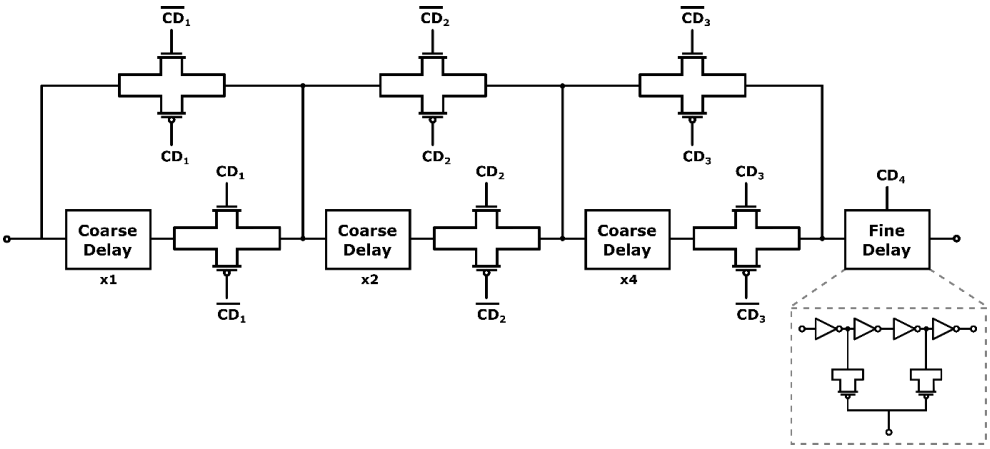

Figure 70 Controllable delay diagram

By looking inside the coarse delay cell, the corresponding delay cell is composed of two starved delay inverter cells. The corresponding SIDCs are composed of bias fingers P 17 and N 17, and each SIDC

finger is composed of P 4 1 and N 4 1.

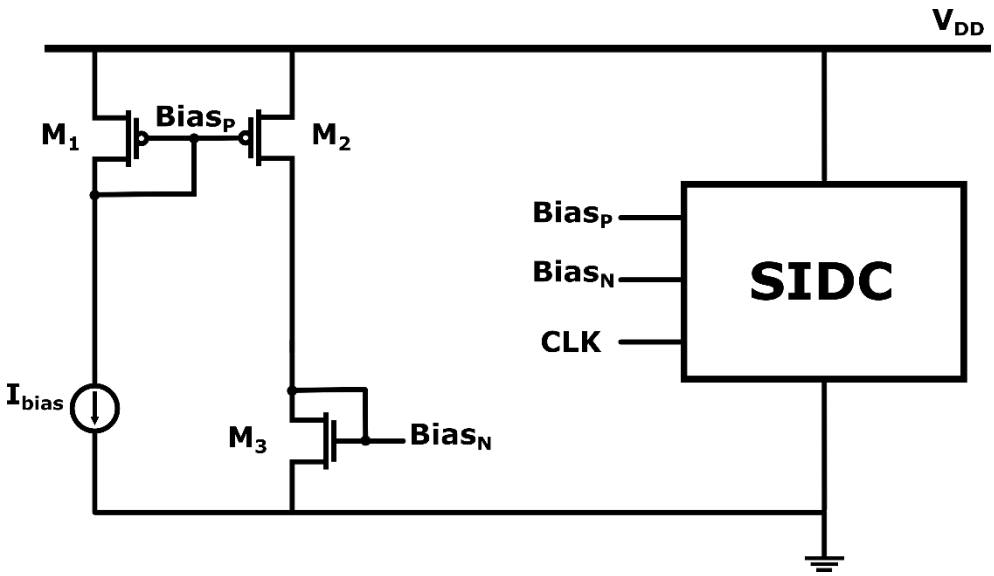

Figure 71 Basic structure of coarse and fine delay cell

The current starved inverter delay shows good performance with a longer delay time and static power consumption. In this way, the delay circuit with starved inverters connected linearizes the delay element by about 23.5% more than the existing conventional delay circuit. The currents of those MOSFETs connected to each stage of the delay cell are defined by control voltage $Bias_P$ and $Bias_N$. At the same time, the other MOSFETs connected through $Bias_P$ and $Bias_N$ are working as the current sink and source, respectively. The bias current coming from

the input of the starved inverter delay cell is used to provide correct polarization of the first delay stage. The currents are mirrored in each inverter delay system source or sink stage. By adjusting the ratio of W/L of delay cells, it is possible to obtain a larger amount of delay regulation. When the current starved inverter delay element decreases, the range of a delay regulation decreases, while the linearity can be improved [87].

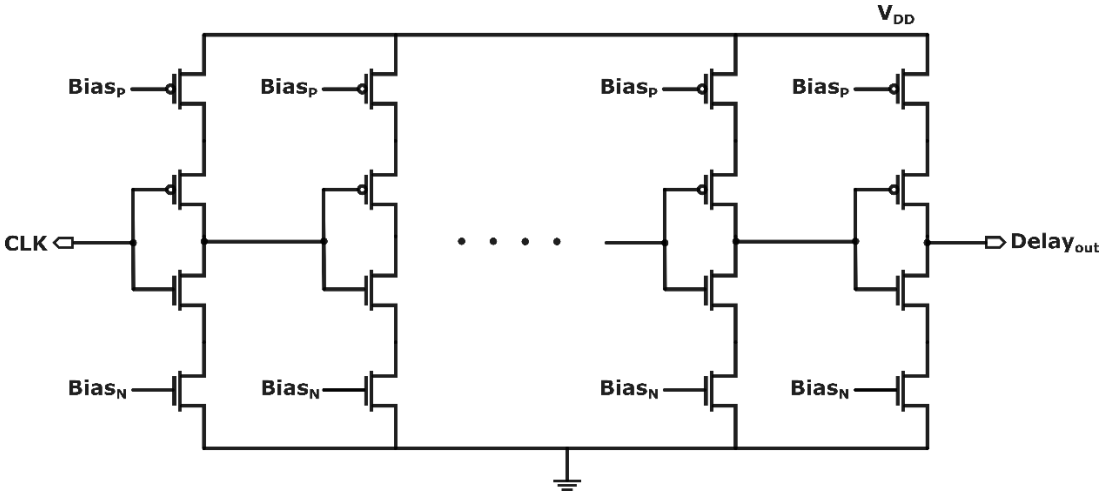

Figure 72 Starved inverter delay cell diagram

The coarse and fine delays were adjusted by changing the bias current of the SIDC after connecting several SIDCs in series. The coarse delay has two SIDCs connected in series, and the fine delay is

controlled by one.

ii) H−bridge

A H−bridge is required to reverse the poles of the two narrow pulse pattern signals generated by the data transmission circuit. The basic configuration is shown in Figure 73, and it is called this because it is H−shaped [88]. MOSFETs are used as switches and are turned on in diagonal pairs. The peak of the two pulses generated from the pulse pattern generator doubles the Vdd to 2Vdd so that the first pulse operates at +2Vdd and the subsequent pulse at −2Vdd. MOSFET P1 = N2 = on when a forward voltage is applied, N1 = P2 = off when a reverse voltage is applied. When S1 = S2 = 0, N1 and N2 are turned off, P1 and P2 are turned on, and the L3 node is connected to Vdd. If S1 = S2 = 1, conversely, P1 and P2 are turned off, N1 and N2 are turned on, and the L3 node is connected to the ground. When S1 = 1 and S2 = 0, N1 and P2 are turned on, and N2 and P1 are turned off, causing current to flow in L3 in the left direction.

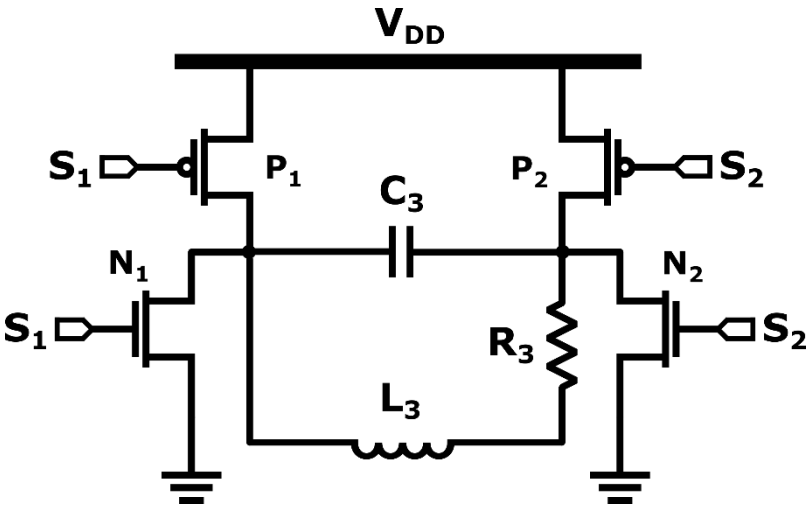

Figure 73 H−bridge diagram

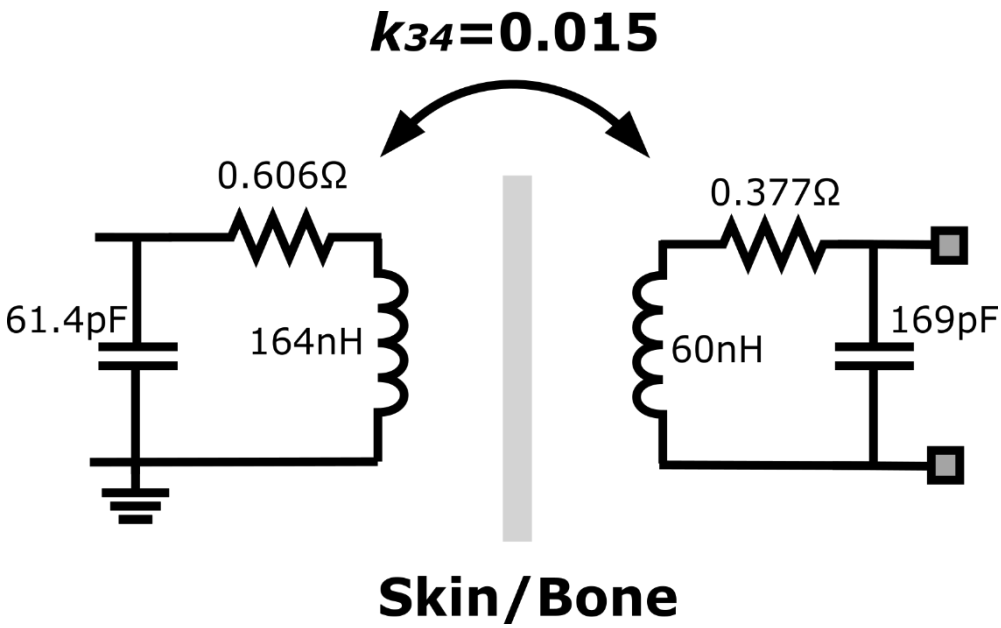

Figure 74 Data tank parameters

The parameters of the data tank were also set considering the

limited implantable space for the artificial retina. According to the size limitation of the implantation and optimal tuning method, the values of inductance, capacitance and resistance for data tank were selected.

Table 10 Data tank parameters under implantation conditions

	1st Coil part	2nd Coil part
Maximum outer D (mm)	13	10
Quality factor	85	50
Line width (mm)	0.45	0.45
Spacing (mm)	0.2	0.2
Number of turns	8	4
Inner D (mm)	3	4.55
L (nH)	164	60
C (pF)	61.4	169
R (Ohm)	0.606	0.377

The inductive link specifications for data transmission can be seen in Table 10.

In retinal prosthesis, normally 1~2Mbps of data need to be

delivered to stimulate electrodes simultaneously. Traditionally in biomedical system, a single pair of coils with single carrier frequency to deliver power and data wirelessly used. The technology of using a single carrier for both power and data transmission has two significant drawbacks. The first is that the carrier's frequency limits the data rate. The data rate should not exceed a few kbps for systems using power carrier frequencies below 50 kHz. The second disadvantage is that the frequency shift keying (FSK) and load shift keying (LSK) technique used for forward communication deviates from the optimal point and reduces the power transmission efficiency, so the FSK/LSK technique is unsuitable for application to a high-power WPT system []. However, a higher data rate can't be achieved by using the single paired system. Increasing the data rate is to increase the bandwidth, which means increasing the carrier frequency. However, by doing this, power transmission efficiency might decrease because of power dissipation from tissue absorption.

To overcome these drawbacks, several methods have been proposed to use multiple inductive links with multiple carriers to increase the data rate and maintain power transfer efficiency [90]. In

this method, power and data are transmitted over independent physical channels, where power carriers are carried over one inductive link, and data carriers are transmitted over another link. This system decouples data transmission from power delivery by assigning a low frequency (fp) to power and (usually) a high frequency (fd) to data carriers. Separating power and data allows using a low Q system and high carrier frequency for data transmission and a high Q and low carrier frequency for power transmission. As a result, higher data bandwidths can be achieved without compromising power transfer. However, multiple links introduce additional self-interference between the two channels. In addition, a strong power carrier is considered to large noise for small data signals, reducing the signal-to-noise ratio (SNR) in the communication channel. Multiple inductive links also lead to larger device sizes, which is undesirable for limited-space applications. While compared to the single-pair coil, the double-pair coil's wireless communication can achieve a higher data rate; we selected this scheme for our design. The designed data coils specifications can be found in Table 11.

Table 11 Designed data coils specifications

Unit: mm	L2	L4
Substrate height (H)	0.1	0.1
Winding trace width (W)	0.45	0.45
Winding trace thickness (T)	0.01	0.01
Inter-winding gap (S)	0.2	0.2
Outer inductor diameter (Do)	13	10
Number of turn (N)	8	4.5
Test frequency (f)	50MHz	50MHz
Inner inductor diameter (Di)	3	4.55
Inductance	163.07nH	62.84nH

2.1.4.2 Pulse Delay Modulation (PDM)

The data receiver has a pulse delay detector, an amplifier, and a controllable delay stage. A carrier-less modulation technique called PDM (Pulse Delay Modulation) was used to recover the received data signals. This method saves the power and space required to filter power carrier interference and further reduces implantable medical devices' power consumption by exploiting the low-power and low-complexity characteristics of impulse radio ultra-wide-band on the Tx side.

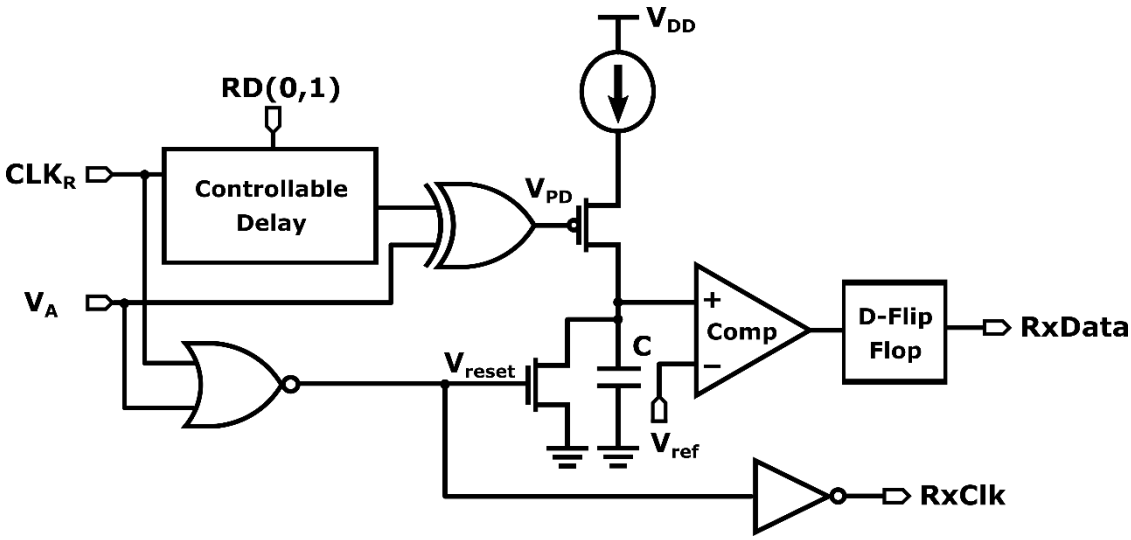

Figure 75 Pulse delay detector

The delay is first detected in the pulse delay detector by comparing the squared V_A with the amplifier and the recovered CLK_R in XOR. This is specified as V_{PD}. During one cycle of T_P, the integrator charges the capacitor. Here C_{INT} is 70fF, and I is 4uA. Next, integrator output VINT is compared with externally adjustable Vref to detect data bit 1. When VINT¬ is greater than Vref, data bit '1' is detected. Otherwise, it is detected as '0'. Next, V_A and CLK_R pass through a NOR gate to create a reset signal, V_{RST}. This reset signal serves to discharge capacitor C_{INT} and prepare the integrator to receive the next bit of data. To restore the pulses at the comparator output, the D flip flop is synchronized with

the rising edge of the clock. Therefore, Rx-data is ready to become a sample at the rising edge of Rx-CLK [91].

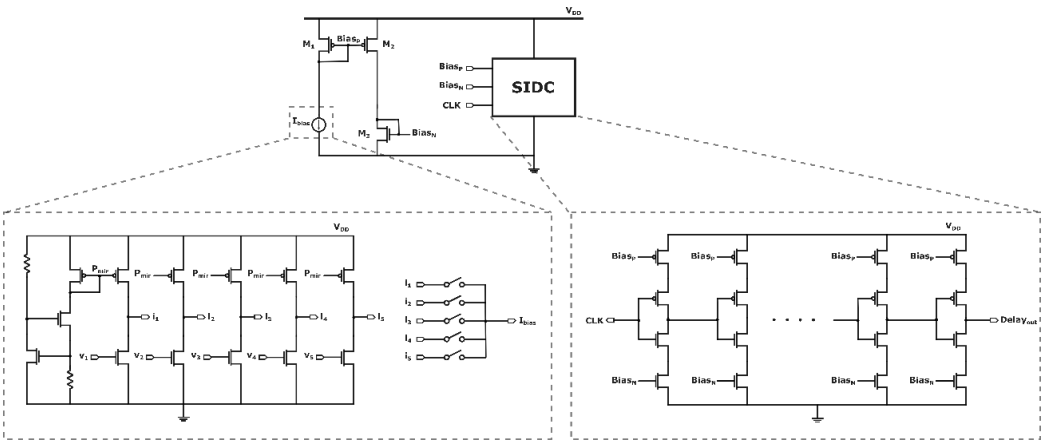

Figure 76 Controllable delay receiver diagram

The controllable delay at the data receiver has the same configuration as the transmitter's, but the bias current can be changed by 0.5uA while controlling the switch MOSFET with a voltage signal. Through this, the delay of SIDC can be adjusted.

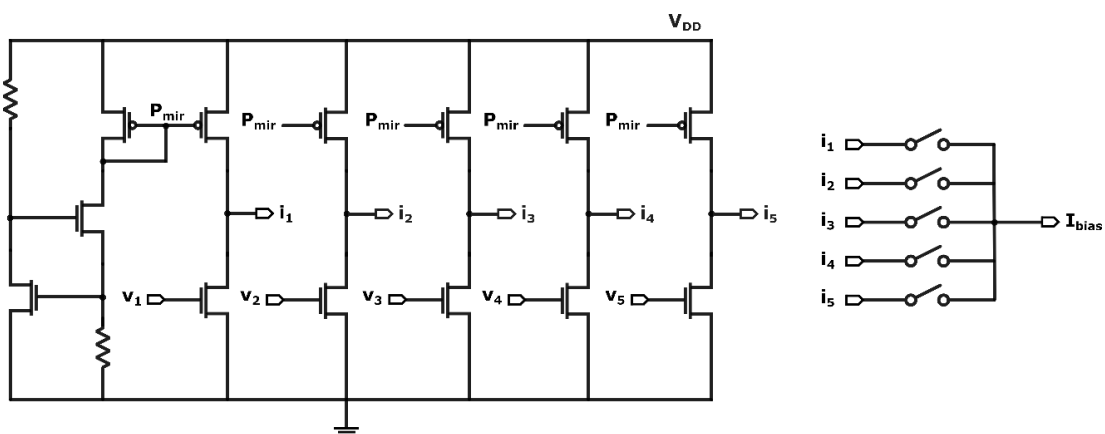

Figure 77 Bias current for SIDC

The total bias current for SIDC is controlled using switches. By adding current 0.5uA, the delay in SIDC controlled from 7 ~ 85ns to compensate process variation.

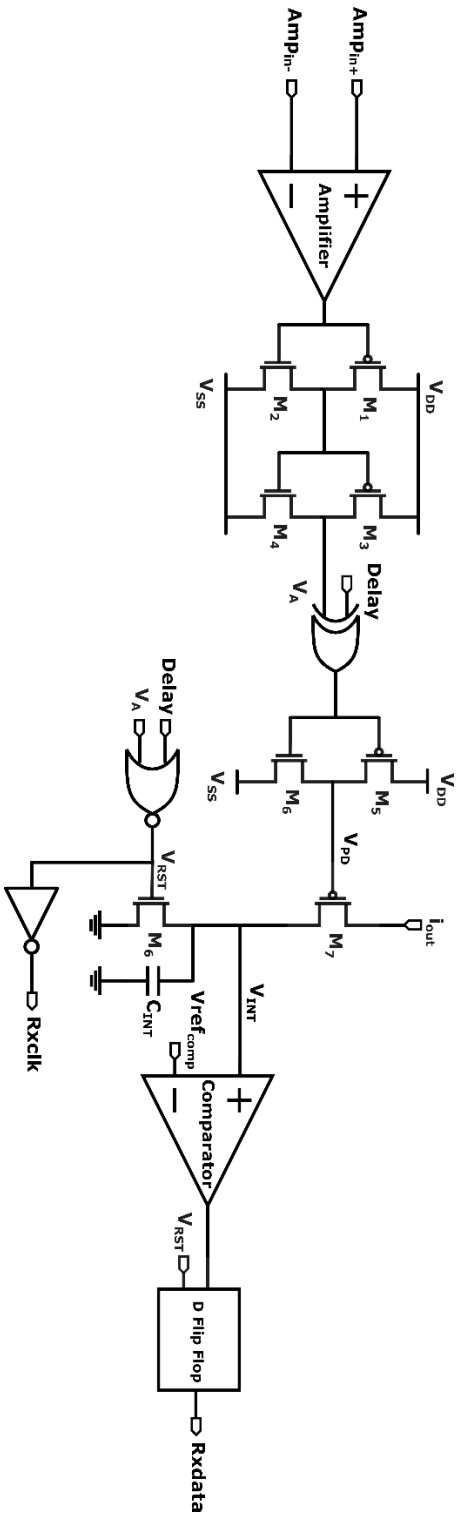

Figure 78 Data recovery system

The data recovery system is shown in Figure 78. The high gain amplifier amplifies received signals, which is the combination of power interference signal with data ringing signal to square those. The pulse delay detector detects the delay between V_A and recovered clock signal. The amplifier used in data receiver has 22.2dB of gain at fd = 50MHz. While the comparator with 32.8dB at same fd.

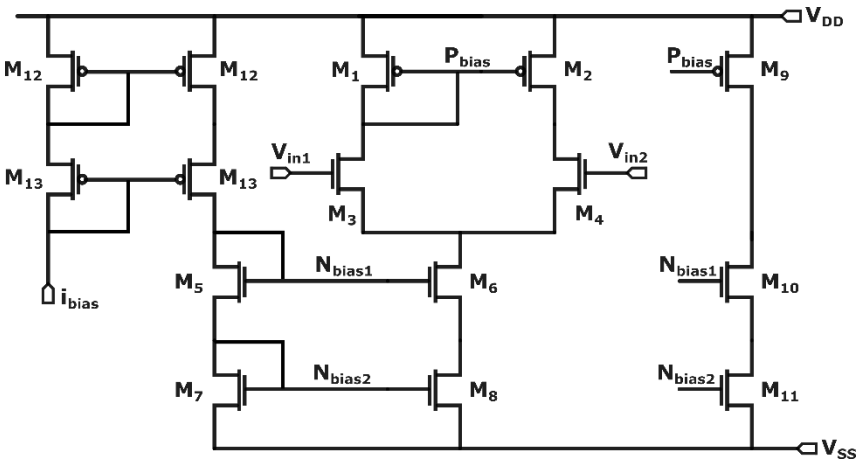

Figure 79 Amplifier 1.8V

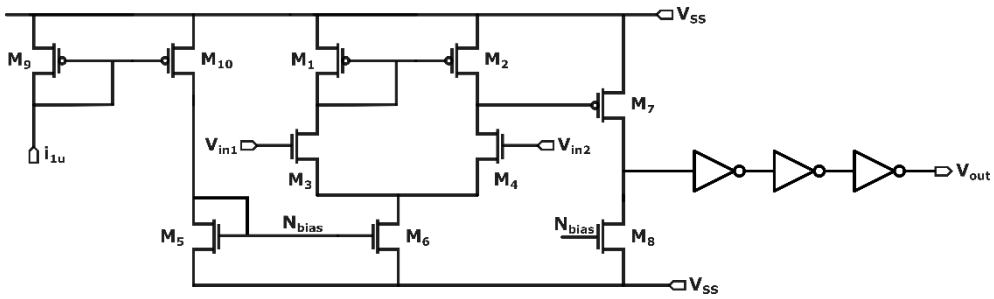

Figure 80 Comparator 1.8V

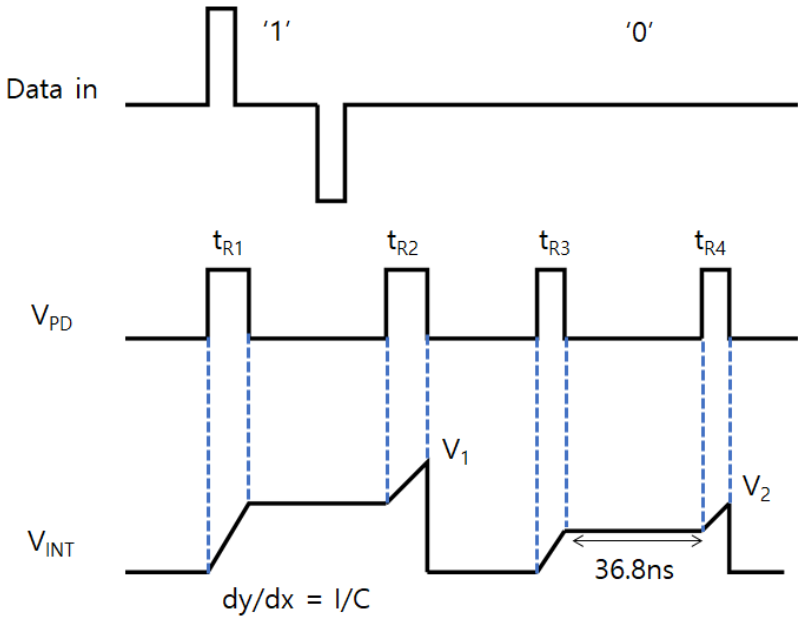

Figure 81 Operation signal V_{PD} and V_{INT} to charge and discharge C_{INT} when the data signal is bit '1' and '0', respectively

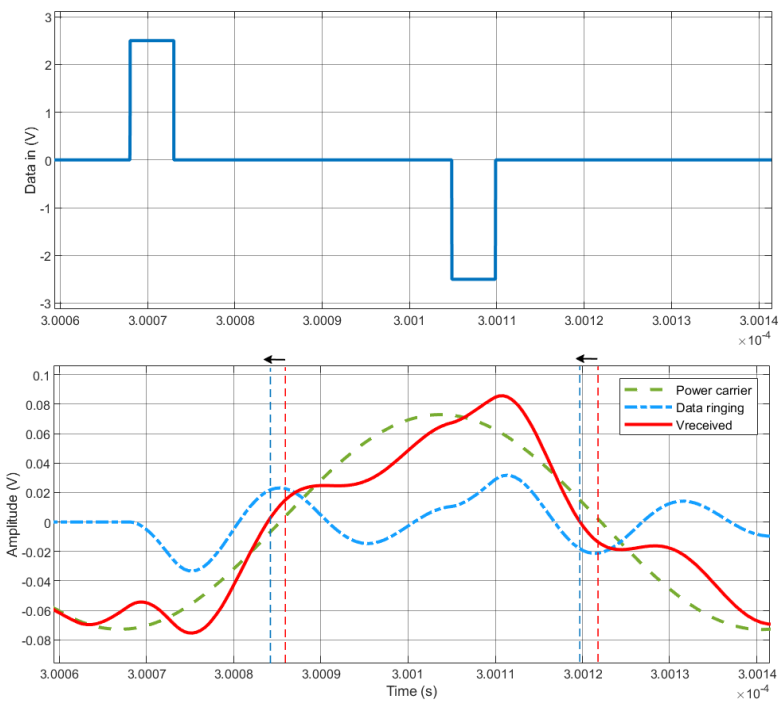

Figure 82 PDM waveforms simulated in MATLAB

When the simulation was performed with MATLAB, the light green line, which is the power carrier interference signal caused by k14, met the data ringing signal indicated by the blue line generated when the pulses with two opposite polarities generated by the pulse pattern generator of the data transmitter were transmitted to the data receiver. It can be seen that the Vreceived signal of the red line finally seen has shifted to the point where zero crossing occurs to the left rather than the existing power carrier interference. The shift can be adjusted, but it is about 2.4 ns. The width of the two pulses was about five ns, and the power carrier transmitted from the L1C1 tank was a sinusoid with a phase shift of 90 degrees at 13.56 MHz with a peak-to-peak value of 100 Vpp. The two pulses have an amplitude of 2.5V, and a slight delay adjustment was made through the controllable delay. Through this, the peak of data ringing was aligned with the zero crossing of power carrier interference. Therefore, the signal passing through the L4C4 tank is quickly damped within about 35 ns and 70 ns at fd = 50 MHz, and it can be seen that the damping is completed before the next pulse starts.

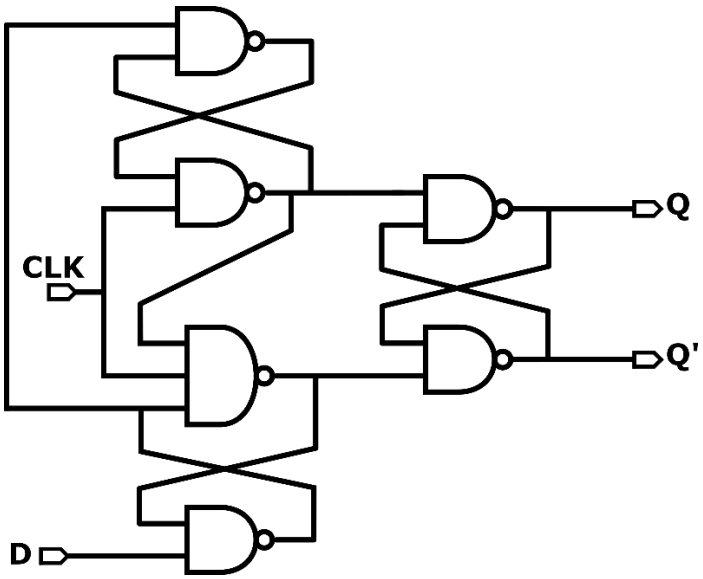

Figure 83 D Flip Flop

A D flip−flop or data flip−flop is a type of flip−flop with only one clock pulse input with one data input, 'D,' and two outputs Q and Q bars. This flip−flop is called a delay flip−flop because when input data is provided to the d flip−flop, the output follows the input data delay by one clock pulse. After comparing V_{INT} with externally controllable reference voltage, the recovered data signal is ready to be sampled at the rising edge of the recovered clock signal with D−flip flop [92].

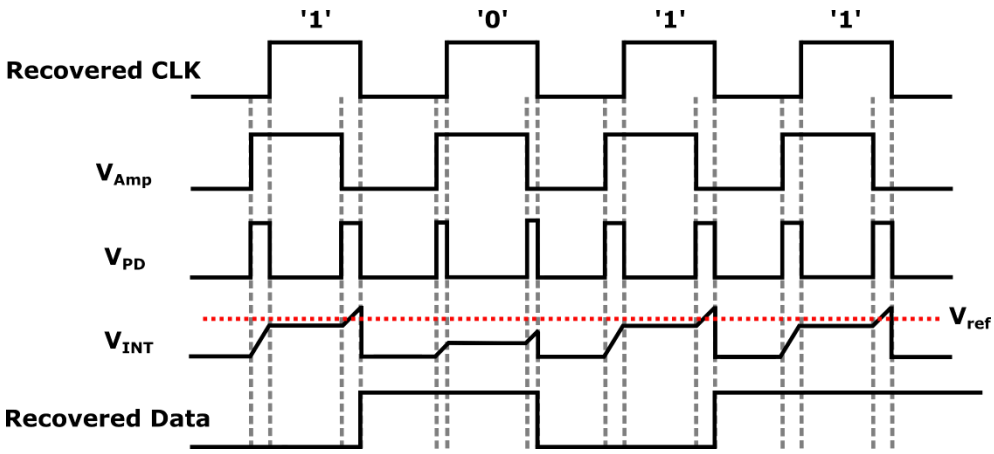

Figure 84 Operating waveforms for data recovery mechanism

PDM is reasonably robust to changes because this scheme keeps td relatively constant, taking into account the fact that L1 and L3 move together. Also, a small change in t_d slightly shifts the voltage peak of the data ringing in Figure 88. This will reduce the zero-crossing shift of the signal received from the L4C4 tank. The shift of the zero crossing is equivalent to the data ringing of amplitude $\cos(\omega_d \Delta t_d)$ times smaller if td varies by Δt_d. This equates to a ~3dB reduction in SIR if Δt_d=1/8fd=2.5ns which can be conclude that the PDM scheme is relatively robust to coupling variations. In addition, to reduce the sensitivity of zero crossing shift to t_d variation, tuning frequency for the data tank was chose as 50MHz.

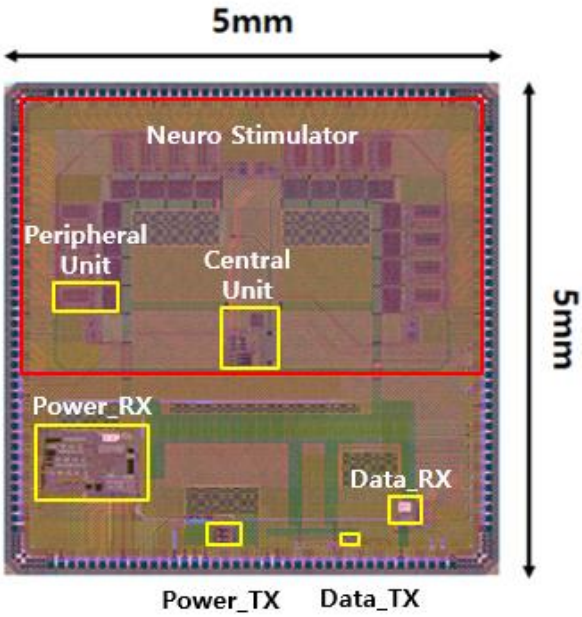

Figure 85 Designed power and data transceiver ASIC with 5x5mm^2 die area, with TSMC 0.18um standard CMOS process

The designed chip is 5x5mm^2 and designed as an integrated circuit for the artificial retina. Because the neural stimulator's channels extend the entire chip area, it could be integrated within a 3x3mm^2 area if only key parts of the circuit design were integrated. The entire system has two pairs of external coils for wireless power and data transmission; the wireless power transmission system is tuned to the industrial-scientific-medical band 13.56MHz, while the data system is tuned to 50MHz. The data rate that can be obtained is 13.56Mbps, which is the

same as the power carrier frequency, and it can be confirmed that it can be integrated within about 1mm^2 by checking only the wireless transmission and receiving system dedicated area. About 40Mbps is required to support 600 to 1000 electrodes to achieve a resolution similar to that of the human eye. However, previously researched artificial retinas can operate up to 60 to 100 electrodes normally [93].

Table 12 Designed wireless transceiver specifications

Technology (TSMC)	0.18um CMOS	
Power carrier frequency	13.56 MHz	
Data supply voltage	1.8V	
Power output voltage	5V	
Data rate	13.56 Mbps	
Area on chip	Tx	0.72mm^2
	Rx	0.13mm^2

2.2 PFA-based Electrode Fabrication

The perfluoro-alkoxy alkane film-based planar electrode with 20-channel was designed for this study. As shown in Figure 86, the

electrode stimulation site was 200um in diameter with a vertical pitch of 700um and a horizontal pitch of 1000um. The metal line width of the electrode was 50um, and the pads were designed to be compatible with standard FFC (flexible flat cable) adapters with 0.5mm pitch. Each pad had 400um of width with 500um pitch with other nearing pads.

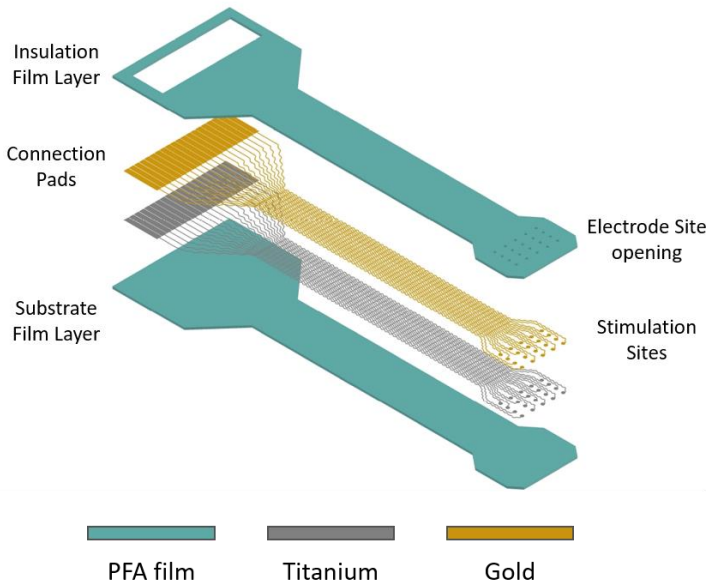

Figure 86 Planar PFA electrode components

2.2.1 Film Preparation

Among the fluoropolymers, PFA was chosen for the base material of electrode with hermetic sealing thanks to its high chemical, physical durability, and biocompatibility. Figure 87 shows the fabrication processes steps for the advanced PFA-based electrodes

for neural prosthetic devices. Ahead of the fabrication, a 50um-thick PFA film was sonicated with alcohol to remove residual particles on the film surface. Then, by sandwiching the PFA film between two polytetrafluoroethylene (PTFE, Alphaflon, Korea) films and an aluminum jig to perform a pre-thermal press to eliminate fine scratches and wrinkles on the surface of the PFA film. The film preparing temperature was set around 295℃ which is slightly above the melting temperature of PFA.

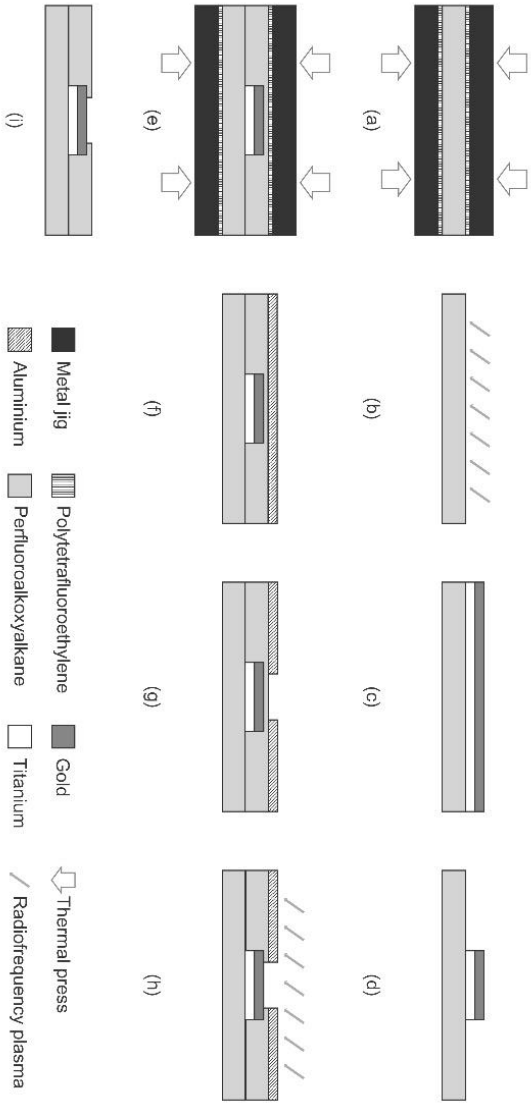

Figure 87 Fabrication process diagram of PFA film based electrode. (a) Pre-thermal press of PFA film (b) RF plasma surface pre-treatment (c) Metal deposition on pre-treated PFA film surface (d) Metal patterning and etching (e) Thermal lamination to bond patterned layer and cover layer (f) Sacrificial metal layer deposition (g) Sacrificial metal patterning for opening (h) RF plasma etching process (i) Etching sacrificial metal layer.

2.2.2 Plasma Pretreatment

i) Surface characterization of PFA film with RF plasma pre-treatment

The Radio Frequency (RF) Argon (Ar) plasma pre-treatment to strengthen the bonding between the PFA film and the metal layer was carried out for 4 min with 100mTorr base pressure and 40W power, which are optimal conditions. This condition was confirmed through a T-peel and tape test in our previous study. The equipment used for pre-treatment was RIE etcher (RIE 80 plus, Oxford Instrument, Abingdon, UK).

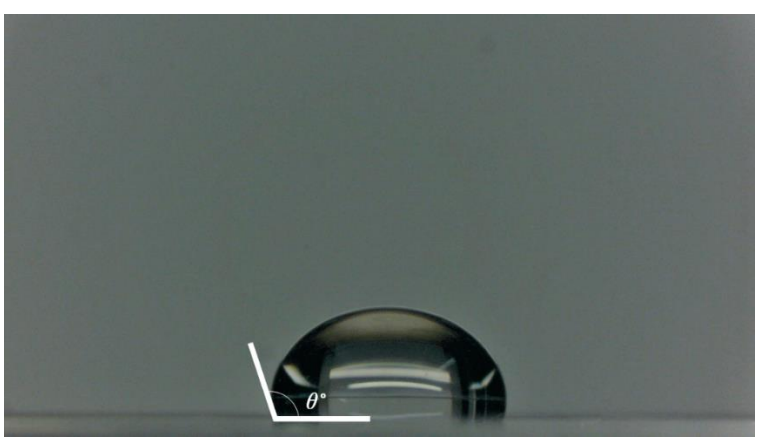

Figure 88 Water contact angle measurement for PFA film surface

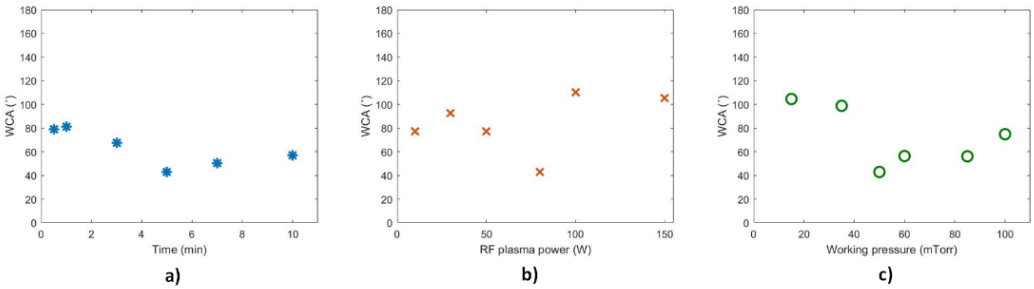

Figure 89 Effect of RF plasma treatment on PFA surface morphology (a) Water contact angle (WCA) change depending on RF plasma treatment working pressure (b) WCA change depending on RF plasma power (c) WCA change depending on RF plasma treatment time

When RF plasma pretreatment using argon gas was performed, as can be seen from the previous reports [94], free radicals were created by breaking the carbon and fluorine bonds on the surface of the fluoropolymer. These free radicals react to each other to form tangled structures like branches. Due to this structure, it was possible to increase the surface bonding strength of the fluoropolymer with surface plasma treatment. As a result, the bonding strength between the deposited metal layer and the fluoropolymer substrate increases through argon plasma pretreatment. Also from Figure 88, the adhesion strength after the thermal lamination between the fluoropolymers also

increases.

To show the variation of surface morphology, water contact angle (WCA) measurements, sheet resistance measurements, t-peel tests and atomic force microscope (AFM) scanning within various conditions were proceeded. The change of WCAs depending on the conditions of plasma pretreatment was shown in the Figure 89. As shown in Figure 87 a), the Ar RF plasma treatment time did not show dramatic change around 1 minute or less, but when it was increased to 3 min or more, water contact angle (WCA) was significantly reduced. However, it was observed that the WCA increased again as the processing time increased beyond 5 min due to the excessive plasma pre-treatment. Thus the treatment around 4 min was considered to be optimal. When it comes to the working pressure and plasma power, the WCA showed similar tendency to that of the WCA change over plasma treatment time, as shown in Figure 89 b) and c). Particularly in low RF power, free radical generation leads to over-etching, increasing the adhesive strength. However, as the RF power increases further, the adhesion strength decreases as etching becomes dominant over radical generation. [95] As can be seen from the Figure 89 b), the WCA was

the smallest when the plasma power was around 80 W.

Figure 89 c) shows that WCA was mainly independent of the working pressure below 30 mTorr, decreases between 35−50 mTorr, and becomes relatively constant above 60 mTorr. The drop−off of WCA may occur due to a decrease in the mean free path of the plasma at higher operating pressures which causes a reduction of the kinetic energy of the plasma gas [96].

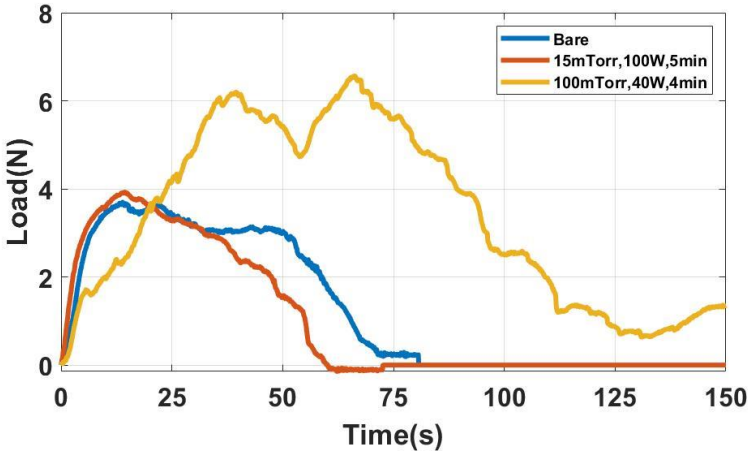

Figure 90 PFA film adhesion evaluation after thermal lamination. Bare, 15mTorr / 100W / 5min / 60sccm, 100mTorr / 40W / 4min / 60sccm condition film samples were compared

After the packaging of the cover layer using thermal pressing, the t−peel test proceeded to check out the adhesion between the substrate film and cover layer. When comparing the t−peel test results in Figure

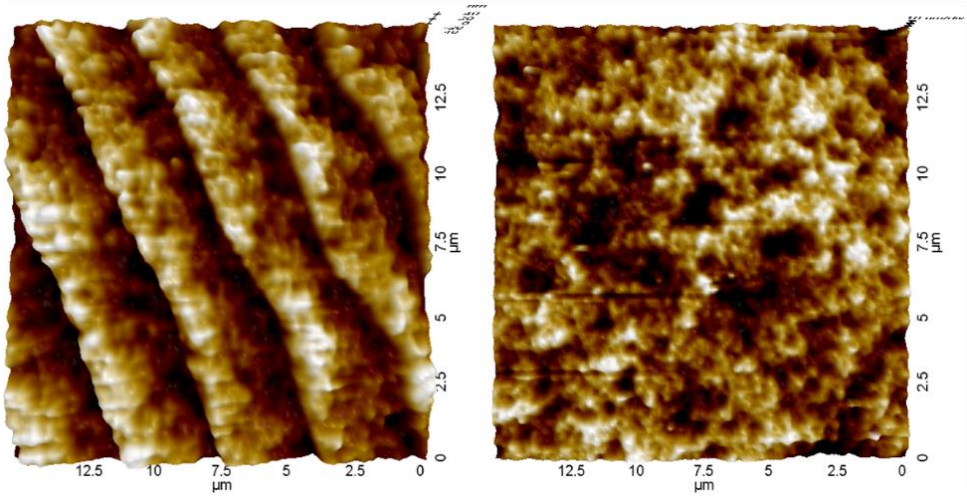

Figure 91 Atomic force microscope image for plasma surface pretreatment of PFA film. PFA film treated at 15mTorr / 10min / 40W (left), 100mTorr / 4min / 40W (right)

90, adhesion was the highest when the pretreatment time was set to about 4min.

Finally, to investigate the reasons for the optimal pretreatment conditions, the surface of the plasma pretreated PFA film was scanned using an atomic force microscope (XE-150, Park Systems Corp., Korea), which can be shown in Figure 91 of left side. For the scanning, a 0.5 Hz scan rate and contact type cantilever were used. Scanning proceeded for 15um square area for each pretreatment condition. The results of plasma surface treatment are shown in Figure 91 of right

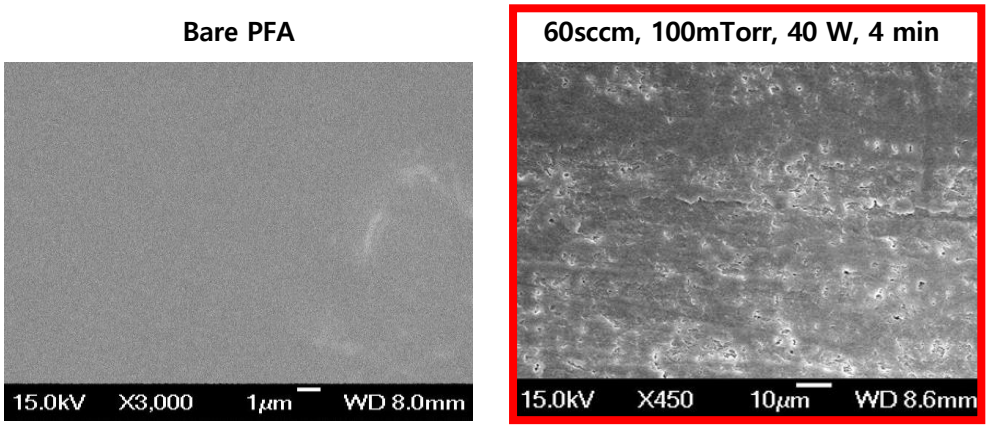

Figure 92 PFA film surface after the pretreatment of RF Ar Plasma at condition of Ar gas concentration: 60sccm, working pressure: 100mTorr, RF power: 40 W, processing time: 4 min

side. The treatment conditions for the left figure were 15 mTorr base pressure, 10 min treatment time, and 40 W power. The conditions for the right one was 100 mTorr base pressure, 4 min time, and 40 W power. The pleated wrinkle-like pattern got denser with optimal pretreatment conditions than the flat and lubricious bare film surface. The results confirm the reduced kinetic energy of plasma gas at higher operating pressures. The adhesion strength dependence on RF power indicates that ion beam irradiation or ion beam auxiliary RF plasma technology may be expected to generate more radicals in deeper

regions due to inherently higher kinetic energy. This led the adhesion strength between pretreated substrate PFA film and the metal layer or cover PFA film gets higher.

Therefore, with a proper selection of treatment conditions, the surface properties of the PFA film are converted to hydrophilic. However, in other areas, hydrophobic properties are maintained similar to the those of bare film. Hence, Ar gas plasma treatment with optimal conditions, which are 100 mTorr base pressure, 40 W power, 4 min treatment time, and 60 sccm gas flow rate was performed to increase the adhesion of the PFA substrate.

2.2.3 Metal Deposition

In the previous study[Reference], gold was deposited without an additional adhesive metal layer after Ar plasma pre-treatment, but this method caused the separation between the film and the metal layer when the electrode was immersed in the buffer solution. Titanium was used as an adhesive layer to increase adhesion between gold and PFA film after pre-treatment to compensate for this. Biocompatible ultraviolet-curing adhesive (UV630, Permabond, UK) was spin-coated on a 4-inch dummy wafer using spin coater (ACE-200, DongAh Trade Corp, Korea) to attach PFA film substrate. 50 um-thick of PFA film was loaded on an adhesive spin-coated wafer,

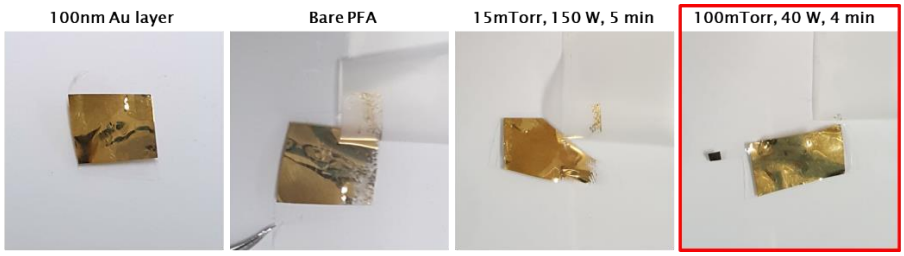

Figure 93 Tape test of pretreated PFA film with 100nm gold layer deposited without extra adhesion layer (a) Bare film without pretreatment (b) Condition of 15mTorr, 100 W, 5 min (c) Condition of 100mTorr, 40 W, 4 min

then cured with UV light for 3 min. PFA film substrate was tightly sealed using Kapton tape and placed in the e-gun evaporator to deposit 1000Å of titanium and 3000Å gold layers (ZZS550-2/D, Maestech, Korea). The corresponding gold layer can be used as a seed layer to adjust the impedance of the electrode.

RF Ar plasma surface pretreatment was performed under different experimental conditions, then a tape test was conducted after 100 nm of gold layer was deposited. The bonding force between the scotch tape and the glass plate used to conduct the tape test is about 0.9 N/cm [97]. At the experimental condition: concentration of 60sccm, 100mTorr pressure and 40 W power for 4 minutes, the adhesion strength between the deposited gold layer and the film was the strongest without any other adhesion metal layer as depicted in Figure 93.

After metal deposition, the sheet resistances in various

treatment conditions were measured. To clarify ideal treatment conditions, 10 metal deposited PFA films with 300 nm-thick gold layer on the 100 nm-thick titanium layer were prepared. Ar gas flow rate was fixed at 60 sccm while varying time, power, and base pressure. Time was varied from 0.5min, 5min, and 10min while fixing other conditions at 40 W power and 50 mTorr base pressure. Power differed in 10 W, 40 W, 80 W and 150 W for 5 min and 50 mTorr. Lastly, pressure changed as 15 mTorr, 60 mTorr, 100 mTorr with 5 min, 40 W conditions. The sheet resistance was measured with a 4-points probe (CMT-SR2000N, Changmin Tech., Korea). The sample size was set as 50 mm, and measurement was taken 100 times for each sample. The average sheet resistance of each condition didn't differ that much. However, 40 W / 100 mTorr / 5 min a achieved the lowest average sheet resistance of 0.76 ohm/sq.

2.2.4 Metal Patterning

After that, the patterning of the deposited metal layer was performed with conventional photolithography process. First, spin coating was done using a negative photoresist (DNR-L 300 series, Dong-jin Semichem., Korea) at 500 rpm for 5 s then 2000rpm for 40 s. The PFA attached wafer was baked for 100 s at 100℃ on a hot plate. The photoresist was exposed using an aligner (MA-6 III, Karl-Suss, Germany) with 25 mW of power for 10 s in the hard contact option.

Post exposure soft bake at 100℃ for 100 s on a hot plate was carried out, then the exposed photoresist was developed for 20 s (AZ 300 MIF Developer, Merck, Germany). Gold and titanium layers were etched, using a corresponding metal etchants. Gold etchant was made by agitating deionized water, potassium iodide, and iodine in 40: 4: 1 ratio. [98] After etching the gold layer, PFA loaded wafer was placed in titanium etchant around 5 s (GE-107, Soon Jung C\&S, Korea). Finally, the remaining photoresist was removed with acetone. The line width of the patterned metal electrode connection track was 50um, and the diameter of the electrode sites for stimulation was 200um. The metal line of the electrode was designed in a serpentine pattern to prevent cracks as the film is pressed in all directions during the subsequent thermal lamination process. The electrode pattern can be seen in Figure 94.

2.2.5 Thermal Lamination

After fabrication of electrodes on the substrate layer, the packaging using thermal lamination proceeded. Thermal lamination was performed to encapsulate the metal electrodes on PFA film with a 12.7 um-thick PFA film using a manual heat press machine (HC300-05, AS

ONE, Japan). The patterned substrate was covered with a cleaned 12.7 um-thick PFA film cover, then sandwiched between the PTFE films for detaching and the aluminum metal jig. Thermal annealing was performed at a temperature slightly lower than the melting temperature of PFA which is 300 ~ 310℃. The heated press was performed at 295℃ with a pressure of 50 bar for 20 min. Thermal lamination around the glass transition temperature of PFA, a force that spreads in all directions could distort metal patterns. Figure 94 shows that the electrode metal line with serpentine pattern to prevent line distortion during thermal lamination. Electrodes completely encapsulated through thermal lamination require connection pads and electrode sites opening for electrical connection. [99]

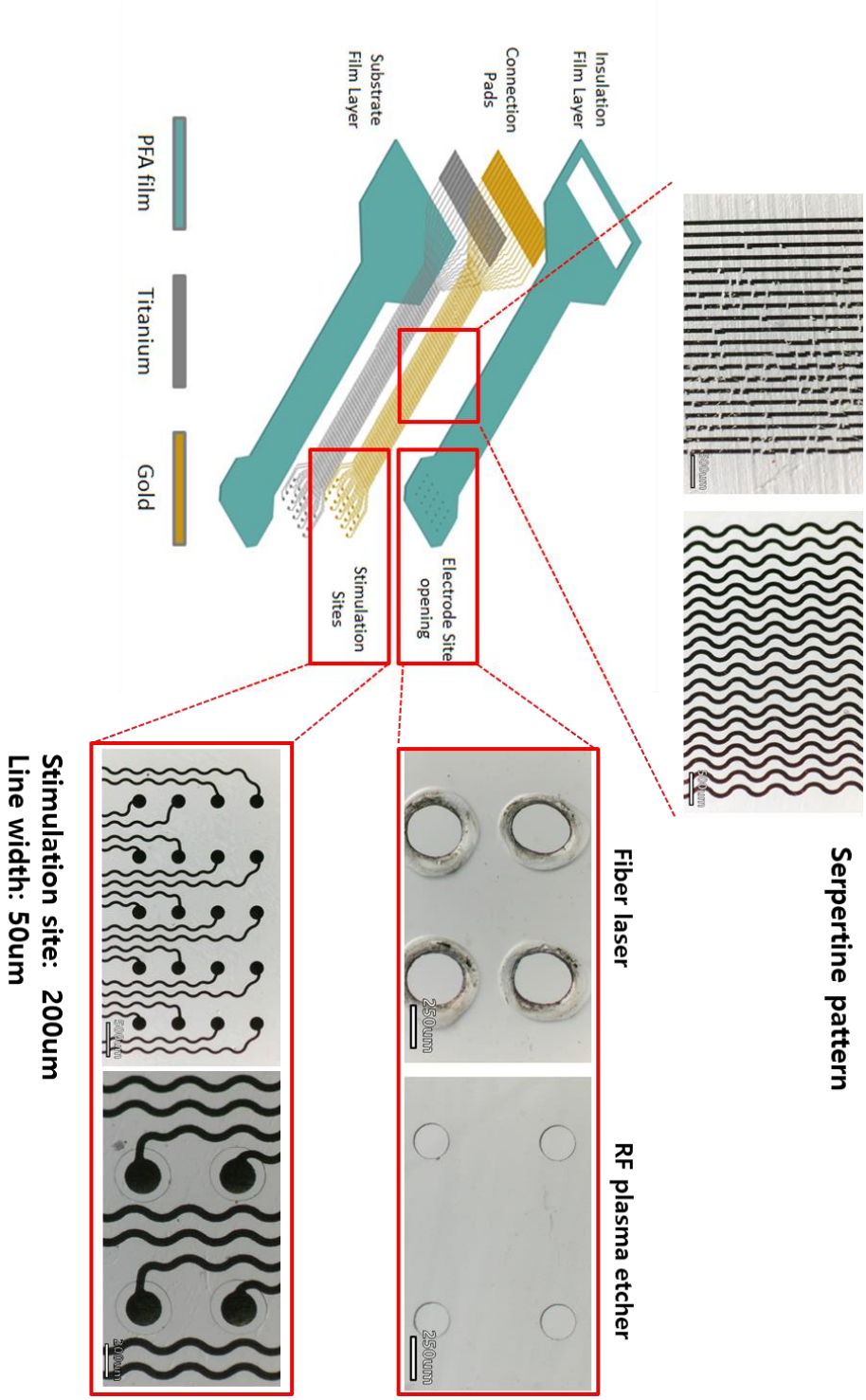

Figure 94 PFA-based electrode specification; Metal patterning, Site opening

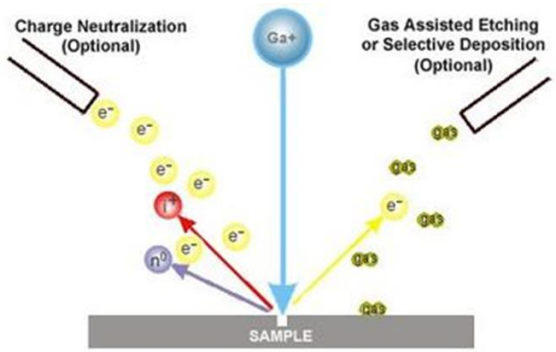

<Experiment conditions>

Beam	Energy	30keV
	Current	2.5nA
	Pattern	Spot
	Spot diameter	50Nm
	Spot overlap	50%
	Dwell time	1 x 10^{-6}sec
	Refresh time	0sec

$$(\text{Number of introduced ions}) = \frac{(\text{Number of scancs}) \text{ x } (\text{current}) \text{ x } (\text{dwell time})}{\text{e x } (\text{overlay})}, \text{e} = 1.602 \text{ x } 10^{-19}$$

<Results>

No.		Number of scans	Number of introduced ions	Depth
1	**Beam**	25	7.8 x 10^5	Penetrate
2		50	1.6 x 10^6	Penetrate
3		75	2.3 x 10^6	Penetrate
4		100	3.1 x 10^6	Penetrate
5		125	3.9 x 10^6	Penetrate

Figure 95 Electrode site opening with focused ion beam (FIB) laser

The focused ion beam (FIB) device is mainly used to observe a microscope image or process a sample surface by detecting electrons/ions generated by scanning a very finely focused ion beam on the sample surface. By using FIB laser device, the combined films were discriminately etched to open active electro-sites. The FIB laser equipment can selectively etch the surface of the PFA film by increasing amount of atoms sputtered, irradiating the surface with the gallium ion beam. As shown in Figure 95, PFA film is clearly dry etched when the experimental condition of ion beam was set over 25 scans and 7.8×10^5 of introduced ions. The number of introduced ions can be derived by multiplying number of scans, current and dwell time divided by overlayed electronic charge. As the scan times increase, number of introduced ions that irritates selective spot also gets higher.

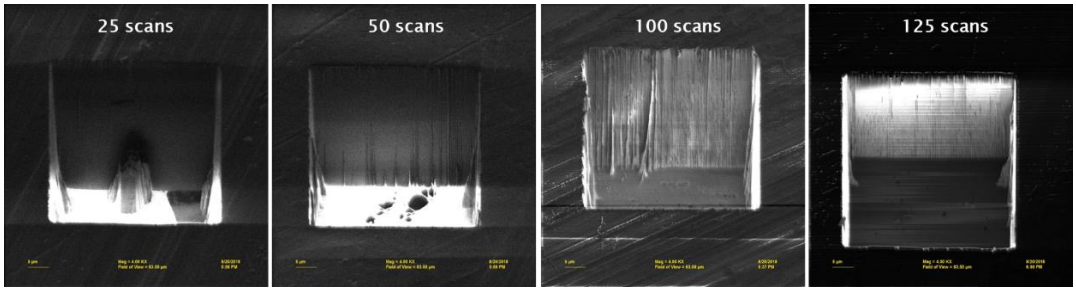

Figure 96 FIB images of the gallium focused ion beam etched PFA (Energy: 30keV; Current: 2.5nA; Spot diameter: 50Nm; Spot overlap:

50%; Dwell time: 1×10^{-6} sec)

As a comparison of processability, FEP fluoropolymer was also etched with FIB laser machine with same experimental condition. Both 50um thick fluoropolymers were penetrated after 25 of scans. From this investigation, FIB laser was verified to be used as an instrument for processing PFA film to open stimulation sites.

For better electrode site opening, fiber laser cutting and RF plasma etching were exploited. Using fiber laser for opening, the laser beam melts the edge of the targeted pattern, creating a much larger opening diameter than 200um. However, the RF plasma etching process achieved a clear opening site pattern without any film ablation. The opening site comparison of both methods is depicted in Figure 96. Therefore, RF plasma etching was used for the site opening.

RIE etcher (RIE 80 plus, Oxford Instrument, Abingdon, UK) is used to perform plasma etching using oxygen gas, CHF_3, and CF_4 gases. For this purpose, the gas flow rates during the etching for each gas were 50 sccm for oxygen, 10 sccm for CHF_3 and 10 sccm CF_4. The 200 W power with 40 mTorr working pressure was applied for 60 min. For electrode site opening, the aluminum layer with 3000Å thickness

was used as a sacrificial layer to protect the area except for the part to be opened.

Chapter 3. Results

3.1 Circuit Assembly

3.1.1 Transmitter Circuit

The circuit was designed in a 180 nm CMOS technology using both 1.8V and 5V transistors. Transistor-level simulations of the SCC have been carried out to estimate the performance of the circuit.

First, a WPT turn-on transient was simulated in order to verify the capability of the SCC to reach steady-state operation. The initial value of VO is set to 0 V and the input voltage Vrect is set to 1.4 V, close to the estimated threshold for the maximum conversion ratio n4 = 5. The results of this simulation are summarized in Figure 98. Three distinct phases may be noticed: (i) initially, with the output switch open, the start-up circuit shorts the converter input to the output, allowing the rectifier to directly charge the output storage capacitance Co; an enlarged view of the evolution of VO in this phase is shown in the lower right inset; (ii) once VO has stabilized to a value close to Vrect, the start-up auxiliary charge-pump is enabled, charging the output

capacitor to a voltage value high enough to guarantee a proper turn-on of the main converter switches; this value is around 2.4 V; (iii) the main converter kicks-in, rapidly charging Co towards the steady state value of VO; when VO exceeds a safe threshold (around 4.1 V) the output switch is closed and power starts being delivered to the load.

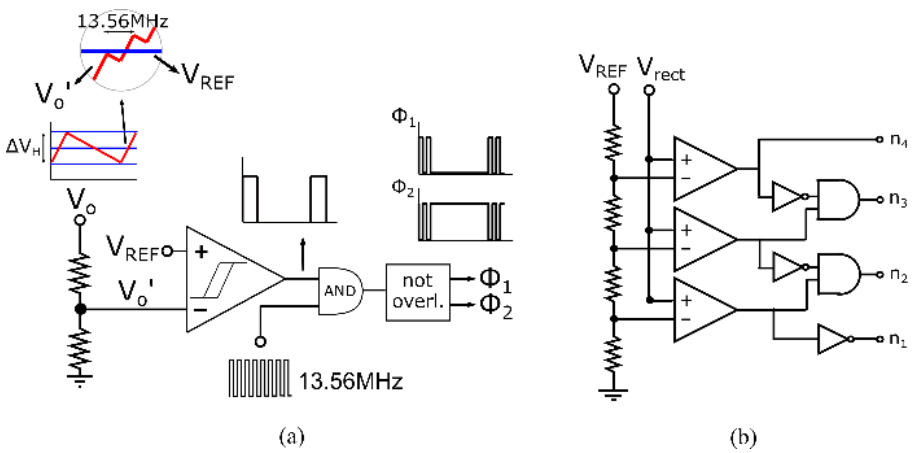

Figure 97 Blocks involved in the hysteresis output voltage regulation (a) and blocks to self-select the conversion ratios.

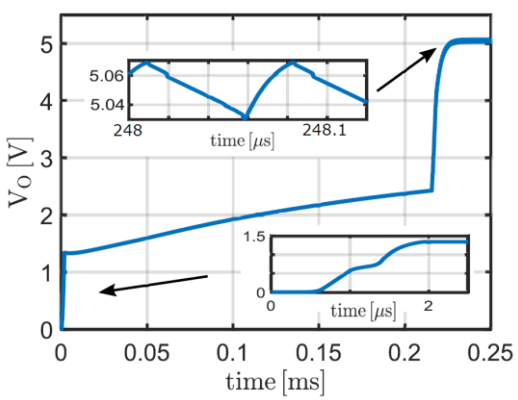

Figure 98 Output voltage time behavior during the WPT turn-on transient for Vrect = 1.4 V.

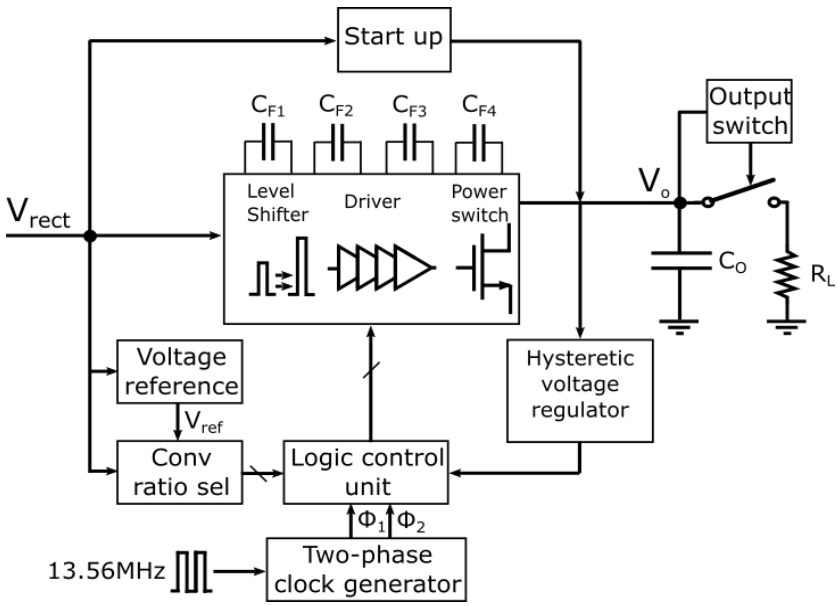

Figure 99 Full power converter design diagram

The upper inset in Figure 101 shows an enlarged view of the steady−state behavior of VO, highlighting the action of the hysteretic regulator that keeps VO on target by freezing the converter when VO exceed an upper threshold to turn it on again when VO drops below a lower threshold.

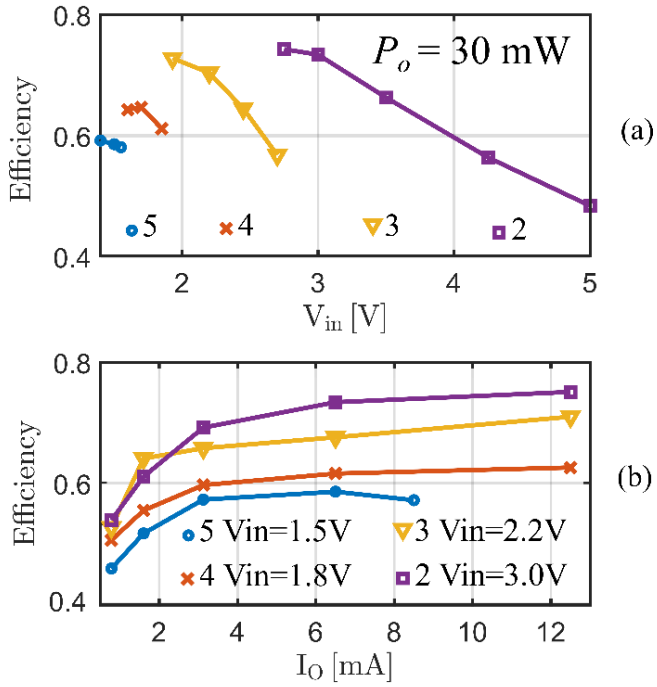

Figure 100 Steady−state efficiency of the converter as a function

(a) of the input voltage and (b) of the output current.

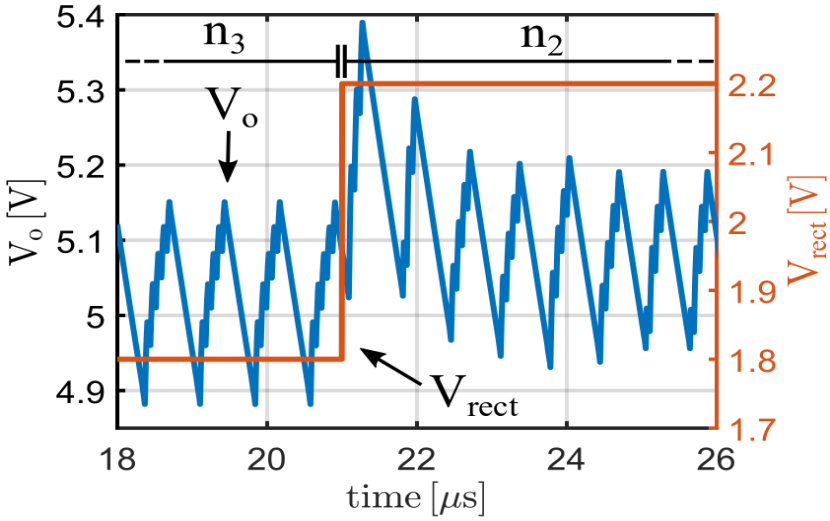

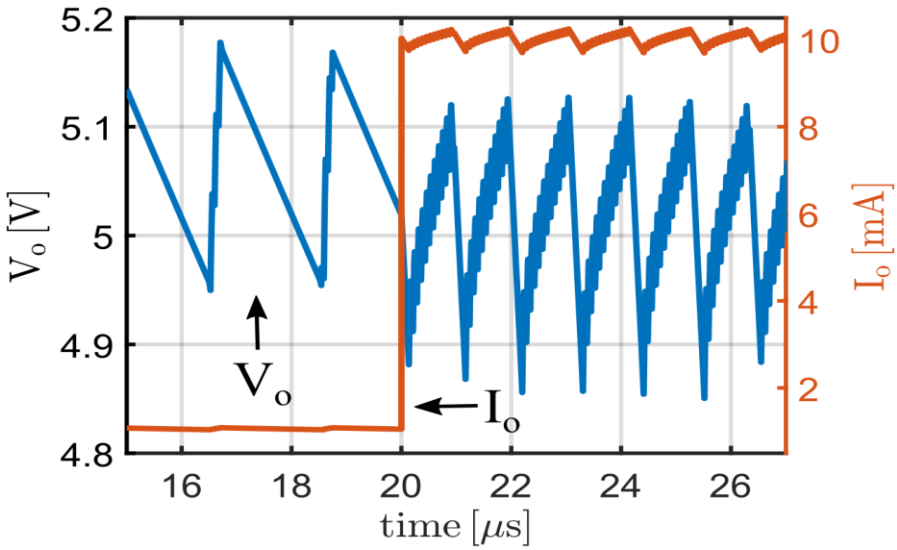

Figure 101 SCC transient response to a change of conversion ratio from n3 = 4 to n2 = 3 and the input voltage from 1.8 V to 2.2 V

The SCC efficiency in steady−state as a function of the converter input voltage is reported in Figure 100 (a). The conversion ratio ni is progressively decreased as VIN reaches the threshold corresponding to the next conversion ratio. Thanks to the adaptive conversion ratio, the SCC is able to handle the expected 1.3 V – 3.3 V range of the rectifier output voltage Vrect with an efficiency between 57 % and 74 %. Figure 100 (b) shows the simulated converter efficiency as a function of the output current Io for a set of different input voltage values, demonstrating, as expected, that lower conversion ratios guarantee a

larger efficiency. Finally, the transient response of the converter to a variation of the input voltage large enough to trigger a change of conversion ratio from n3 = 4 to n2 = 3 is shown in Figure 101. The simulation results show that steady-state operation is recovered in about than 2 μs.

We have presented a switched-capacitor, step-up converter based on Dickson topology designed to meet the requirements of implantable medical devices supplied by inductive wireless power transfer systems. We derived the peculiar specifications that the applications falling in the above category impose on the converter, with particular reference to the input voltage variability induced by the uncertainty in the magnetic coupling factor of the WPT.

We developed a simple model to estimate a priori the input voltage range, and proposed to resort to a reconfigurable converter that adapts the conversion ratio to the input voltage value, in order to minimize conduction power losses. We discussed in detail a procedure for the optimal sizing of the converter switches from the point of view of efficiency. The procedure is based on an analytical model of the switches conduction and driving losses and allows to derive the

absolute switch size that maximizes the reconfigurable SCC overall efficiency. A thorough set of transistor-level simulation results is included to demonstrate the performance and robustness of the converter.

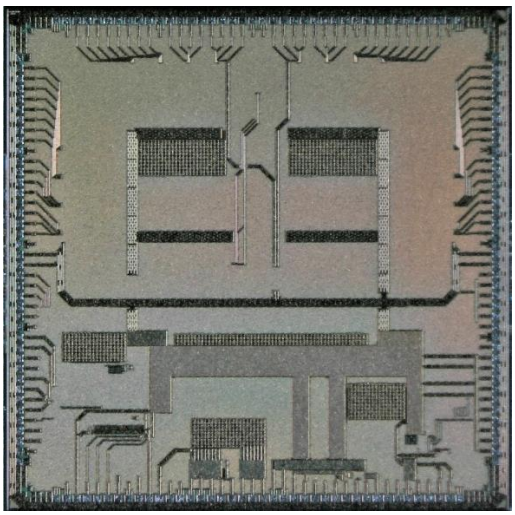

Figure 102 Die photograph of the fabricated silicon chip: stand alone

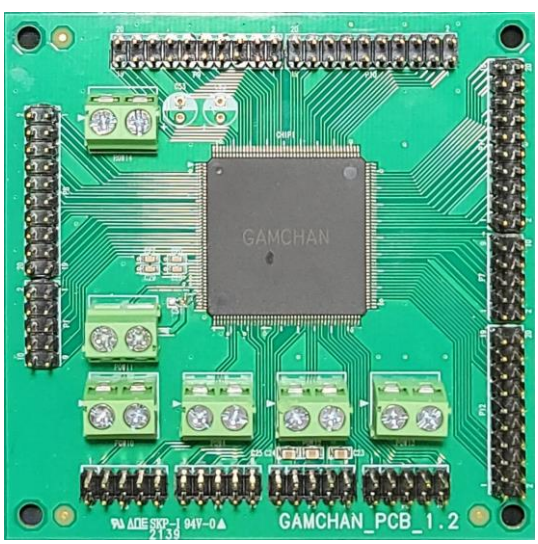

Figure 103 Die photograph of the fabricated silicon chip: within

the package and PCB board for I/O pins

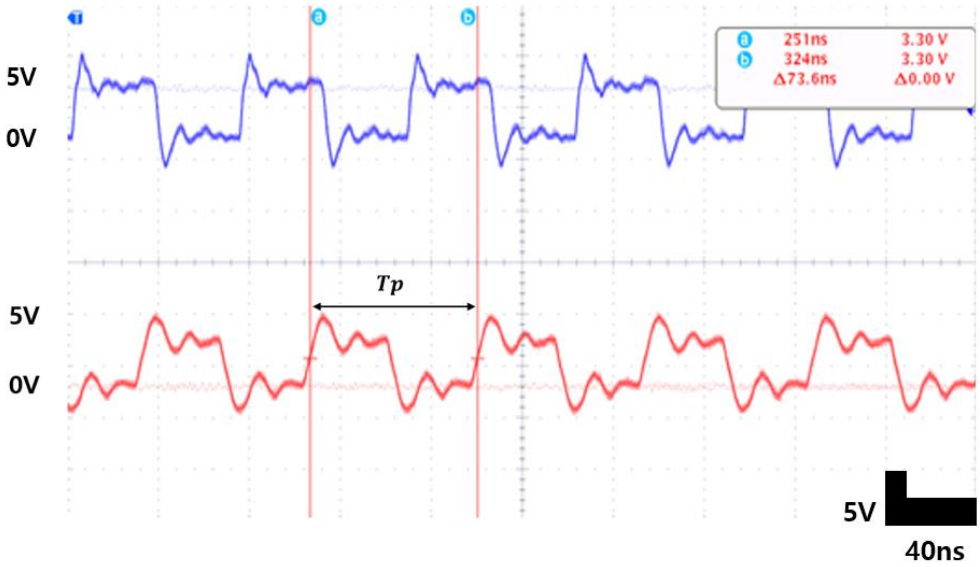

Figure 104 Power signal coming from non-overlapping clock generator (Blue line) and power amplifier (Red line)

By testing data transfer system part, to generate 5ns of data pulse S1 and S2, 7.5uA and 11uA of bias current were needed. To achieve these value, potentiometer was used, 360kohm and 530kohm respectively. The two narrow pulses generated from pulse pattern generator go through h-bridge to get different polar as shown in Figure 105.

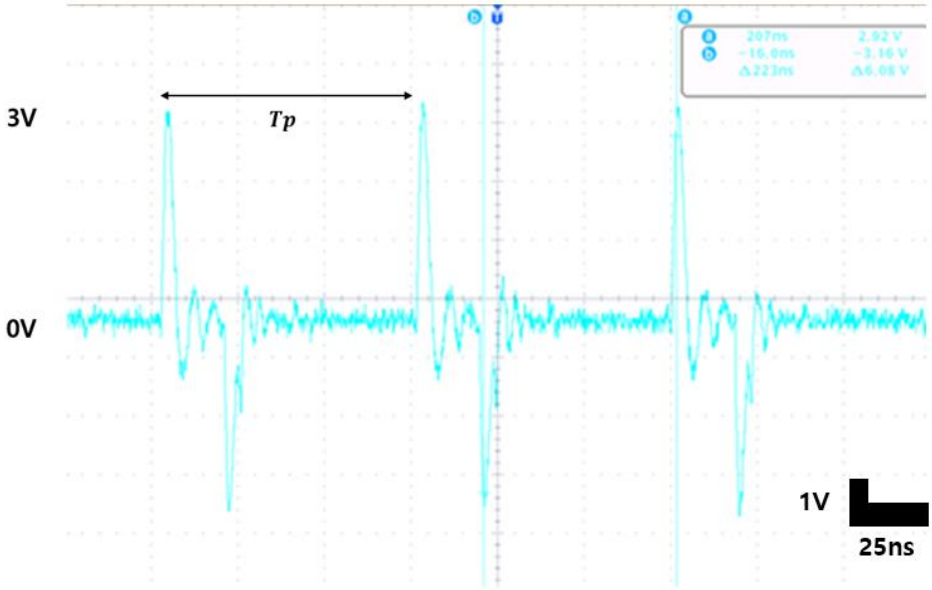

Figure 105 Pulse pattern generator output signal and output signal from h-bridge

3.1.2 Receiver Circuit

With the power receiver stand-alone test, the low drop voltage output system had an output of 1.78V with 5V supply voltage. The main reconfigurable DC-DC step up converter worked in the range of input voltage from 1.8V to 3V. Following Figure 106 shows the output voltage of step-up converter when the input voltage is 2.8V. Also, the received power carrier interference from data receiver showed shifted signal from Figure 104.

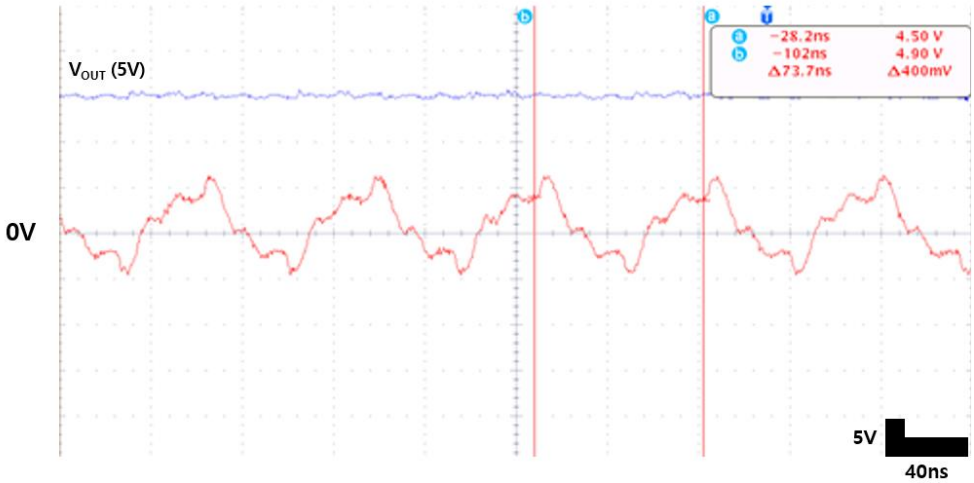

Figure 106 Output voltage of 5V from DC-DC step-up converter (Blue line) and received voltage from data receiver (Red line)

As shown in Figure 107, the external reference voltage controlled from 0.7V to 1.5V to compare the left shifted voltage due to data ringing. The external voltage reference could be different depending on the process variation. The data ringing has shifted the zero-crossing of the power carrier interference signal in data receiver system by 2.5ns. The transmitted serial data bit from was recovered through pulse delay modulation scheme, achieving 13.56Mbps data rate which is the same value of the power carrier frequency 13.56MHz.

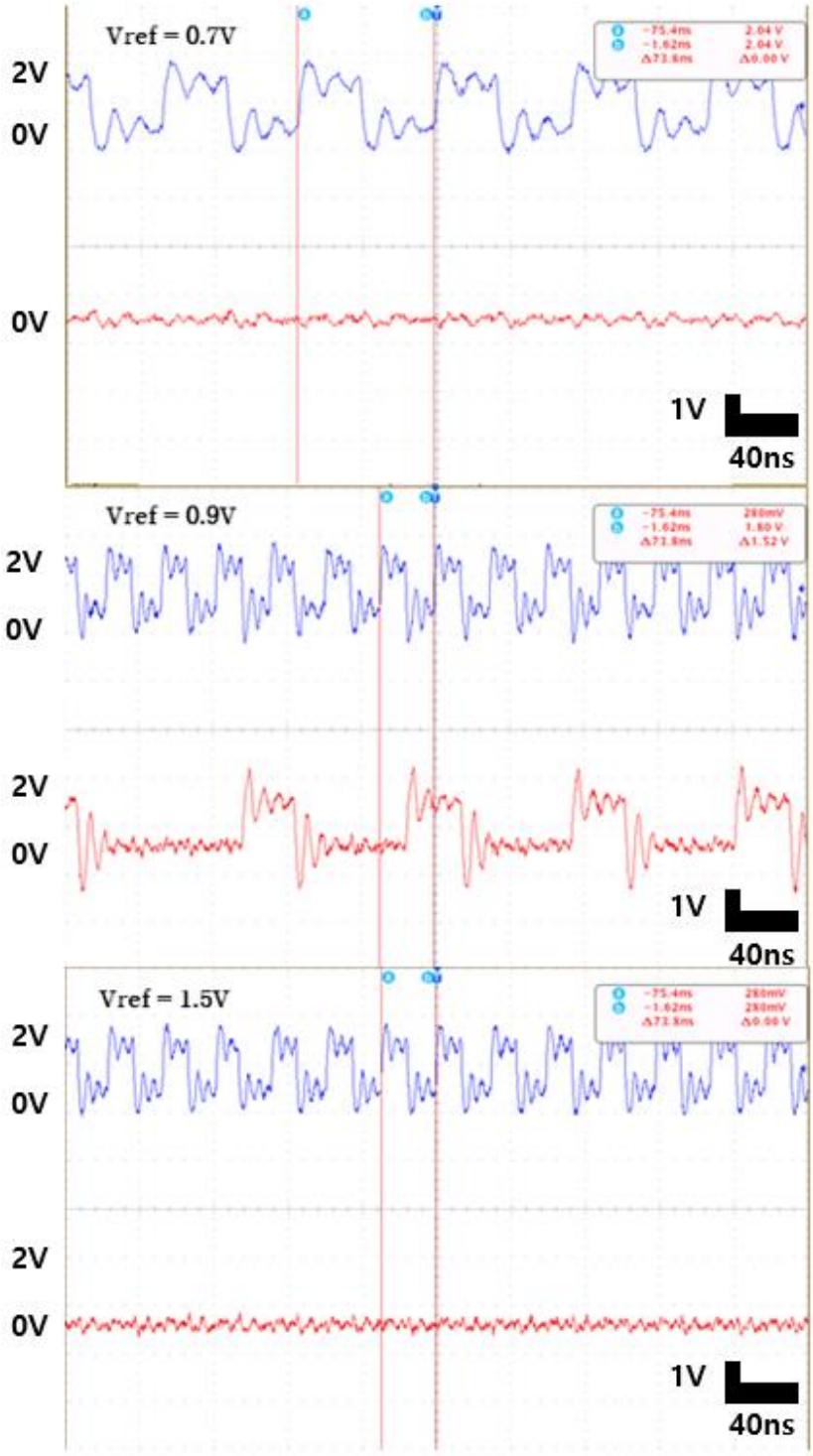

Figure 107 Recovered data signal (Red line) depending on the external reference voltage for signal comparison

3.1.3 Coils for Power and Data System

The simulation data and heat generation due to electromagnetic from spiral planar pair of coils for artificial retinal implant were analyzed by COMSOL Multiphysics. Planar spiral outer and inner coils for an implantable artificial retina were designed and analyzed. The whole geometry was designed in a transplant situation. The parameters of the coil were set within the design limits due to the limitations of implant space. The inductance for the coil and the thermal change due to the electromagnetic force generated in the inductively coupled coil were calculated [100] – [102].

Table 13 Design parameters of spiral planar coils

	N	W[mm]	S[mm]	T[mm]	Di[mm]	Do[mm]
Outer	10	0.45	0.2	0.1	8.7	15
Inner	8	0.45	0.2	0.1	1.5	6.5

The designed planar spiral coil has a design parameters; metal line width (W), winding trace thickness(T), interwinding gap(S), outer inductor diameter (Do), inner inductor diameter (Di) and number of coil

turns(N). All parameters of spiral planar coil are shown in Table 13.

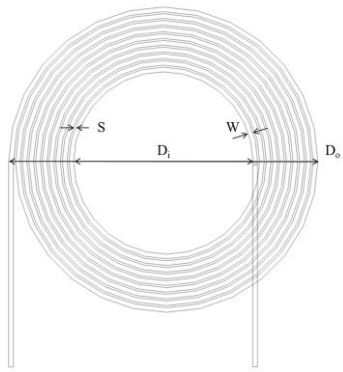

Figure 108 Dimension of planar spiral coil

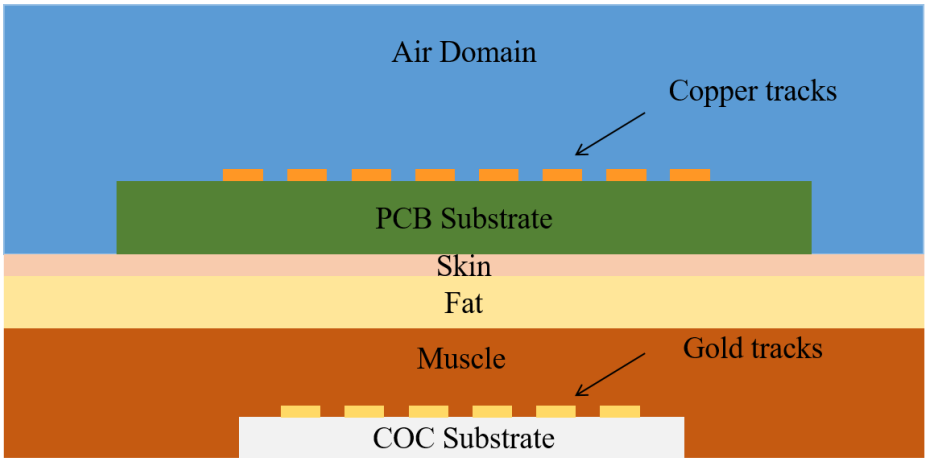

Figure 109 2D Symmetric schematic of inductive coupled coils

The outer coil was powered by direct voltage Vo = 200V and inner coil Vi = 30V. A very important parameter of the simulation is the mesh. The correct size and shape of the mesh elements will affect the

accuracy of the solution. The finer the mesh elements, the higher the analysis accuracy. Mapped mesh for both coils was used.

It can be seen from Figure that the maximum magnetic flux density is induced in the innermost turn of the non-helical planar coil structure.

The current splitting pattern of the non-helical coil winding which can be seen from Figure, causes this magnetic field distribution. The innermost turn of the coil structure has the lowest resistance of all coil turns, so the maximum current will reach there, leading to the maximum magnetic field in the innermost turn. Figure shows the yz-axis current density distribution for outer coil. From the simulation, the inductance of outer and inner coil were 2.99uH and 0.443uH respectively.

The two coils designed together with the internal tissues of the body were analyzed for heat generation through heat transfer in solid. The skin, fat, and muscle layers of living tissue were prepared based on the average adult body temperature of 36.5℃, and the external coil was set to 24℃, which is room temperature, and the body coil was set similar to body temperature.

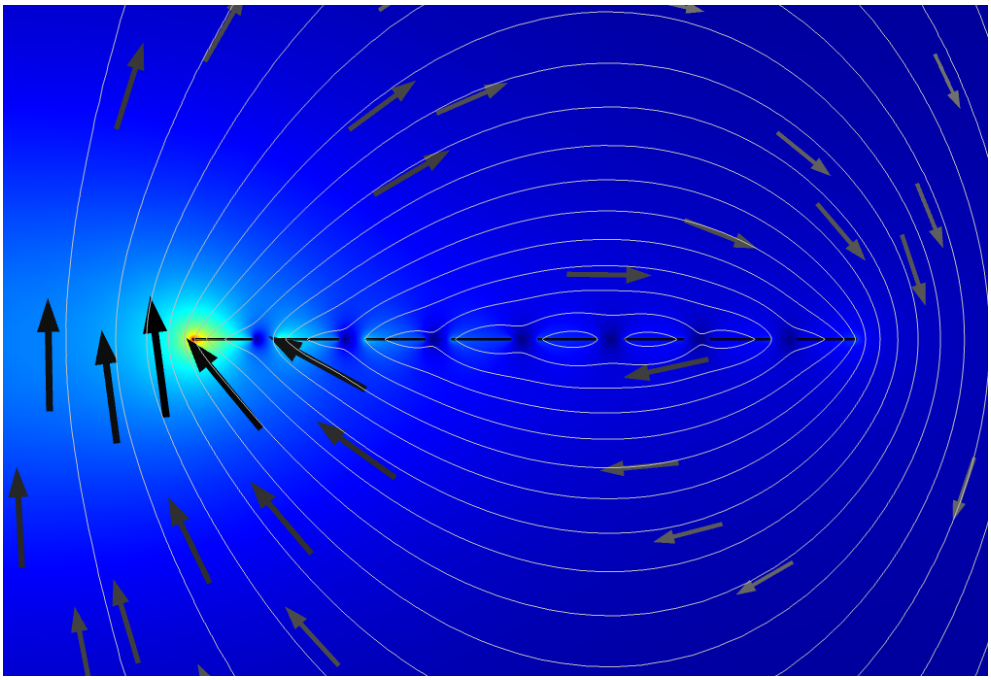

Figure 110 Current density of outer coil

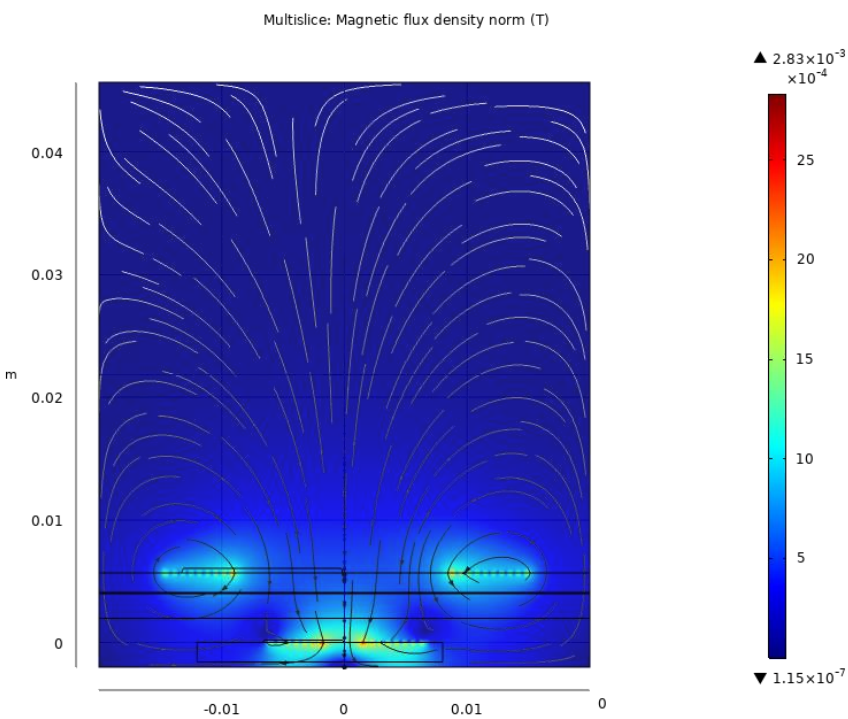

Figure 111 Surface yz-axis magnetic flux density [T]

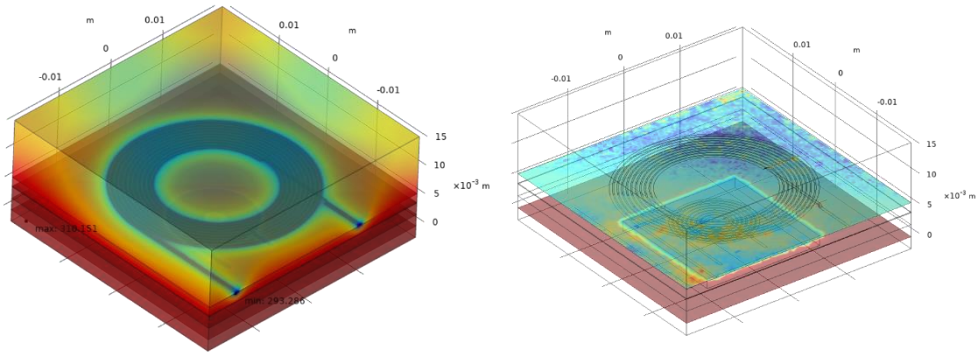

(a) (b)

Figure 112 a) Maximum and minimum temperature arise in biological tissue model due to wireless powered coils b) Cross sectional view for temperature variation in tissue model [K]

As shown in Figure 112, the simulation result, the maximum temperature was 310.151 K and the minimum temperature was 293.286 K, which were not all within the range to cause damage to the internal tissues of the body. If the applied heat is above 44℃, a minimum of 6 hours is required, tissue damage occurs. At the skin surface above 44℃ but below 51℃, the rate of thermal damage doubles for every 1-degree increase in temperature. Temperatures above 51℃ will cause almost instantaneous destruction of the epidermis. Muscle damage was assessed with indicators such as blood creatine levels, neuromuscular function, hemorrhage, and appearance of necrosis.

There was acute but minor damage to the muscles when thermal dose concept CEM43 was between 41 and 80 minutes. At CEM43 higher than 80 min, the injuries (hemorrhage and necrosis) became more chronic and severe [103].

Planar spiral outer and inner coil for implantable artificial retina was designed and analyzed. The full geometry was designed under the circumstance of implantation. Parameters of coil were set within the design restriction due to limitation of implant space. Those inductances for coils and thermal variation due to electromagnetic force generated from inductively coupled coil were calculated using the finite element method used by COMSOL Multiphysics. After analyzing heat transfer in biological model, the maximum heat didnt exceed the temperature occurs tissue damage. As a result, the designed pair of coils for artificial retina could be implant under in vivo without destruction of body tissue.

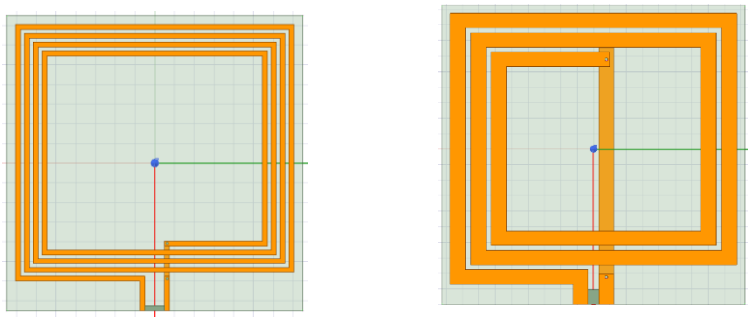

Figure 113 Power coils designed from Ansys

Table 14 Simulation and measured results of designed power coils

	Simulation results	Measurements
Size	30 x 30 mm^2	
Substrate	FR4	
Frequency	13.56 MHz	
L1	805 nH	840 nH
Q1	93.04	92.28
L3	167.8 nH	177 nH
Q3	80.69	76.7

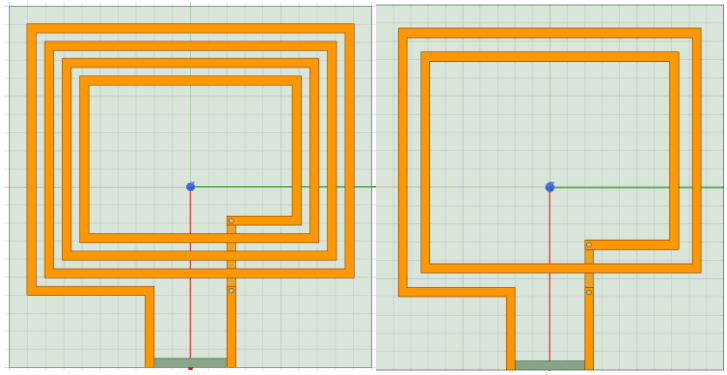

Figure 114 Data coils designed from Ansys

Table 15 Simulation and measured results of designed power coils

	Simulation results	Measurements
Size	10 x 10 mm^2	
Substrate	FR4	
Frequency	50 MHz	
L2	163.84 nH	175 nH
Q2	96.24	62
L4	60.45 nH	62.2
Q4	79.01	49.6

3.2 Wireless Operation

3.2.1 Bit-Error-Rate (BER)

By repeating the data transfer, the usual standard bit error rate of 10^{-6} could be achieved with litz wire coils. However, more precise bit error rate measurement should be followed in the future by varying the alignment, distance of the coils with much longer data chain. The use of crystal-based oscillators with sub-nanosecond jitter is feasible in the external power Tx due to its relatively relaxed size constraints. In systems with high jitter oscillators, PDL should be reduced to increase the amount of zero-crossing shifts or SIR to keep the BER low. Furthermore, in a complete system, the data Tx block can actively adjust in a closed loop to maintain its optimal value for the lowest BER.

3.2 Validation of Electrode Performance

3.2.1 Electrochemical Characteristics

The impedance and charge storage capacity of fabricated electrodes were measured using the Si 1260 impedance/gain phase analyzer (SolarTron, UK). Ag/AgCl reference electrode, Pt counter electrode, and PFA electrode was immersed in a beaker with 200 ml of PBS(PBS, PH 7.4, Thermo Fisher Scientific Solution Inc., MA, USA),

and the Impedance Analyzer (SI 1287 Electrochemical Interface (SolarTron, UK) interfaced with it. An Au-based electrode was also prepared to compare the electrode performance with Ti-Au based sample. One was prepared the same as the previous study (Au), while the other followed the proposed steps (Ti-Au).

From Figure 115, the impedance and charge storage capacity (CSC) are compared between polymer-based electrodes. The impedance of the Au-based electrode at 1kHz was 1.55 kohm, and the Ti-Au based electrode was 1.59 kohm at 1 kHz. For CSC, Au PFA electrode showed 0.67 mC/cm^2, while Ti-Au PFA electrode got 1.257 mC/cm^2. As a comparison, the LCP-based gold electrode showed 26.65 kohm of impedance at 1kHz and CSC of 0.32 mC/cm^2 [104]. Also, the COC-based Ti-Au based electrode showed 1.57 kohm at 1 kHz and CSC of 0.31 mC/cm^2 [105]. These results showed that both PFA based Au / Ti-Au electrodes have faultless performances compared to other biocompatible polymer materials-based electrodes. Especially Ti-Au electrode showed excellent CSC compared to other biocompatible polymer-based electrodes due to its micro-protrusion structure surface after pretreatment.

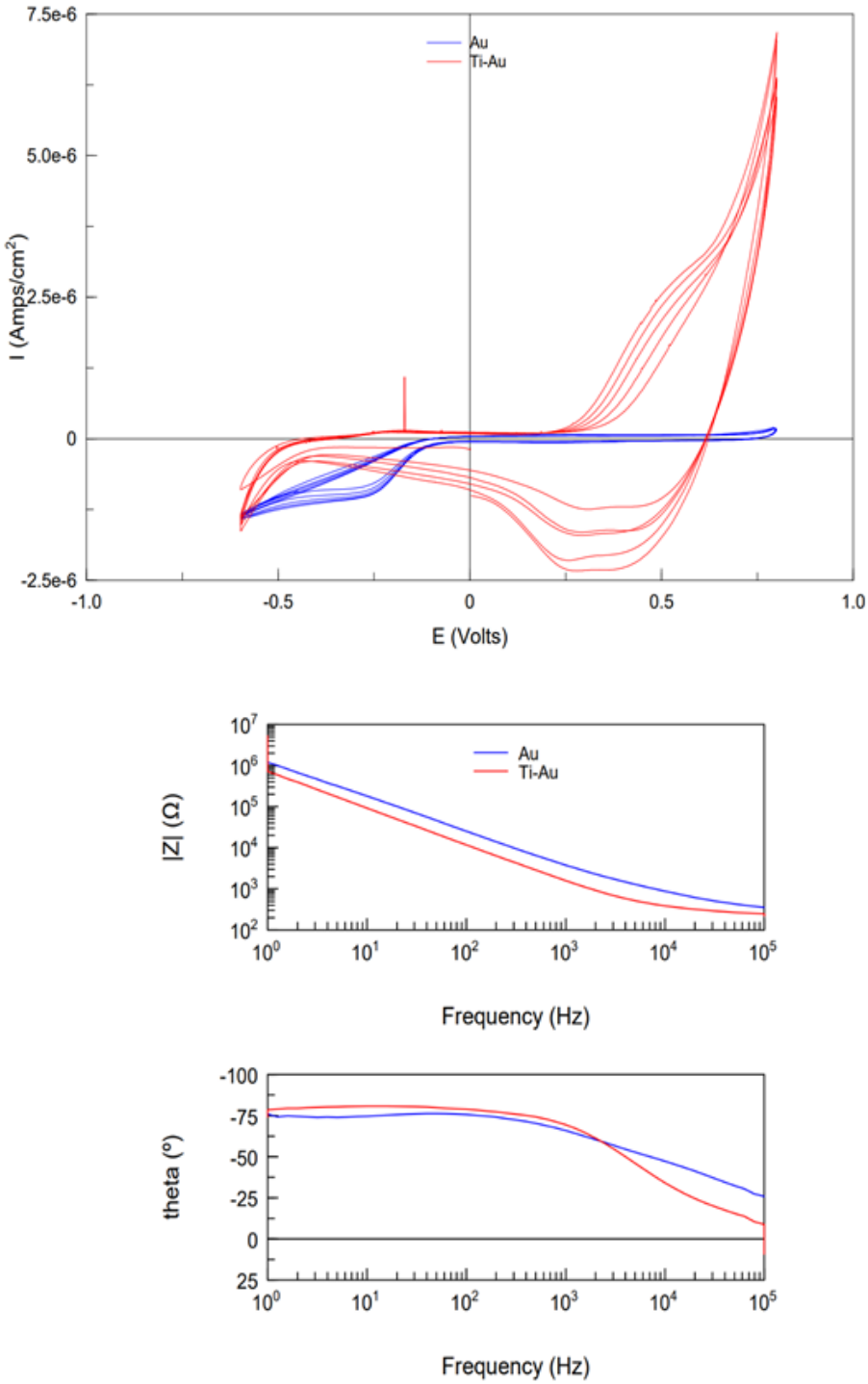

Figure 115 Electrical characteristics of PFA based MEAs. Charge storage capacitance and impedance

Table 16 Impedance and charge storage capacity comparison chart

with different polymer based electrodes

	PFA (Au)	PFA (Ti-Au)	COC	LCP
Impedance @ 1kHz(kΩ)	1.55	1.59	3.68	26.65
CSC (mC/cm^2)	0.67	1.257	0.31	0.32

3.2.2 Mechanical Characteristics

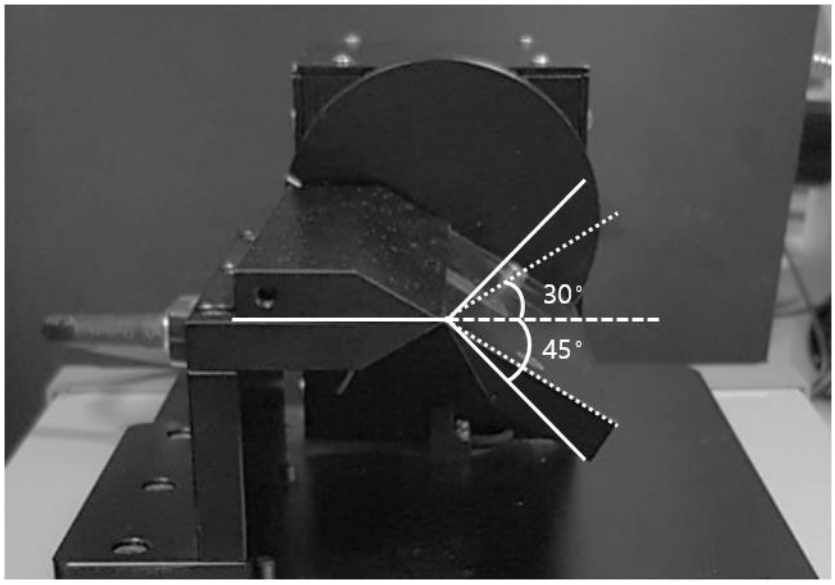

Figure 116 Bending test experiment setup. The bending angle was set

as ±30° and ±45°

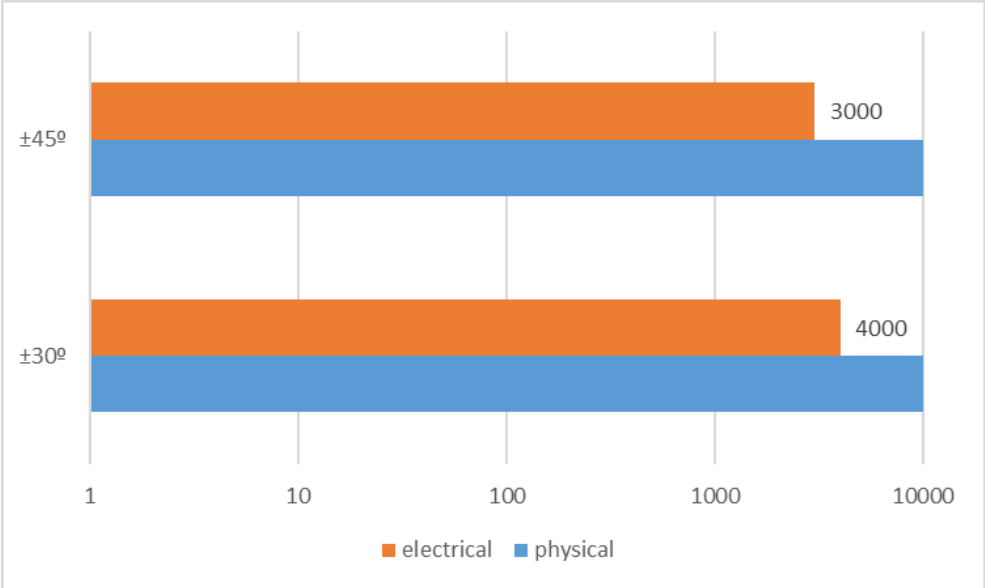

Figure 117 Electrical and physical connection lost for both angles of bending test

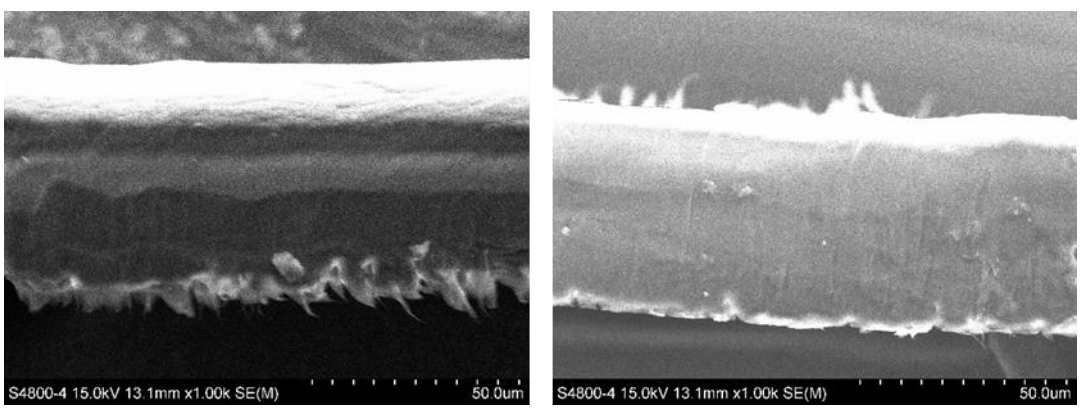

Figure 118 Cross section SEM view of electrode sample after the bending test

Typically, implanted electrodes experience various physical disturbances. Therefore, 62.7um-thick(50um substrate + 12.7um

cover) PFA planar electrode was analyzed through a mechanical bending test. Bending test apparatus (32-03675-01, ST1, Korea) and 1-axis motion controller (STM-1-USB, ST1, Korea) set repeated bend test for ±30°, ±45° angle conditions as shown in Figure 116. The electrical connection for the prepared electrode was maintained until 4000 and 3000 iterations for ±30°, ±45° respectively. The electrical connection was measured with digital multimeter. For each electrical disconnection iterations, the criterion resistance was set as 25Ω. The physical fracture didn't occur over 10,000 iterations for both bending angle conditions (Figure 117). The physically bend location was checked through Scanning Electron Microscope(SEM) (Figure 118). This endurability from external fatigue showed substantial PFA merit as implantable neural electrode packaging, which might require repeated bending circumstances.

3.2.3 Biocompatibility *in-vitro*

To evaluate the long-term reliability of PFA encapsulation in a physiological setting, a multi-inter digitated electrode (MIDE) was used for leakage current measurements during an accelerated life test

in-vitro. The soak tests were performed in a 75℃ PBS solution (D8537-500ML, Sigma-Aldrich, Burlington, MA). [105] As shown in Figure 117, the MIDE array consists of six interdigitated electrodes (IDE) designed to detect leakage current at each location. These IDEs (Channels 1, 2, 3, 5, 6) were soaked to detect the penetration of moisture and ions through PFA encapsulation, while the other IDE (Channel 4) was not soaked to use as control group. Both the width and spacing of the IDE pattern was 300um, and the width of the connecting line was 130um. Each IDE was connected to two pads via double interconnect lines to verify electrical connections during the experiment.

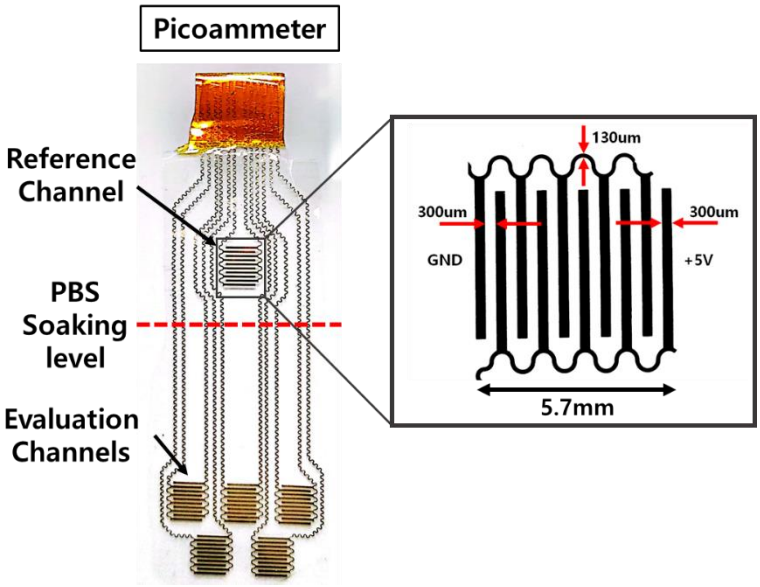

Figure 119 MIDE fabricated for accelerated soak test

MIDE prepared for leakage current measurement was placed in a test bottle with a 75℃ PBS solution in a forced convection oven. A 5 V direct current (VDC) bias was regularly applied between the IDE during the *in-vitro* accelerated life test using the standard 24-pin FFC connector to connect the IDE to the power supply (PWS-3005D, Providence, Korea). Then, the leakage current was measured with a pico-ammeter (Model 6485, Keithley Instruments, Inc., Cleveland, OH). The MIDE array consisted of six interdigitated electrodes (IDEs) designed to sense the electrical leakage current at each location. Four of the six IDEs were placed in the outer area. One IDE was centrally placed. These IDEs were soaked to detect the permeation of moisture and ions through the LCP encapsulation, while the other IDEs were not soaked for control experiments. Both the width and spacing of the IDE pattern are 300 μm, and the width of the wiring is 300 μm. Each IDE was connected to two pads via double wiring to verify electrical connectivity during the experiment. Accelerated life testing (ALT) is a convenient and cost-effective solution for determining the reliability and robustness of an electronic product or component (Figure 119).

10-degree rule' is generally used in many applications to

approximate the device's expected life. This rule suggests that whenever the temperature increases by 10℃, the expected life of the device reduces by half [106]. The value from simplified protocols for accelerating aging proposes valuable performance and shelf life data for designed implantable electrodes.

As shown in Figure 120, the reliability of the electrode can be checked in a similar environment in the body through the acceleration test results. Measured channels showed a very stable current throughout the test. From [107], average current data of different biocompatible polymer-based IDEs were extracted for comparison. The leakage current values from Polyimide, Parylene-C, and LCP-based samples started around 10^{-12}A, while PFA-based IDE began with a relatively higher value, 10^{-9}A. The leakage current from Polyimide and Parylene-C based IDEs exceeded 1uA safety limitation around 60 days and 120 days, respectively. Other IDEs except the PFA-based sample showed a steep increase of leakage current after starting the soak test, while value from PFA IDE maintained stability. According to the 10 degrees law, 30 days at temperature at 75℃ is equivalent to 480 days in the human body environment. Therefore, the

acceleration of PFA packaging, which is currently under 180 days, can last at least 8 years *in-vivo* environment. The accelerated life test for PFA-based IDE is still going on without any contortion.

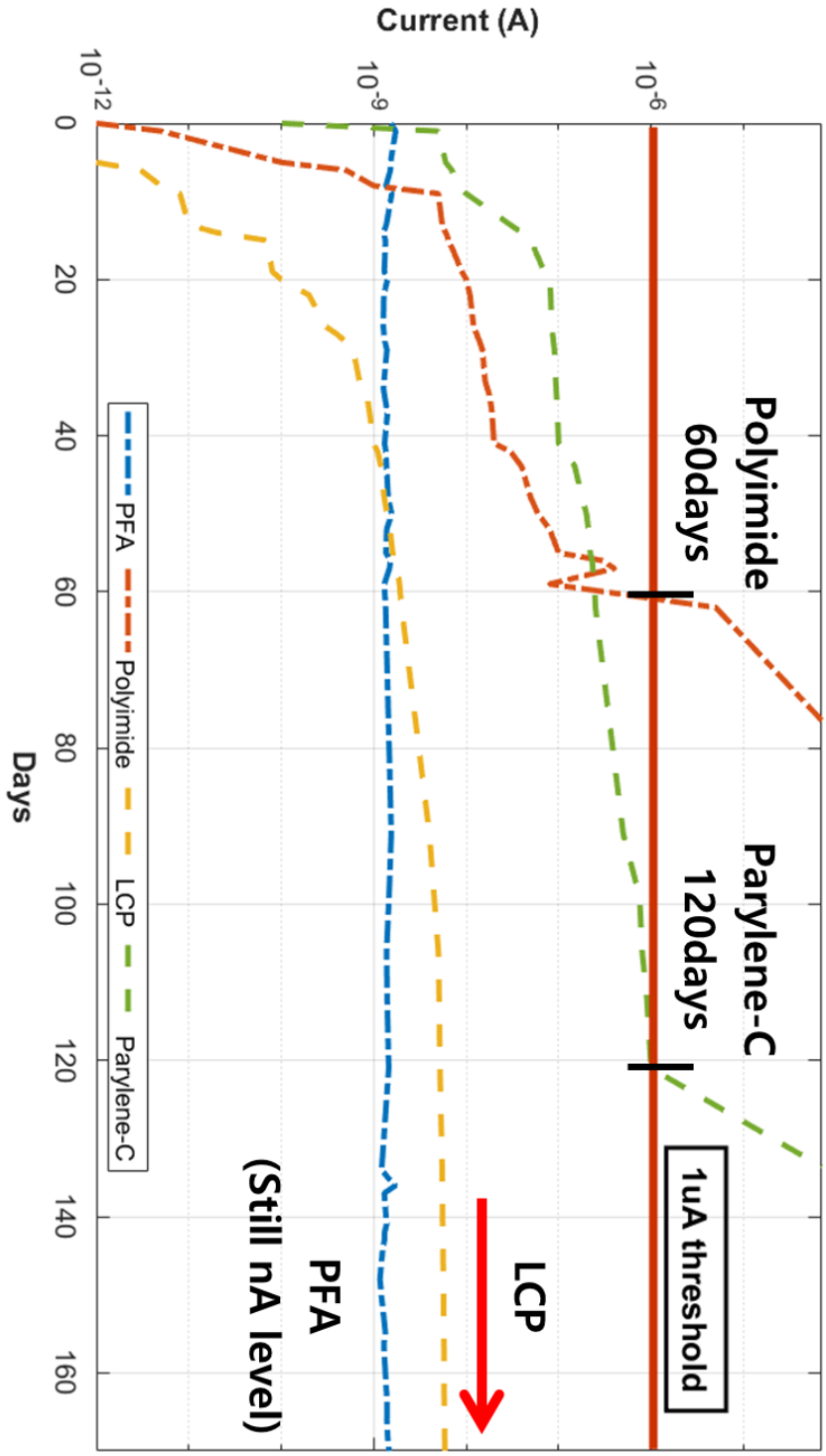

Figure 120 Leakage current of different polymer based IDE samples during accelerated soak test in 75℃ PBS solution

The results of *in-vitro* biocompatibility of PFA can be seen in Table 17. The cytotoxicity test and elution test were proceeded to appraise biocompatibility of designed planar PFA-based electrodes. The elution test shows appearance, pH difference, $KMnO_4$ reduction and evaporation residue of PFA eluted solution. The appearance of eluted PFA solution was transparent and clean. The pH difference between the result and control showed 0.5. In $KMnO_4$ reduction, the result and the control showed a 0.3 mL difference. Moreover, there was no residual substance for eluted PFA solution. The result of the heavy metal test was not darker than the control. From the elution test, the PFA can be considered acceptable in the criteria. The detailed results are shown in Table II. From cytotoxicity test, the cell survival rates were higher than the 70% threshold, in the range from 89.96% to 100.27%. This result shows PFA doesn't bring out toxicity to living cells compared to control group.

Table 17 Biocompatibility of PFA based MEAs

	Items	Pass Criteria	Control	Treat
Elution test	Appearance	Clear	-	Clear
	pH	|Control - Treat |$\leq$ 1.5	6.19	6.24
	$KMnO_4$ Reducing substance	|Control - Treat | $\leq$ 2.0 mL	17.6 mL	17.9 mL
	Residue on Evaporation	$\leq$ 1.0 mg	-	0 mg
	Heavy metal	Treat <Control	-	Not darker than Control
	UV Spectrophotometer	$\leq$ 0.1	-	0.002

	Group	Treated Time (hour)	Test Item	Concentration (% (v/v), in media)	Absorbance (Mean $\pm$ SD)	Survival Rate (%)
Cytotoxicity Test	Blank	24	MEM	-	0.783 $\pm$ 0.025	100.00
	Negative Control	24	HDPE	100 % extracts	0.650 $\pm$ 0.022	82.91
	Treatment	24	PFA	100 % extracts	0.705 $\pm$ 0.009	89.96
				75 % extracts	0.709 $\pm$ 0.017	90.44
				50 % extracts	0.758 $\pm$ 0.010	96.73
				25 % extracts	0.752 $\pm$ 0.021	95.99
				12.5 % extracts	0.786 $\pm$ 0.013	100.27
	Positive Control	24	0.25 % ZDBC	100 % extracts	0.065 $\pm$ 0.001	8.27
				50 % extracts	0.447 $\pm$ 0.017	57.06

MEM: Minimum Essential Medium; HDPE: High Density Polyethylene; ZDBC: Zinc Dibuthyldithiocarbamate;

3.2.4 *Ex vivo* Stimulation Validation

For ex vivo evaluation of the stimulation chip and microelectrode array, freshly harvested rodent retina was used. All animal procedures were approved by the Institutional Animal Care and Use Committee (IACUC) at Ewha Womans University (IACUC 22-007). The mouse (C57BL/6N, male, 8 weeks) (KOATECH, Pyeongtaek-si, Korea) was anesthetized through inhalation using isoflurane (Ifran, Hana Pharm Co., Korea) for 5 minutes. After the cervical dislocation, both eyes were enucleated and the whole layers of retinae were harvested.

The retinal patch was prepared under dim red light in artificial cerebrospinal fluid (aCSF solution : 124 mM NaCl (Sigma-Aldrich, St. Louis, MO, USA), 5 mM KCl (Sigma-Aldrich, St. Louis, MO, USA), 1.15 mM KH2PO4 (Junsei Chemical Co., Ltd., Tokyo, Japan), 1.15 mM MgSO4 (Junsei Chemical Co., Ltd., Tokyo, Japan), 10 mM D(+)-glucose (Junsei Chemical Co., Ltd., Tokyo, Japan), 25 mM NaHCO3 (Sigma-Aldrich, St. Louis, MO, USA), 2.5 mM CaCl2 (Sigma-Aldrich, St. Louis, MO, USA)) bubbled with 95% O2 and 5% CO2 at room temperature, and placed onto the 64 channel recording microelectrode array (perforated microelectrode array; pMEA 200/30, 30um of

electrode site diameter and 200um of spacing; Multi Channel Systems MCS GmbH, Reutlingen, Germany) as epiretinal side down, to record the retinal ganglion cell activities (Figure 121, 122).

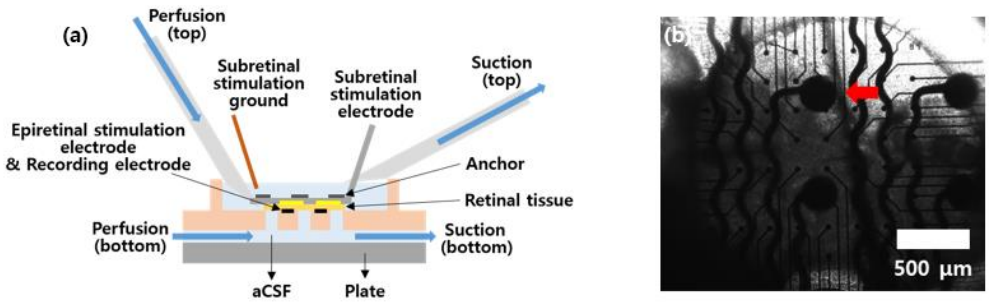

Figure 121 Experimental setup for ex-vivo evaluation; (a) schematic diagram of the setup, (b) The red arrow indicates the area of the electrode to which electrical stimulation has been applied.

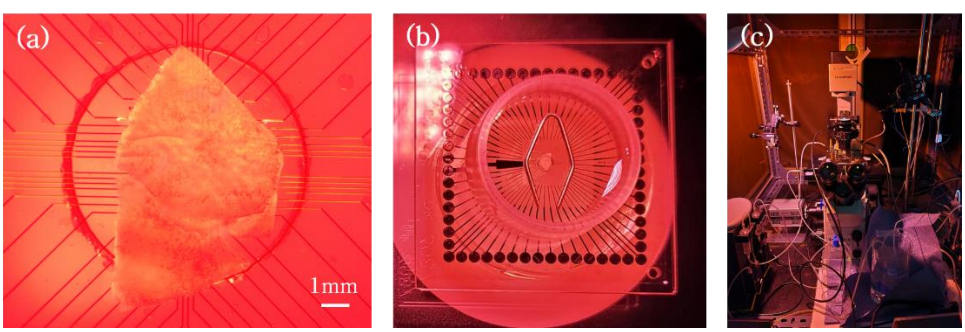

Figure 122 a) Attached retina patch onto the recording electrodes. b) Nylon mesh anchoring was applied for better attachment of the harvested retina onto the microelectrode array. c)

Experimental setup for the ex vivo stimulation

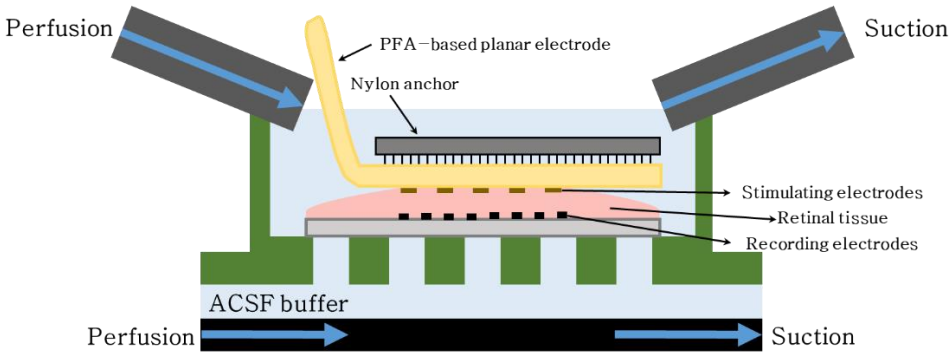

Figure 123 Schematic diagram of the *ex vivo* subretinal stimulation

Electrical stimulation was given to the harvested retina by the PFA film-based electrodes (Section 2.2, electrode stimulation site 200um with 800um spacing), which was placed over the retina. This results in the subretinal electrical stimulation, because the epiretinal side containing ganglion cell layer is attached over the recording MEA (Figure 123).

Stimulating electrode was gently held over the retinal patch by nylon mesh, supported by the stainless ring. During the electrical stimulation, oxygen-bubbled aCSF was continuously perfused and drained in the upper and lower space of the retinal patch as shown in Figure 123. By doing this, the contact between tissue and stimulation

electrode can be enhanced and improve oxygenation [108] – [110].

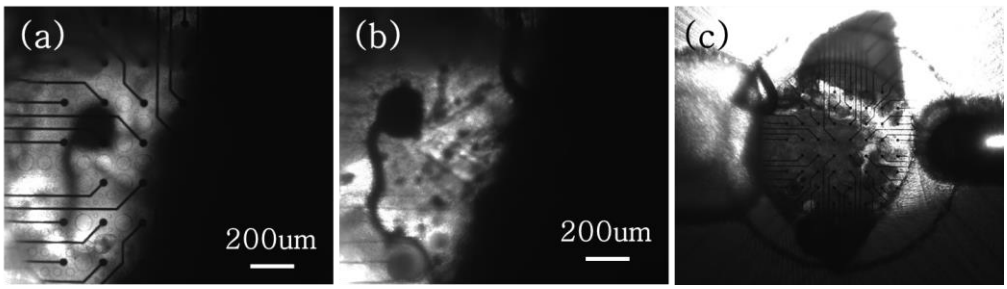

Figure 124 Microscopic view of the ex vivo experimental setup. Focused on the level of a) recording electrodes and b) stimulation electrodes. c) Perfusion chamber perfused with aCSF.

From recording pMEA, spontaneous spikes of ganglion cells between 3 to 12 Hz were recorded (Figure 125) from around half of the electrode channels, which was 50 ~ 100 uV of voltage.

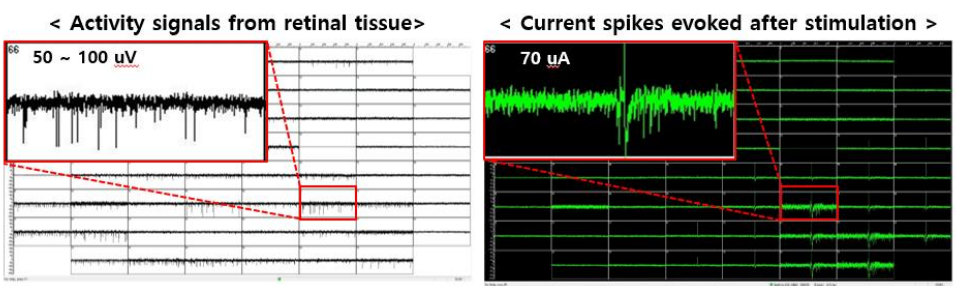

Figure 125 The spontaneous activity signal from retinal tissue and current spikes evoked after applying bipolar stimulation current

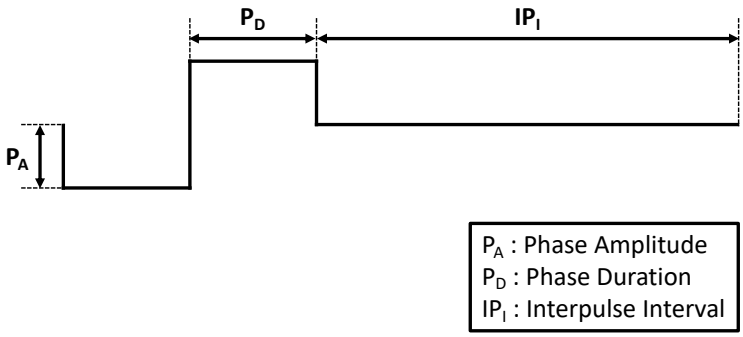

Figure 126 Stimulation parameters: cathodic-first biphasic pulse, PA: 3000mV, PD: 500 μs, IPI: 999 ms, frequency 1 Hz, 20 trains

After applying cathodic-first, biphasic, symmetrically square-shaped current pulses in 70uA amplitude, electrically evoked ganglion cell activities were observed (Figure 127). This complex waves are composed of responses of multiple ganglion cells adjacent to the stimulation electrode and the consecutive harmonic waves of the stimulation signal. The strongest response can be postulated as the evoked potential of the nearest ganglion cell of the electrode, and it is between 60 to 75uV in amplitude. Responses smaller than 60 uV may be the responses of the adjacent ganglion cells, and the consecutive harmonic waves of the stimulation signal rapidly decays more than half on each repetition, thus the threshold voltage was set as -65uV to simplifying the sorting of the spikes.

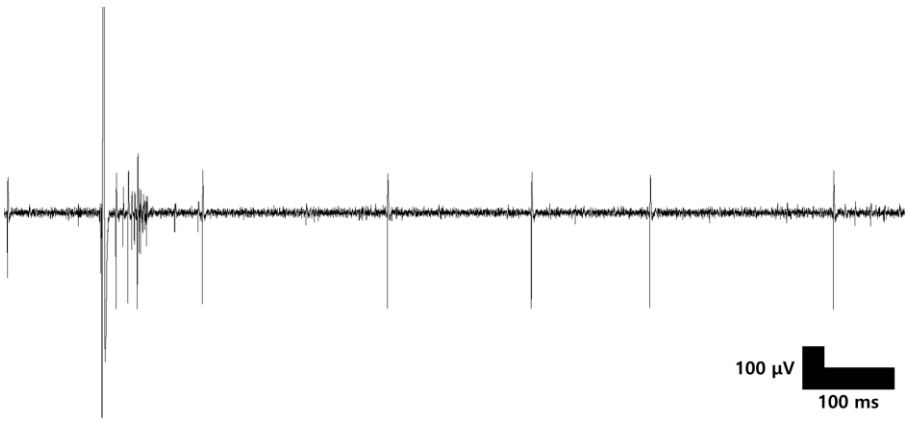

Figure 127 Evoked RGC activity by voltage stimulation

By this way, single cell evoked potential on the electrical stimulation was sorted (Figure 128) from the recording during 20 trains of electrical stimuli, and the post-stimulus time histogram (PSTH) was made with the number of spikes sorted for 1s after stimulation, in time interval of 5ms (Figure 129).

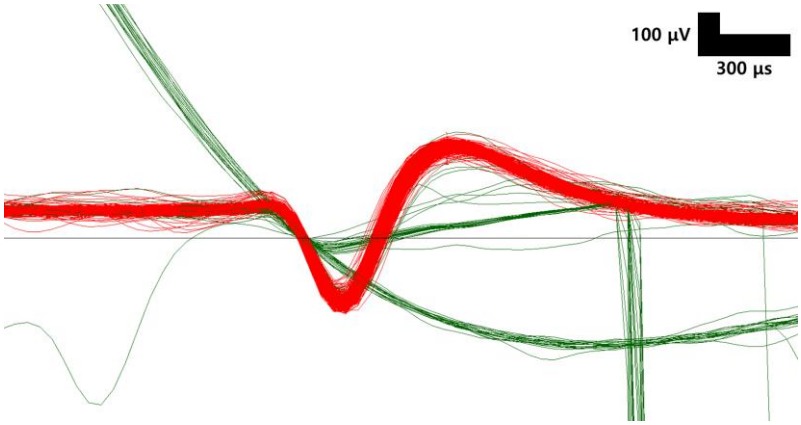

Figure 128 Voltage spike sorting with threshold voltage of −65uV

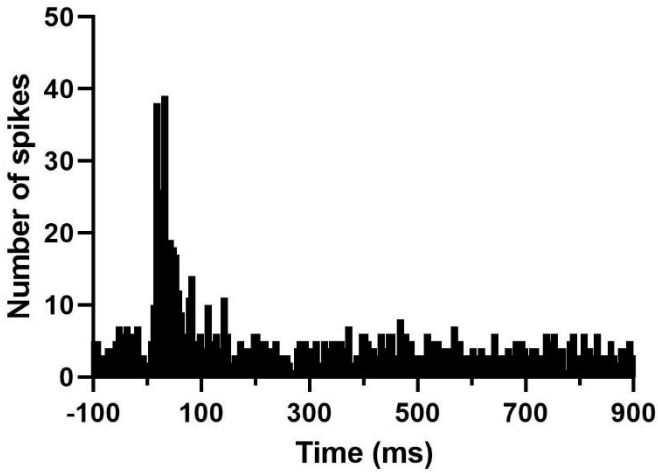

Figure 129 Post-stimulus time histogram (PSTH) of electrically evoked retinal ganglion cell (RGC) responses (time bin: 5 ms)

Chapter 4. Discussion

4.1 Electric characteristics improve with electroplating

The starting measurement value of the leakage current of PFA based electrode from section 3.2.3 (Figure 120) is higher than other polymer-based electrode samples. This is due to the measurement after calibrating the pico-ammeter used in the experiment. Before the machine calibration, the default base value was around 10^{-12}A, while the value after the calibration was set as 10^{-9}A. Therefore, the leakage current value of the PFA film-based electrode is still maintaining a 10^{-}

^{9}A level.

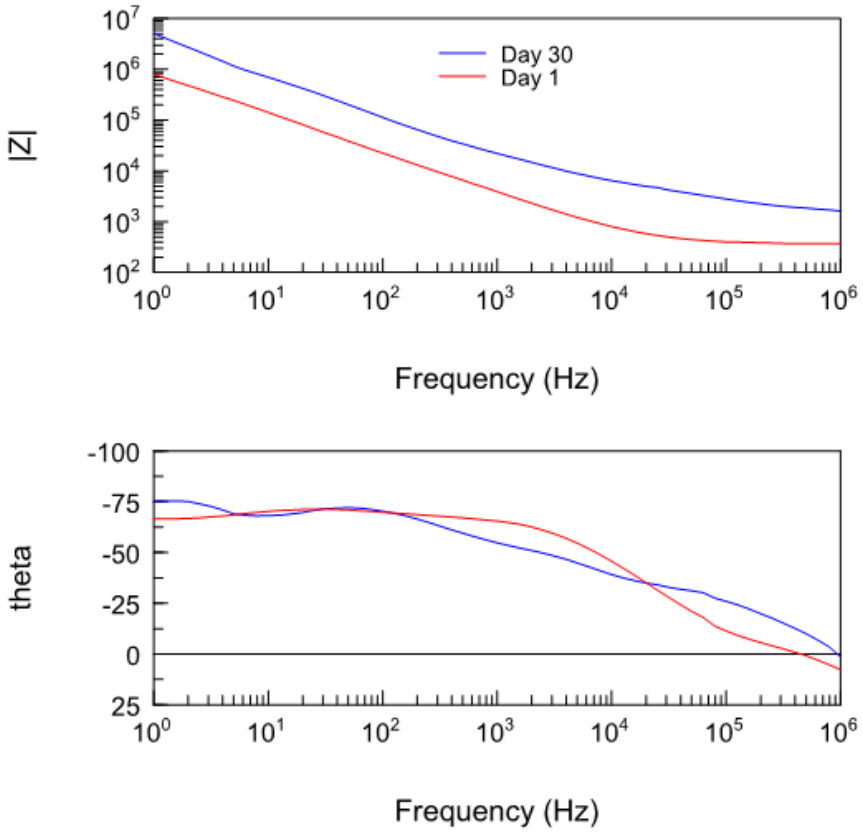

Figure 130 Impedance after 30 days of soak test

After the 30 days of accelerated soak test in 75℃ PBS, the impedance of PFA based electrodes were checked to see the performance, which was measured around 22kohm. Applying the 10-degree rule, 30 days in 75℃ can be roughly approximated to 480 days in human body temperature. Even with conservative prediction, it can

be expected that the PFA packaging can last at least one year in in vivo environment.

The impedance improvement will be presented by electro-plating porous gold or iridium oxide on the stimulation opening sites. Also, in the future, the productiveness of stimulating neurons should be exploited through in vivo tests. However, making MEA based on PFA film is still in the early stages of the investigation. So a longer assessment of its reliability will be required to guarantee at least 10 years of a lifetime after the initial implant without getting damaged.

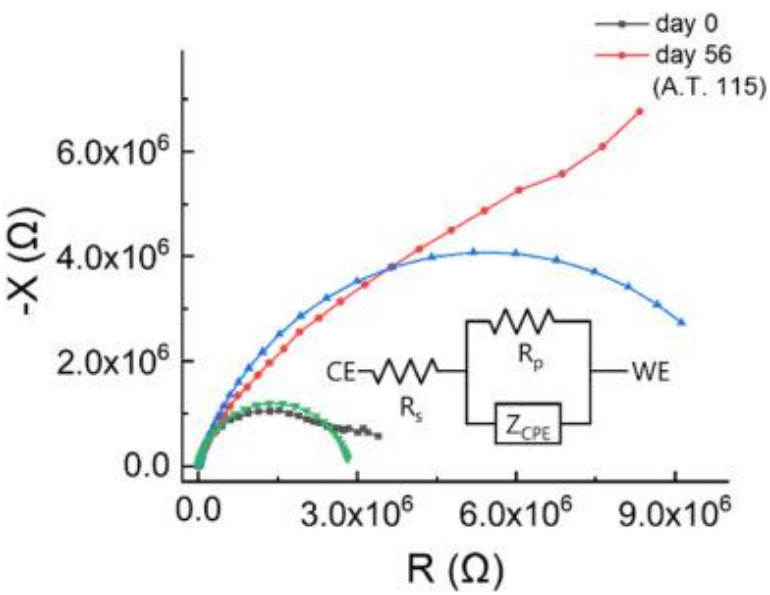

Figure 131 Impedance change during soak test [111]

The impedance of the encapsulation at 1 kHz is important for a

lot of applications, e.g., neural recording and stimulation, because the frequency of action potentials is about 1 kHz.

The reason of increase of the impedance of the electrode during the 30 days accelerated soak test can be seen from Figure 131. The electrode can be represented as circuit model as in figure. R_S represents the solution resistance, constant phase element Z_{CNE} is a modeling of electrochemical double layer existing at the electrode-electrolyte interface. Lastly R_P is polarization resistance. Comparing the day 0 circuit element to the day56, R_S and Z_{CPE} remained relatively unaffected while the R_P value showed a significant rise. R_S can be affected by ionic concentration. However, the electrode mainly consists of polymer film substrate and gold. Neither of them was expected to remarkably get ionized to change the concentration of electrolyte during CV measurement. Correspondingly, R_S exhibited less considerable change. Z_{CPE} is formed by a potential attracting mobile charge in a solution and is usually close to pseudo-capacitance. Impure capacitance seems to be degraded during the test, nonetheless, not as much as R_P. That is, R_S and Z_{CPE} are relatively close to chemical properties that are not expected to be affected by heat during the soak

test; however, R_P describes interfacial charge transfer kinetics and affected by changes in the electrical characteristics of the channel. As demonstrated by the figure, impedance increased as the acceleration soak test progressed. Thus, R_P also increased with the degradation of charge storage capacity, corresponding to the impedance change trend.

From the measurement of the 30days soak test, the impedance value can be increased due to moisture penetration due to the bigger opening site compared to the electrode stimulation site. Suppose the metal pattern of the electrode stimulation site peeled off during the accelerated soak test. In that case, the geometrical area goes higher than in ordinary conditions, and the impedance value might go down. However, according to Tencer' s model, the electrical stimulation surface can be represented as electric components. [112] By applying stimulation through the electrode, the charge storage capacity tends to degrade as the stimulation goes further. This might increase the RP during the soak test. Also, there will be pathways of water leakage along the soaked electrode surface. Various leakage pathways might affect the interface of PFA-PFA sealing and PFA-metal adhesion. This behavior needs further development by fitting impedance from CV

measurement and checking the R_P trend by checking the value daily.

4.2 Wireless operation of the full system

To get an information of bit error rate (BER) and signal to interference ratio (SIR) during the wireless operation of the full system. Fabrication and designing of the proper coil for wireless operation should be continued in the future. The drop in zero-crossing shifts has significantly increased the BER for $\Delta td>2$ ns. The use of crystal-based oscillators with sub-nanosecond jitter is feasible in the external power Tx due to its relatively relaxed size constraints. In systems with high jitter oscillators, PDL should be reduced to increase the amount of zero-crossing shifts or SIR to keep the BER low. Furthermore, in a complete system, the data Tx block can actively adjust in a closed loop to maintain its optimal value for the lowest BER.

The SIR should also be considered according to the alignment and coupling of the coil pairs. An additional study must be conducted to investigate the wireless system performance. The current experiment measurement achieved the standard BER of 10^{-6} with manually designed litz wire coils. The small planar spiral coil needs to be used

for better measurements and application for retinal prosthesis.

4.3 Further improvements and potential applications

In this study, two subsystems for artificial retinas were developed. The wireless power and data transfer system and PFA-film-based MEAs. Since the wireless power and data transfer system was designed for 16 channels 64 electrodes neural stimulator, the fabricated thin film PFA MEAs must be developed in higher density.

To achieve higher electrode density, the size of the electrode stimulation site needs to be reduced. The circuitry and electrode will be packaged in a monolithic structure using thermal lamination and flip-chip bonding. Filp-chip bonding is made to make a protrusion such as a solder ball on the electrode pattern of flip chip bonding or the inner lead and make it electrically connected when placing the chip on the board. This method allows flip-chip bonding to save as much space as wire bonding, making it possible to manufacture small packages.

Since the thermal lamination process of PFA-film proceeds at a high temperature of around 300℃, the maintenance of the circuitry performance will be critical. For this monolithic encapsulation, different

methods should be done, such as using a spin-coatable PFA solution.

The PFA film-based electrode can be produced at a low cost. The current application for this circuitry and MEAs is artificial retinas; however, since the specifications are designed for the general application of low-powered medical devices, both subsystems can be applied in various fields. The power and data transceiver circuitry achieved over 30mW, which can be applied to those IMDs using the near-field transmission. With around 10Mbps of data rate, this system can also be applied to deep brain stimulation, cochlear implants, biosensors, etc. In addition, to the advantage of PFA-based electrodes due to their low water absorption rate and long-term reliability, the MEAs also be used for various neural prosthetic applications. While Young' s modulus is not high enough for shank electrodes, the application can be limited for planar electrodes.

Several issues still need improvements, such as decreasing the size of the opening site. Currently, an RIE etcher is used for opening, and this is done by etching the cover film first and laminating it with substrate film afterward. This process should be done after the thermal lamination of the substrate and cover films together for batch

production.

Chapter 5. Conclusion

Therefore, this study presents an inductive wireless power transmission system designed to meet the requirements of an artificial retina and an electrode based on a biocompatible polymer. A reconfigurable DC-DC step-up converter capable of boosting with various multipliers was designed considering the low coupling factor of wireless power transmission in an implantable device in vivo, and a target power of 30mW was achieved with an output voltage of 5V. We have presented a switched-capacitor, step-up converter based on Dickson topology designed to meet the requirements of implantable medical devices supplied by inductive wireless power transfer systems. We derived the peculiar specifications that the applications falling in the above category impose on the converter, with particular reference to the input voltage variability induced by the uncertainty in the magnetic coupling factor of the WPT.

We developed a simple model to estimate a priori the input voltage range, and proposed to resort to a reconfigurable converter that

adapts the conversion ratio to the input voltage value, in order to minimize conduction power losses. We discussed in detail a procedure for the optimal sizing of the converter switches from the point of view of efficiency. The procedure is based on an analytical model of the switches conduction and driving losses and allows to derive the absolute switch size that maximizes the reconfigurable SCC overall efficiency. A thorough set of transistor-level simulation results is included to demonstrate the performance and robustness of the converter.

A PFA film-based implantable neural electrodes fabrication method. PFA has several merits, such as low water absorption rate and relatively low Young' s modulus compared to other biocompatible polymers. Performance and reliability tests were performed to evaluate these electrodes' characteristics. The impedance-charge storage capacitance analysis showed that the electrical performance of the PFA electrode is better than those of other biocompatible polymer-based electrodes. The bending test confirmed that the fabricated PFA planar electrode has flexible and durable physical performance. The accelerated soak test proposed that the PFA electrode can be implanted

without any external distortions over 8 years. In vitro test results showed biocompatibility of selected PFA material that it doesn’t cause any hazardous effect in vivo environment. From ex vivo test, it could be able to catch the stimulation performance of the fabricated MEA.

Reference

[1] Volkmann, Jens. "Deep brain stimulation for the treatment of Parkinson's disease." Journal of clinical neurophysiology 21.1 (2004): 6-17.

[2] Humayun, Mark S., et al., eds. Artificial sight: basic research, biomedical engineering, and clinical advances. Springer Science & Business Media, 2007.

[3] Weiland, James D., Wentai Liu, and Mark S. Humayun. "Retinal prosthesis." Annu. Rev. Biomed. Eng. 7 (2005): 361-401.

[4] Margalit, Eyal, et al. "Retinal prosthesis for the blind." Survey of ophthalmology 47.4 (2002): 335-356.

[5] Zeng, Fan-Gang, et al. "Cochlear implants: system design, integration, and evaluation." IEEE reviews in biomedical engineering 1 (2008): 115-142.

[6] Zeng, Fan-Gang. "Trends in cochlear implants." Trends in amplification 8.1 (2004): 1-34.

[7] Loizou, Philipos C. "Introduction to cochlear implants." IEEE Engineering in Medicine and Biology Magazine 18.1 (1999): 32-42.

[8] DiFrancesco, Dario. "Pacemaker mechanisms in cardiac tissue." Annual review of physiology 55.1 (1993): 455-472.

[9] Benabid, Alim Louis. "Deep brain stimulation for Parkinson's disease." Current opinion in neurobiology 13.6 (2003): 696-706.

[10] Clark, Graeme. "Cochlear implants." Speech processing in the auditory system. Springer, New York, NY, 2004. 422-462.

[11] Ben Amar, Achraf, Ammar B. Kouki, and Hung Cao. "Power approaches for implantable medical devices." sensors 15.11 (2015): 28889-28914.

[12] Yang, Jiachen, et al. "A low-power and portable biomedical device for respiratory monitoring with a stable power source." Sensors 15.8 (2015): 19618-19632.

[13] Nathan, Menachem. "Microbattery technologies for miniaturized implantable medical devices." Current pharmaceutical biotechnology 11.4 (2010): 404-410.

[14] Bock, David C., et al. "Batteries used to power implantable biomedical devices." Electrochimica acta 84 (2012): 155-164.

[15] Drews, J., et al. "Primary batteries for implantable pacemakers and defibrillators." Journal of power sources 97 (2001): 747-749.

[16] Das, Rupam, et al. "Serpentine-Shaped Metamaterial Energy Harvester for Wearable and Implantable Medical Systems." 2021 IEEE International Symposium on Circuits and Systems (ISCAS). IEEE, 2021.

[17] Bazaka, Kateryna, and Mohan V. Jacob. "Implantable devices: issues and challenges." Electronics 2.1 (2012): 1-34.

[18] Kim, Han-Joon, et al. "Review of near-field wireless power and communication for biomedical applications." IEEE Access 5 (2017): 21264-21285.

[19] Das, Rupam, Farshad Moradi, and Hadi Heidari. "Biointegrated and wirelessly powered implantable brain devices: A review." IEEE transactions on biomedical circuits and systems 14.2 (2020): 343-358.

[20] Schormans, Matthew, Virgilio Valente, and Andreas Demosthenous. "Practical inductive link design for biomedical wireless power transfer: A tutorial." IEEE Transactions on Biomedical Circuits and Systems 12.5 (2018): 1112-1130.

[21] Yue, Lan, et al. "Retinal stimulation strategies to restore vision: Fundamentals and systems." Progress in retinal and eye research 53 (2016): 21-47.

[22] Hartong, Dyonne T., Eliot L. Berson, and Thaddeus P. Dryja. "Retinitis pigmentosa." The Lancet 368.9549 (2006): 1795-1809.

[23] Lim, Laurence S., et al. "Age-related macular degeneration." The Lancet 379.9827 (2012): 1728-1738.

[24] Richer, Stuart, et al. "Double-masked, placebo-controlled, randomized trial of lutein and antioxidant supplementation in the intervention of atrophic age-related macular degeneration: the Veterans LAST study (Lutein Antioxidant Supplementation Trial)." Optometry-Journal of the American Optometric Association 75.4 (2004): 216-229.

[25] Fariss, Robert N., Zong-Yi Li, and Ann H. Milam. "Abnormalities in rod photoreceptors, amacrine cells, and horizontal cells in human retinas with retinitis pigmentosa." American journal of ophthalmology 129.2 (2000): 215-223.

[26] Kim, S. Y., et al. "Morphometric analysis of the macula in eyes with disciform age-related macular degeneration." Retina 22.4 (2002): 471-477.

[27] Weiland, James D., Alice K. Cho, and Mark S. Humayun. "Retinal prostheses: current clinical results and future needs." Ophthalmology

118.11 (2011): 2227-2237.

[28] Tehovnik, Edward J. "Electrical stimulation of neural tissue to evoke behavioral responses." Journal of neuroscience methods 65.1 (1996): 1-17.

[29] Bishop, George H. "Natural history of the nerve impulse." Physiological Reviews 36.3 (1956): 376-399.

[30] Rattay, Frank. "The basic mechanism for the electrical stimulation of the nervous system." Neuroscience 89.2 (1999): 335-346.

[31] Yue, Lan, et al. "Retinal stimulation strategies to restore vision: Fundamentals and systems." Progress in retinal and eye research 53 (2016): 21-47.

[32] Mathieson, Keith, et al. "Photovoltaic retinal prosthesis with high pixel density." Nature photonics 6.6 (2012): 391-397.

[33] Soltan, Ahmed, et al. "A head mounted device stimulator for optogenetic retinal prosthesis." Journal of neural engineering 15.6 (2018): 065002.

[34] Hu, Monica L., et al. "Gene therapy for inherited retinal diseases: progress and possibilities." Clinical and Experimental Optometry 104.4 (2021): 444-454.

[35] M. S. Humayun, J. D. Dorn, L. da Cruz, G. Dagnelie, J.-A. Sahel, P. E. Stanga, et al., "Interim Results from the International Trial of Second Sight's Visual Prosthesis," Ophthalmology, vol. 119, pp. 779-788, Apr 2012.

[36] J. D. Weiland, A. K. Cho, and M. S. Humayun, "Retinal prostheses: current clinical results and future needs," Ophthalmology, vol. 118, pp. 2227-2237, 2011.

[37] S. K. Kelly, D. B. Shire, J. Chen, P. Doyle, M. D. Gingerich, S. F. Cogan, et al., "A hermetic wireless subretinal neurostimulator for vision prostheses," IEEE Trans Biomed Eng, vol. 58, pp. 3197-205, Nov 2011.

[38] K. Mathieson, J. Loudin, G. Goetz, P. Huie, L. Wang, T. I. Kamins, et al., "Photovoltaic retinal prosthesis with high pixel density," Nat Photon, vol. 6, pp. 391-397, May 2012.

[39] K. Stingl, K. U. Bartz-Schmidt, D. Besch, A. Braun, A. Bruckmann, F. Gekeler, et al., "Artificial vision with wirelessly powered subretinal electronic implant alpha-IMS," Proceedings of the Royal Society B: Biological Sciences, vol. 280, Apr 2013.

[40] J. A. Zhou, S. J. Woo, S. I. Park, E. T. Kim, J. M. Seo, H. Chung,

et al., "A suprachoroidal electrical retinal stimulator design for long-term animal experiments and in vivo assessment of its feasibility and biocompatibility in rabbits," Journal of Biomedicine and Biotechnology, vol. 2008, 2008.

[41] T. Fujikado, M. Kamei, H. Sakaguchi, H. Kanda, T. Morimoto, Y. Ikuno, et al., "Testing of semichronically implanted retinal prosthesis by suprachoroidaltransretinal stimulation in patients with retinitis pigmentosa," Investigative Ophthalmology & Visual Science, vol. 52, pp. 4726-4733, 2011.

[42] Fernández, Delia Cabrera, Harry M. Salinas, and Carmen A. Puliafito. "Automated detection of retinal layer structures on optical coherence tomography images." Optics express 13.25 (2005): 10200-10216.

[43] Ho, Allen C., et al. "Long-term results from an epiretinal prosthesis to restore sight to the blind." Ophthalmology 122.8 (2015): 1547-1554.

[44] Stingl, Katarina, et al. "Subretinal visual implant alpha IMS–clinical trial interim report." Vision research 111 (2015): 149-160.

[45] Mathieson, Keith, et al. "Photovoltaic retinal prosthesis with high

pixel density." Nature photonics 6.6 (2012): 391-397.

[46] Rizzo, Joseph, and John Wyatt. "ARTIFICIAL RETINA." Technology Review 107.7 (2004): 82-85.

[47] Yue, Lan, et al. "Retinal stimulation strategies to restore vision: Fundamentals and systems." Progress in retinal and eye research 53 (2016): 21-47.

[48] Lawrence, Stephen M., Gurpreet S. Dhillon, and Kenneth W. Horch. "Fabrication and characteristics of an implantable, polymer-based, intrafascicular electrode." Journal of neuroscience methods 131.1-2 (2003): 9-26.

[49] Sastri, Vinny R. "Regulations for Medical Devices and Application to Plastics Suppliers: history and Overview." Handbook of Polymer Applications in Medicine and Medical Devices. William Andrew Publishing, 2010. 337-346.

[50] Baek, Ju Yeoul, et al. "Stable deposition and patterning of metal layers on the PDMS substrate and characterization for the development of the flexible and implantable micro electrode." Solid State Phenomena. Vol. 124. Trans Tech Publications Ltd, 2007.

[51] Lago, Natalia, et al. "Assessment of biocompatibility of chronically

implanted polyimide and platinum intrafascicular electrodes." IEEE Transactions on Biomedical Engineering 54.2 (2007): 281-290.

[52] Winslow, Brent D., et al. "A comparison of the tissue response to chronically implanted Parylene-C-coated and uncoated planar silicon microelectrode arrays in rat cortex." Biomaterials 31.35 (2010): 9163-9172.

[53] Lawrence, Stephen M., et al. "Long-term biocompatibility of implanted polymer-based intrafascicular electrodes." Journal of Biomedical Materials Research: An Official Journal of The Society for Biomaterials, The Japanese Society for Biomaterials, and The Australian Society for Biomaterials and the Korean Society for Biomaterials 63.5 (2002): 501-506.

[54] Sastri, Vinny R. "Engineering thermoplastics: acrylics, polycarbonates, polyurethanes, polyacetals, polyesters, and polyamides." Plastics in medical devices (2010): 121-173.

[55] Sastri, Vinny R. "High-temperature engineering thermoplastics: polysulfones, polyimides, polysulfides, polyketones, liquid crystalline polymers, and fluoropolymers." Plast Med Devices, 2nd ed.; Sastri, VR, Ed.; William Andrew Publishing: Oxford, UK (2014): 173-213.

[56] Garnica, Jaime, Raul A. Chinga, and Jenshan Lin. "Wireless power transmission: From far field to near field." Proceedings of the IEEE 101.6 (2013): 1321-1331.

[57] Jawad, Aqeel Mahmood, et al. "Opportunities and challenges for near-field wireless power transfer: A review." Energies 10.7 (2017): 1022.

[58] Garnica, Jaime, Raul A. Chinga, and Jenshan Lin. "Wireless power transmission: From far field to near field." Proceedings of the IEEE 101.6 (2013): 1321-1331.

[59] Mercier, Patrick P., and Anantha P. Chandrakasan. "Near-field wireless power transfer." Ultra-Low-Power Short-Range Radios. Springer, Cham, 2015. 343-375.

[60] Chang, Joseph S., et al. "Analysis and design of power efficient class D amplifier output stages." IEEE Transactions on Circuits and Systems I: Fundamental Theory and Applications 47.6 (2000): 897-902.

[61] Athas, William C., L. J. Svensson, and N. Tzartzanis. "A resonant signal driver for two-phase, almost-non-overlapping clocks." 1996 IEEE International Symposium on Circuits and Systems. Circuits and

Systems Connecting the World. ISCAS 96. Vol. 4. IEEE, 1996.

[62] Chang, Joseph S., et al. "Analysis and design of power efficient class D amplifier output stages." IEEE Transactions on Circuits and Systems I: Fundamental Theory and Applications 47.6 (2000): 897-902.

[63] Yang, Shiyan, Jingfang Wang, and Wei Yang. "A novel 24-pulse diode rectifier with an auxiliary single-phase full-wave rectifier at DC side." IEEE Transactions on Power Electronics 32.3 (2016): 1885-1893.

[64] Peters, Christian, et al. "CMOS integrated highly efficient full wave rectifier." 2007 IEEE International Symposium on Circuits and Systems. IEEE, 2007.

[65] Kumngern, M., and K. Dejhan. "High frequency and high precision CMOS full-wave rectifier." International Journal of Electronics 93.03 (2006): 185-199.

[66] Milliken, Robert J., Jose Silva-Martínez, and Edgar Sánchez-Sinencio. "Full on-chip CMOS low-dropout voltage regulator." IEEE Transactions on Circuits and Systems I: Regular Papers 54.9 (2007): 1879-1890.

[67] Roh, Jeongjin. "High-performance error amplifier for fast transient DC-DC converters." IEEE Transactions on Circuits and Systems II: Express Briefs 52.9 (2005): 591-595.

[68] Banba, Hironori, et al. "A CMOS bandgap reference circuit with sub-1-V operation." IEEE Journal of Solid-State Circuits 34.5 (1999): 670-674.

[69] Shen, Yongjian, and Ran Zhang. "Constant-gm bias circuit without off-chip components." 2016 13th IEEE International Conference on Solid-State and Integrated Circuit Technology (ICSICT). IEEE, 2016.

[70] Oguey, Henri J., and Daniel Aebischer. "CMOS current reference without resistance." IEEE Journal of Solid-State Circuits 32.7 (1997): 1132-1135.

[71] Chun, Tae-Won, et al. "Sensorless control of BLDC motor drive for an automotive fuel pump using a hysteresis comparator." IEEE transactions on power electronics 29.3 (2013): 1382-1391.

[72] GUO, Dan, Fu-lei CHU, and D. Chen. "The unbalanced magnetic pull and its effects on vibration in a three-phase generator with eccentric rotor." Journal of sound and Vibration 254.2 (2002): 297-312.

[73] Lo, Y., Chen, K., Gad, P., & Liu, W. (2013). A fully-integrated high-compliance voltage SoC for epi-retinal and neural prostheses. IEEE Transactions on Biomedical Circuits and Systems, 7(6), 761–772.

[74] Das, R., Moradi, F., & Heidari, H. (2020). Biointegrated and wirelessly powered implantable brain devices: A review. IEEE Transactions on Biomedical Circuits and Systems, 14(2), 343–358.

[75] Yoo, H. J., & van Hoof, C. (Eds.). (2010). Bio-medical CMOS ICs. UK: Springer Science & Business Media.

[76] Bocan, Kara N., and Ervin Sejdić. "Adaptive transcutaneous power transfer to implantable devices: A state of the art review." Sensors 16.3 (2016): 393.

[77] Trigui, A., Hached, S., Ammari, A. C., Savaria, Y., & Sawan, M. (2019). Maximizing data transmission rate for implantable devices over a single inductive link: Methodological review. IEEE Reviews in Biomedical Engineering, 12, 72–87.

[78] Bikson, Marom, Abhishek Datta, and Maged Elwassif. "Establishing safety limits for transcranial direct current stimulation." Clinical neurophysiology: official journal of the International Federation of Clinical Neurophysiology 120.6 (2009): 1033.

[79] Kiani, M., & Ghovanloo, M. (2015). A 13.56-Mbps pulse delay modulation based transceiver for simultaneous near-field data and power transmission. IEEE Transactions on Biomedical Circuits and Systems, 9(1), 1–11.

[80] Seeman, M. D. (2009). A design methodology for switched-capacitor DC-DC converters. University of California, Berkeley.

[81] Ben-Yaakov, S., & Kushnerov, A. (2009). Algebraic foundation of self adjusting switched capacitors converters. In 2009 IEEE Energy Conversion Congress and Exposition, San Jose, CA (pp. 1582–1589).

[82] Kushnerov, A., & Ben-Yaakov, S. (2012). The best of both worlds: Fibonacci and binary switched capacitor converters combined. In 6th IET International Conference on Power Electronics, Machines and Drives (PEMD 2012), pp. 1–5.

[83] Seeman, M. D., & Sanders, S. R. (2008). Analysis and optimization of switched capacitor DC-DC converters. IEEE Transactions on Power Electronics, 23(2), 841–851.

[84] Zhang, Huijie, et al. "A wide-input-range low-power ASK demodulator for wireless data transmission in retinal prosthesis." 2016 IEEE Biomedical Circuits and Systems Conference (BioCAS). IEEE,

2016.

[85] Yang, Jiawei, and Efstratios Skafidas. "A low power MICS band phase-locked loop for high resolution retinal prosthesis." IEEE transactions on biomedical circuits and systems 7.4 (2012): 513-525.

[86] Kiani, Mehdi, and Maysam Ghovanloo. "Pulse delay modulation (PDM) a new wideband data transmission method to implantable medical devices in presence of a power link." 2012 IEEE Biomedical Circuits and Systems Conference (BioCAS). IEEE, 2012.

[87] Jovanović, Goran S., and Mile K. Stojčev. "Current starved delay element with symmetric load." International journal of electronics 93.03 (2006): 167-175.

[88] Rahim, Nasrudin Abd, Mohamad Fathi Mohamad Elias, and Wooi Ping Hew. "Transistor-clamped H-bridge based cascaded multilevel inverter with new method of capacitor voltage balancing." IEEE Transactions on Industrial Electronics 60.8 (2012): 2943-2956.

[89] Wu, Jiande, et al. "Wireless power and data transfer via a common inductive link using frequency division multiplexing." IEEE transactions on industrial electronics 62.12 (2015): 7810-7820.

[90] Wang, Guoxing, et al. "Analysis of dual band power and data

telemetry for biomedical implants." IEEE Transactions on biomedical circuits and systems 6.3 (2011): 208-215.

[91] Kiani, Mehdi, and Maysam Ghovanloo. "A 13.56-Mbps pulse delay modulation based transceiver for simultaneous near-field data and power transmission." IEEE transactions on biomedical circuits and systems 9.1 (2014): 1-11.

[92] Ko, Uming, and Poras T. Balsara. "High-performance energy-efficient D-flip-flop circuits." IEEE Transactions on Very Large Scale Integration (VLSI) Systems 8.1 (2000): 94-98.

[93] Yue, Lan, et al. "Retinal stimulation strategies to restore vision: Fundamentals and systems." Progress in retinal and eye research 53 (2016): 21-47.

[94] Kim, Yong Hee, et al. "Fluoropolymer-based flexible neural prosthetic electrodes for reliable neural interfacing." ACS applied materials & interfaces 9.50 (2017): 43420-43428.

[95] Kim, Yong Hee, and Sang-Don Jung. "Simultaneous photoadhesion and photopatterning technique for passivation of flexible neural electrodes based on fluoropolymers." Scientific reports 10.1 (2020): 1-13.

[96] Yasuda, T., T. Okuno, and H. Yasuda. "Contact angle of water on polymer surfaces." Langmuir 10.7 (1994): 2435-2439.

[97] Mittal, K. L. Adhesion measurement: Recent progress, unsolved problems, and prospects. ASTM International, 1978.

[98] Shin, Soowon, et al. "High charge storage capacity electrodeposited iridium oxide film on liquid crystal polymer-based neural electrodes." Sens. Mater 28.3 (2016): 243-260.

[99] Schuettler, Martin, et al. "Stretchable tracks for laser-machined neural electrode arrays." 2009 Annual International Conference of the IEEE Engineering in Medicine and Biology Society. IEEE, 2009.

[100] R. Das, F. Moradi and H. Heidari, "Biointegrated and Wirelessly Powered Implantable Brain Devices: A Review," IEEE Trans. Biomed. Circuits Syst., vol. 14, no. 2, pp. 343-358, Apr. 2020.

[101] Hoi-Jun Yoo and Chris van Hoof, eds. Bio-Medical CMOS ICs, Springer Science & Business Media, 2010.

[102] Weiland, James D., Wentai Liu, and Mark S. Humayun. "Retinal prosthesis."Annu. Rev. Biomed. Eng.7 (2005): 361-401.

[103] Cosman Jr, Eric R., and Eric R. Cosman Sr. "Electric and thermal field effects in tissue around radiofrequency electrodes." Pain Medicine

6.6 (2005): 405-424. [104] Jeong, Joonsoo, et al. "A miniaturized, eye-conformable, and long-term reliable retinal prosthesis using monolithic fabrication of liquid crystal polymer (LCP)." IEEE transactions on biomedical engineering 62.3 (2014): 982-989.

[105] Baek, C. H., et al.,“Fabrication and evaluation of cyclic olefin copolymer based implantable neural electrode.” IEEE Transactions on Biomedical Engineering 67.9, pp. 2542–2551, 2020.

[106] Suhir, E., et al.,“Accelerated life testing (ALT) in microelectronics and photonics: its role, attributes, challenges, pitfalls, and interaction with qualification tests.” J. Electron. Packag. 124.3, pp. 281–291, 2002.

[107] S. W. Lee, K. S. Min, J. Jeong, J. Kim and S. J. Kim, "Monolithic Encapsulation of Implantable Neuroprosthetic Devices Using Liquid Crystal Polymers," in IEEE Transactions on Biomedical Engineering, vol. 58, no. 8, pp. 2255-2263, Aug. 2011

[108] Yoo, Eun-Sun, et al. "Adherent cells generated during long-term culture of human umbilical cord blood CD34+ cells have characteristics of endothelial cells and beneficial effect on cord blood ex vivo expansion." Stem Cells 21.2 (2003): 228-235.

[109] Rezzola, Sara, et al. "In vitro and ex vivo retina angiogenesis assays." Angiogenesis 17.3 (2014): 429-442.

[110] Rountree, Corey M., et al. "Prototype chemical synapse chip for spatially patterned neurotransmitter stimulation of the retina ex vivo." Microsystems & Nanoengineering 3.1 (2017): 1-12.

[111] Kim, Ju-Hwan, et al. "Investigation on Parylene-C based neural electrodes by accelerated life test and reliability improvement using polyimide flexible cable." Current Applied Physics 39 (2022): 214-220.

[112] Tencer, Michal. "Moisture ingress into nonhermetic enclosures and packages. A quasi-steady state model for diffusion and attenuation of ambient humidity variations." 1994 Proceedings. 44th Electronic Components and Technology Conference. IEEE, 1994.

국문 초록

신경 보철 장치는 신경 기능 장애가 있는 환자에게 직접적인 전기 자극을 통해 기능 회복을 돕는 이식형 의료기기이며 현재 뇌심부자극술, 인공망막, 인공와우, 심장박동기 등 다양한 분야에서 환자들을 돕고 있다. 최근 들어 인공 망막 기법은 시각 시스템에서 손상되지 않은 양극성 세포 또는 망막 신경절 세포를 전기적으로 자극하여 망막의 기능을 상실한 맹인들의 시력을 회복하는 방식으로 부각이 되고 있다. 인공 망막과 같은 이식형 생체 의료 기기에서 주로 발생하는 문제점은 생체 내부에 삽입할 수 있는 공간이 제한적이라는 것이다. 기존에 사용되고 있는 이식형 배터리는 부피가 크며 주기적으로 교체를 해주어야 한다는 한계점이 있다. 따라서 이식형 의료 기기에는 상대적으로 작은 크기로 안정적인 공급 전압을 제공하기 위해 무선 전력 전송 시스템이 필요하다. 기존의 이식형 의료 기기에서 사용되는 전력 및 정보 송수신 기술뿐만 아니라 생체 적합 재료에 대한 한계도 존재한다. 이식 가능한 신경 보철 장치에 사용되는 재료들에는 일반적으로 생체 적합성 금속, 유리 또는 세라믹이 있다. 티타늄과 같은 금속 기반 인캡슐레이션의 경우 시스템 분리로 인해 피드스루 기술이 필요하다. 또한, 조립 과정이 복잡하고 완성된 모듈이 부피가 커서 체내 이식 부위에 한계가 있거나 내부 조직에 손상을 줄 수

있다. 미세전자기계시스템 (MEMS) 호환 폴리머 기반 장치도 현재로서는 장기 이식을 위한 내구성이 충분하지 않다.

따라서 이 연구에서는 인공 망막의 요구 사항을 충족하도록 설계된 유도 무선 전력 전송 시스템과 생체 적합 불소 수지 PFA 기반의 평면형 전극을 제시하였다. 생체 내 이식 장치의 무선 전력 전송의 낮은 결합 계수를 고려하여 다양한 배율로 승압이 가능한 재구성 가능한 DC-DC 승압 컨버터를 설계하였으며 5V 출력 전압으로 30mW의 목표 전력을 달성했다. 무선 정보 전송을 위해서는 펄스 지연 변조 기법을 사용하여 전력 전송 주파수인 13.56MHz와 동일한 13.56Mbps의 정보 전송률을 달성하였다. 또한 수분 흡수율이 낮고 열 접합이 가능한 20-채널 전극을 디자인하여 총 두께가 62.7um인 얇고 유연한 일체형 공정 기술을 확립하였다. 일반적인 인공망막의 임계 전하 밀도 한계인 0.65mC/cm^2 이상의 충전 저장 용량을 달성하였다.

개발된 인공 시각 장치의 장기 내구성을 위하여 성능, 안정성, 생체 적합성을 in vitro 및 ex vivo 실험을 통해 검증하였다. 가속 수명 시험을 통하여 미루어 보았을 때, 자극 전극의 폴리머-금속 접합은 75℃에서 180일 이상 버티고 있으며 현재 진행 중이다. 해당 기간은 생체 내 온도에서 약 8년 이상 정상 작동을 할 것으로 예상된다. 생체 적합성은 ISO 기준 및 대한 약전 기준 세포독성시험과 용출물 시험을 통해

검증하였으며 생체 적합 판정을 받았다. 또한 ex vivo 실험을 통한 전극의 자극의 유효성을 검증하였다.

주요어: 신경보철, 망막보철, PFA(Perfluoro alkoxyalkane), 미세전극배열, DC-DC 승압변환기, 펄스변환변조 (PDM)

학번 : 2017-22199